Title
HYDROGEL-BASED BIOADHESIVES FOR TISSUE ENGINEERING AND SURGICAL APPLICATIONS

Author
Shirzaei Sani, Ehsan

Publication Date
2020

Peer reviewed|Thesis/dissertation

UNIVERSITY OF CALIFORNIA

Los Angeles

Hydrogel-Based Bioadhesives for Tissue Engineering and Surgical Applications

A dissertation submitted in partial satisfaction of the

requirements for the degree Doctor of Philosophy

in Chemical Engineering

by

Ehsan Shirzaei Sani

2020

ABSTRACT OF THE DISSERTATION

Hydrogel-Based Bioadhesives for Tissue Engineering and Surgical Applications

by

Ehsan Shirzaei Sani

Doctor of Philosophy in Chemical Engineering

University of California, Los Angeles, 2020

Professor Nasim Annabi, Chair

Sutures, wires, and staples constitute the conventional standard of care for reconnecting tissues after surgical procedures to restore their structure and function. These methods generally have several limitations. For example, they are time-consuming and may cause further tissue damage and lead to infection. In addition, they may not provide immediate and adequate sealing to stop body fluid and air leakages. Using adhesive biomaterials is a suitable alternative for wound closure due to their characteristics, such as simple and painless application, and short implementation time. In this regard, various types of surgical materials have been used for sealing, reconnecting tissues, or attaching devices to the tissues. Based on the final application and the anatomical parts involved in the medical intervention, it is important to design these tissue adhesives with some specific characteristics such as: i) high biocompatibility, ii) easy and rapid application, iii) strong adhesion to the target tissue, iv) biomimetic mechanical properties, v) permeability to nutrients and gases, vi) supporting tissue regeneration, and vii) antimicrobial properties in the case of infected wounds. However, commercially available surgical adhesives have many drawbacks and generally only possess one of the properties mentioned above. In this project, we aimed to combine different types of highly biocompatible biopolymers (e.g. gelatin, elastin like polypeptides, and hyaluronic acid)

with different nanomaterials to engineer novel bioadhesives with the combined properties mentioned above. These biopolymers were first chemically modified to form photocrosslinakble hydrogels through a short exposure to visible light in the presence of a highly biocompatible photoinitiator (Eosin Y). The engineered adhesives exhibited tunable physical properties and could be tailored for a variety of surgical and tissue engineering applications. As the first step of the project, a flexible and transparent gelatin-based adhesive was designed for corneal tissue sealing and repair. The mechanical properties of the engineered hydrogel adhesive were optimized to mimic the stiffness of the native cornea. In addition, the formulation of the adhesive was modified to obtain high adhesion to the cornea, while retaining appropriate biodegradability and high cytocompatibility *in vitro*. Our data showed that the engineered hydrogel adhesives had higher adhesive strength than commercially available adhesives used for cornea such as ReSure® (Ocular Therapeutix, Inc., USA), based on standard adhesion tests by the American Society for Testing and Materials (ASTM). In addition, *ex vivo* tests on explanted rabbit eyes demonstrated that the adhesives possessed high retention and were resistant to burst pressure. Furthermore, *in vivo* tests were conducted using a rabbit stromal cornea defect model to test the biocompatibility and retention of the biomaterial, as well as corneal regeneration after the application. In the second part of this proposal, we modified our engineered hydrogels to fabricate multifunctional adhesives through incorporation of different drugs and nanomaterials. In particular, we engineered antimicrobial adhesives by incorporating ZnO nanoparticles (NPs) or antimicrobial peptides (Tet213) to the structure of the biopolymer prior to photopolymerization. In addition, we showed that the incorporation of laponite (disc shaped silicate NPs) could lead to the formation of osteoinductive adhesives that can be used for a wide range of applications, such as bone and dental tissue engineering. These multifunctional adhesive hydrogels exhibited high biocompatibility,

mechanical stability and tissue integration in different animal models such as subcutaneous implantation in rats, and a mouse calvarial defect model. Our engineered multifunctional adhesives with tunable physical and adhesive properties can be used as a platform for sealing and repair of various tissues such as bone, lung, skin, and arteries.

The dissertation of Ehsan Shirzaei Sani is approved.

Andrea Armani

Andrea M. Kasko

Harold G. Monbouquette

Nasim Annabi, Committee Chair

University of California, Los Angeles

2020

To my beloved father, mother, sisters, and brothers:

Because I owe it all to you. Thank you for everything!

Table of Content

Abstract of the Dissertation……ii
Dedication……..vi
Acknowledgements.…… …..xvii
Vita……...…….xx
INTRODUCTION…….…….1
1. **CRITICAL LITERATURE REVIEW**…….……4
1.1. Theory and Mechanism of the adhesion…….……4
1.1.1. Mechanical Interlocking…….……..5
1.1.2. Intermolecular Bonding…….……...…..…5
1.1.3. Chain Entanglement……..……...…..….6
1.1.4. Electrostatic Bonding……..……...……...7
1.2. Synthetic Polymer as Tissue Adhesives…….……..……...…8
1.2.1. Polycyanoacrylates Adhesives……...…….....8
1.2.2. PEG–based Adhesives…….……...……..11
1.2.3. Dendrimer-based Adhesives……..14
1.3. Naturally Derived Tissue Adhesives…….……..……...…..…15
1.3.1. Protein-based Adhesives…….……...……15
1.3.2. Fibrin and Fibrinogen-based Adhesives…….……...…..……16
1.3.3. Serum Albumin-based Adhesive…….……...……17
1.3.4. Collagen and Gelatin-based Adhesives…….…….....….....18
1.3.5. Silk-based Adhesives…….……...…....21
1.4. Polysaccharide-based Adhesives…….……...……21
1.4.1. Chondroitin-based Adhesives…….……..22
1.4.2. Dextran-based Adhesives…….……..……24
1.4.3. Hyaluronic Acid-based Adhesive…….……..……24
1.5. Summary…….……..……25
2. EXPERIMENTAL……..…….……...…26
2.1. Synthesis of Photocrosslinkable Adhesive Hydrogels for tissue engineering and surgical

applications…….27
2.1.1. Synthesis of gelatin methacryloyl (GelMA)…….. ……27
2.1.2. Synthesis of methacrylated hyaluronic acid (MeHA)…….……..…27
2.1.3. Expression and synthesis of elastin like polypeptide (ELP)……....…27
2.2. Fabrication of Adhesive hybrid hydrogels…….…….……28
2.2.1. Fabrication of MeHA/ELP hybrid hydrogels…….…….….28
2.2.2. Fabrication of visible light crosslinked GelMA-based hybrid hydrogels…..…...28
2.3. Mechanical characterization of the engineered hydrogels……...…29
2.4. In vitro adhesion tests……...……29
2.5. In vitro swellability of the adhesive hydrogels……...…….31
2.6. Pore size determination…….……31
2.7. In vitro cell studies……....……31
2.7.1. Cell lines……...……31
2.7.2. 2D cell seeding on adhesive hydrogels…….32
2.7.3. 3D cell encapsulation within the engineered hydrogels……...…….32
2.7.4. Determination of cell proliferation……..…..…….33
2.7.5. Determination of cell viability……...33
2.7.6. Determination of cell adhesion and spreading…….…..…..34
2.7.7. Histological evaluation of the chondrogenic differentiation of 3D encapsulated hMSCs …….…….….34
2.8. Determination of in vitro antimicrobial activity of adhesive hydrogels……...….35
2.8.1. Bacteria seeding on adhesive hydrogels……...…..35
2.8.2. Colony-forming units (CFU) assay……...….35
2.8.3. BacLight™ live/dead assay……36
2.8.4. SEM imaging of bacterial clusters on adhesive hydrogels……36
2.9. Animal studies……...…36
2.9.1. Rabbit corneal surgeries……36
2.9.2. Subcutaneous implantation of the adhesive hydrogels in rats……...…37
2.9.3. Mouse calvaria defect model…….38
2.9.4. Ligature induced peri-implantitis model in minipigs. …….38
2.9.5. Histological and immunofluorescent evaluation of in vivo biocompatibility …..40

2.10. Statistical analysis……41
3. RESULTS……...41
3.1. Highly Elastic and Flexible Adhesive hydrogels for Surgical and Tissue Engineering Applications……...…41
3.1.1. Synthesis and structural characterization of photocrosslinkable adhesive hydrogels……41
3.1.2. Synthesis and physical characterization of adhesive hydrogels…….....44
3.1.3. *In vitro* adhesive properties of GelCORE adhesive hydrogels……..51
3.1.4. *Ex vivo* retention and burst pressure resistant of the engineered bioadhesives….55
3.1.5. In vitro assessment of cytocompatibility and integration of adhesive hydrogels..58
3.1.6. *In vivo* assessment of biocompatibility and biointegration of engineered adhesive hydrogel in injury model……61
3.2. Multifunctional Photocrosslinkable Adhesive Hydrogels for Surgical and Tissue Engineering Applications……..….68
3.2.1. Antimicrobial Adhesive Hydrogels……70
3.2.1.1. Synthesis of MeHA/ELP hybrid hydrogels……..73
3.2.1.2. Mechanical characterization of MeHA/ELP hybrid hydrogels…….…….76
3.2.1.3. *In vitro* adhesive properties of MeHA/ELP hydrogels……79
3.2.1.4. Pore characteristics and swelling ratios of MeHA-ELP hybrid hydrogels…..…80
3.2.1.5. *In vitro* cytocompatilbity and chondrogenic differentiation of 3D encapsulated hMSCs in MeHA/ELP hydrogels…….....83
3.2.1.6. *In vitro* antibacterial properties of the hybrid hydrogels……88
3.2.1.7. *In vivo* biodegradation and biocompatibility of the engineered MeHA-ELP hybrid hydrogels……...91
3.2.2. Osteoinductive and antimicrobial adhesive hydrogels……95
3.2.2.1. Synthesis and physical characterization of the adhesive hydrogels…..……99
3.2.2.2. Physical characterization of adhesive hydrogels…….99
3.2.2.3. *In vitro* and *ex vivo* adhesive properties of the engineered hydrogels……..103
3.2.2.4. *In vitro* antimicrobial properties of adhesive hydrogels……..106
3.2.2.5. Cell studies……..……..108
3.2.2.6. *In vivo* evaluation of implanted bioadhesives hydrogels……..……112

3.3. Engineering an osteoinductive and antimicrobial bioadhesive hydrogels for treatment of peri-implantitis and periodontal bone defects…….……117

3.3.1. Physical characterization of composite bioadhesive hydrogels…….120

3.3.2. *In vitro* antimicrobial properties of composite bioadhesive hydrogels …….121

3.3.3. *In vitro* cytocompatibility and differentiation studies ……...…….123

3.3.4. *In vivo* biocompatibility and biodegradation of composite bioadhesives …….127

3.3.5. *In vivo* bone forming capacity of composite bioadhesives …….129

3.3.6. *In vivo* of composite bioadhesives in a ligature induced peri-implantitis model in miniature pigs ……130

4. Conclusion……..…….....139

6. References……...141

List of Figures

Figure 1. Different chemical/physical bonds formed between adhesive and surrounding tissues [5]…...6

Figure 2. (A) Polymerization and (B) degradation reactions of cyanoacrylate-based adhesives [5]…….9

Figure 3. Schematic illustration of application, and crosslinking of a bioadhesive which shows biointegration of adhesive hydrogel (dark blue) to cartilage tissue (light blue) using functionalized CS, which covalently binds biomaterial to cartilage tissue……22

Figure 4. Synthesis, application, and *in vitro* characterization of GelCORE adhesive hydrogels. (a) Schematic of the chemical reaction for GelCORE formation and photocrosslinking of the prepolymer solution with Eosin Y (photoinitiator), TEA (co-initiator) and VC (co-monomer). **(b)** Schematic diagram for the application of GelCORE for rapid and long-term repair of corneal injuries which include **(i)** formation of stromal defect, **(ii)** application of the bioadhesive, **(iii)** regeneration of the epithelial layer and **(iv)** stromal regeneration. **(c)** The prepolymer solution is injected into the corneal defect and exposed to visible light, forming **(d)** an adhesive GelCORE hydrogel. **(e)** Representative compressive stress-strain curves, **(f)** compressive (Young's) moduli, and **(g)** elastic moduli of GelCORE adhesive hydrogels fabricated using 5%, 10%, and 20% (w/v) total polymer concentration with varying photocrosslinking time points. **(h)** Water content of GelCORE adhesives produced by using 20% (w/v) polymer concentration and varying visible light exposure times at 37 ºC in DPBS over time. **(i)** *In vitro* degradation of 20% (w/v) GelCORE adhesive (4 min photocrosslinking time), in different concentrations of collagenase type II solution in DPBS and 37 ºC over time. All hydrogels were polymerized by using 0.1 Mm Eosin Y, 1.5% (w/v) TEA and 1% (w/v) VC in distilled water. Data are reported as mean ± SD (*p<0.05, **p<0.01, ***p<0.001, ****p<0.0001 and n ≥ 3)……...…….…….46

Figure 5. ***In vitro* adhesion properties of GelCORE hydrogels using porcine skin and intestine as biological substrates. (a)** Schematic of the modified test for burst pressure measurements (ASTM F2392-04) and **(b)** average burst pressure of GelCORE adhesives (n ≥ 3) produced with varying polymer concentrations, photocrosslinking times, compared to two commercial adhesives including Evicel® and CoSEAL™. **(c)** Schematic of the modified test for lap shear strength measurements (ASTM F2255-05) and **(d)** average shear strengths of GelCORE adhesives (n ≥ 3) produced with varying polymer concentrations and photocrosslinking times, Evicel®, and CoSEAL™. **(e)** Schematic of the modified test for wound closure test (ASTM F2458-05) and **(f)** average adhesive strengths of GelCORE adhesives (n ≥ 3) produced with varying polymer concentrations and photocrosslinking times, compared to Evicel® and CoSEAL™. Data are means ± SD (*p < 0.05, **p < 0.01, ***p < 0.001, ****p < 0.0001)..…..…… …….52

Figure 6. *Ex vivo* application and adhesion properties of GelCORE adhesives. **(a)** Representative slit lamp photographs from rabbit eyes sealed by GelCORE bioadhesive, and **(b)** retention times of GelCORE bioadhesives, formed at various crosslinking times and prepolymer concentrations, on cornea tissues. **(c)** OCT images after *ex vivo* application of GelCORE adhesives to rabbit corneas at days 1, 14 and 28 after

application. **(d)** Schematic of *ex vivo* burst pressure set up, including a syringe pump, a pressure sensor and a recording system. **(e)** Average burst pressure of GelCORE adhesives formed by varying photocrosslinking time, compared to a commercially available ocular sealant, ReSure® (control). Data are represented as mean ± SD (*p<0.05, **p<0.01, ***p<0.001, ****p<0.0001, n ≥ 4)……..…… …….56

Figure 7. *In vitro* cytocompatibility of GelCORE bioadhesives. Representative live/dead images from corneal fibroblast cells seeded on **(a)** tissue culture well-plate, **(b)** GelCORE adhesives, and **(c)** ReSure sealant on day 1, 4 and 7 post seeding (scale bar = 100 μm). **(d)** Quantification of cell viability on GelCORE bioadhesives compared to tissue culture well-plate and ReSure after 1, 4, and 7 days of culture. **(e)** Quantification of metabolic activity of corneal fibroblast cells seeded on control (tissue culture well-plate), GelCORE hydrogels, and ReSure after 1, 4, and 7 days. Representative live/dead images of corneal fibroblast cells grown on **(f)** tissue culture well-plate and **(g)** GelCORE hydrogels on a 2D scratch assay at days 0, 1 and 3 after scratching. **(h)** Quantification of relative cell densities migrated to the scratched area on GelCORE adhesives and control samples, at days 0, 1, 2, and 3. GelCORE hydrogels at 20% (w/v) final polymer concentration were used for 2D cell culture studies (photocrosslinking time: 4 min). Data is represented as mean ± SD (**p < 0.01, ***p < 0.001 and ****p < 0.0001, n ≥ 3)…….60

Figure 8. *In vivo* application of GelCORE bioadhesives into corneal defects in rabbits. **(a-b)** Representative images for creating a 50%-depth corneal stromal defect on rabbit eye. **(c)** *In situ* application of GelCORE prepolymer solution into corneal defect. **(d)** Photocrosslinking and **(e)** formation of a transparent GelCORE adhesive hydrogel on corneal stromal defect. AS-OCT images **(f)** before and **(g)** after treatment with GelCORE. 7 days after application, the bioadhesive still had a smooth surface. GelCORE hydrogels were prepared by using 20% (w/v) total polymer concentration and 4 min light exposure time……...63

Figure 9. Corneal re-epithelialization after *in vivo* application of the bioadhesive to corneal defects in rabbit cornea. (a) Representative slit lamp photographs and **(b)** cobalt blue with fluorescein staining after *in vivo* application of GelCORE adhesive to rabbit cornea at different time points. Progressive reduction in the size of corneal epithelial defect (green area in the central cornea) implicates epithelial migration over GelCORE……..……...…….……64

Figure 10. Histological analysis after application of GelCORE bioadhesive in a rabbit corneal stromal defect model. Representative Hematoxylin and Eosin (H&E) histopathology images from **(a)** native rabbit corneas (without defect), and **(b)** rabbit cornea after application of GelCORE in a 50%-depth stromal defect. Histological images for **(c)** untreated stromal defect (without bioadhesive), and **(d)** the defect treated with bioadhesive at day 14 post-surgery (scale bar = 50 μm, and 1 mm). **(e)** The thickness of stromal layer for the native cornea, GelCORE-treated, and untreated eyes at day 14 post-surgery obtained from histological images. **(f)** The thickness of epithelial layer for native cornea, GelCORE treated and untreated eyes at day 14 post-surgery obtained from histological images. **(g)** Representative fluorescent immunohistochemical image (DAPI and CD45 marker) **(i)** from the area without defect, and **(ii)** from corneal stromal defect treated with GelCORE bioadhesive at day 14 post-surgery. GelCORE hydrogels were prepared at 20% (w/v) total polymer concentration and 4 min light exposure time.……..……..……66

Figure 11. Schematic of MeHA/ELP hydrogel formation and chemical structure. (a) HA

methacrylation process to form MeHA, **(b)** chemical structure of ELP, indicating the presence of cysteine residues, and **(c)** schematic diagrams of photocrosslinking of MeHA/ELP hydrogels and potential application of the cell-laden adhesive biocomposite……...74

Figure 12. **Mechanical and adhesive properties of photocrosslinkable MeHA/ELP hybrid hydrogels. (a)** Representative compressive cyclic stress–strain curves of MeHA/ELP hydrogels produced by using different ELP concentrations and 2% MeHA. **(b)** Compressive modulus and **(c)** Energy loss of MeHA/ELP hydrogels produced by using different MeHA and ELP concentrations. **(d)** Elastic modulus, **(e)** ultimate tensile stress and **(f)** ultimate tensile strain of MeHA/ELP hydrogels produced using different MeHA and ELP concentrations. **(g)** burst pressure resistance and **(h)** lap shear strength values for MeHA/ELP hybrid hydrogels(* $p < 0.05$, ** $p < 0.01$, **** $p < 0.0001$)…… ……..….77

Figure 13. **Pore characteristics and swelling properties of photocrosslinked MeHA/ELP composite hydrogels.** Representative SEM images from the cross sections of the MeHA/ELP hydrogels produced by using 1% MeHA and **(a)** 0, **(b)** 5, **(c)** 10, and **(d)** 15% (w/v) ELP concentrations; and 2% MeHA and **(e)** 0, **(f)** 5, **(g)** 10, and **(h)** 15% (w/v) ELP concentrations (scale bar = 100 μm). **(i)** Effect of MeHA and ELP concentrations on the average apparent pore sizes of MeHA/ELP gels calculated from SEM images. Swelling ratios of hydrogel produced by using various ELP concentrations and (**j)** 1% or **(k)** 2% (w/v) MeHA at 37 °C in DPBS (* $p < 0.05$, ** $p < 0.01$, *** $p < 0.001$, **** $p < 0.0001$)…….82

Figure 14. ***In vitro*** **3D encapsulation and differentiation of mesenchymal stem cells (MSCs) inside MeHA/ELP hybrid hydrogels.** Representative live/dead images of MSCs encapsulated within MeHA/ELP hydrogels after **(a)** 1 and **(b)** 5 days. Representative phalloidin (green)/DAPI (blue) stained images of cell-laden MeHA/ELP hydrogels after **(c)** 1 and **(d)** 5 days. Quantification of **(e)** cell viability and **(f)** metabolic activity RFU (relative fluorescence intensity) of MSC laden hydrogel using live/dead and PrestoBlue assays on days 1, 3, and 5 post encapsulation. Representative images of Alcian blue stained from MSC-laden MeHA/ELP hydrogels to visualize glycoproteins of differentiated cells at days 1, 14, and 35 post encapsulation.…… ……...…86

Figure 15. ***In vitro*** **bacterial seeding on MeHA/ELP-ZnO hydrogels with different ZnO concentrations.** Representative SEM images of methicillin-resistant Staphylococcus aureus (MRSA) colonization on MeHA/ELP-ZnO hydrogels containing **(a, b)** 0% ZnO, **(c, d)** 0.1% ZnO and **(e, f)** 0.2% ZnO. Clusters of bacteria are shown in dashed circles. **(g)** Representative live/dead images from bacteria seeded MeHA/ELP-ZnO hydrogels containing **(g)** 0% ZnO, **(h)** 0.1% ZnO, and **(i)** 0.2% ZnO after 1 day of incubation. Hydrogels were formed by using 2% MeHA and 10% ELP at 120 sec UV exposure time...89

Figure 16. ***In vivo*** **biocompatibility and biodegradation of MeHA/ELP hybrid hydrogels in a rat subcutaneous implantation model**. **(a)** Representative images of MeHA/ELP hydrogels before implantation (day 0) and on days 4, 14, 28, 56 post-implantation. **(b)** *In vivo* biodegradation of MeHA/ELP hydrogels on days 0, 4, 14, 28 and 56 of implantation, based on weight and volume loss of the implants (n = 4). The *in vivo* degradation profile of MeHA/ELP hydrogels shows an approximately linear degradation behavior by volume during the first 56 days after implantation, as well as the highest biodegradation by weight between days 14 and 28. Hematoxylin and eosin (H&E) staining of MeHA/ELP sections (hydrogels with the surrounding tissue) after **(c)** 4 days, **(d)** 28 days, and **(e)** 56 days of implantation (scale bars = 500

μm). Immunohistofluorescent analysis of subcutaneously implanted MeHA/ELP hydrogels showing no significant local lymphocyte infiltration (CD3) at days **(f)** 4, **(g)** 28 and **(h)** 56 post-implantation (scale bars = 200 μm). Fluorescent images showed transient macrophage infiltration (CD68) at day 4 **(i)**, followed by no apparent positive fluorescence at days **(j)** 28 and **(k)** 56 post-implantation (scale bars = 200 μm). Green, red and blue colors in **(f-k)** represent the MeHA/ELP autofluorescent hydrogels, the immune cells, and cell nuclei (DAPI), respectively. ……...……...…92

Figure 17. Physical characterization of bioadhesive hydrogels. (A) Synthesis and photocrosslinking process of bioadhesive hydrogels. **(B)** Elastic and Young's modulus, **(C)** extensibility, and **(D)** ultimate stress of the adhesive hydrogels produced by using 7% and 15% (w/v) total polymer concentration with and without AMP. **(E)** *In vitro* degradation properties and **(F)** swelling ratios in Dulbecco's phosphate buffered saline (DPBS) for 7% and 15% (w/v) adhesive hydrogels with and without AMP. Data are represented as mean ± SD (*$p < 0.05$, **$p < 0.01$, ***$p < 0.001$, ****$p < 0.0001$ and $n \geq 5$)……...100

Figure 18. *In vitro* and *ex vivo* adhesion properties of GelAMP hydrogels. (A) Representative images of wound closure test using pig gingiva tissue based on ASTM standard test (F2458-05) and **(B)** adhesion strength of bioadhesive hydrogels and a commercially available adhesive (CoSEAL™) to porcine gingiva. **(C)** Schematic of the *in vitro* lap shear test based on a modified ASTM standard (F2255-05), using titanium as a substrate. **(D)** The *in vitro* lap shear strength of the bioadhesive hydrogels at 7% and 15% polymer concentration and a commercially available adhesive (CoSEAL™). ……....104

Figure 19. *In vitro* antibacterial properties of bioadhesive hydrogels against *p. gingivalis*. (A) Representative images of *p. gingivalis* colonies grew on blood agar plates for bioadhesives with and without AMP. **(B)** Quantification of colony forming units (CFUs) for bioadhesive hydrogels with and without AMP (0.2% (w/v)), seeded with *p. gingivalis bacteria* (day 4). Representative scanning electron microscope (SEM) images of *p. gingivalis* colonization on bioadhesive hydrogels containing **(C)** 0% and **(D)** 0.2% AMP. Clusters of bacteria are shown with yellow arrows. (***$p < 0.001$ and ****$p < 0.0001$)……106

Figure 20. *In vitro* 3D encapsulation of W-20-17 cells and mouse calvarial bone sutures inside adhesive hydrogels. (A) Representative live/dead images of W-20-17 cells encapsulated within bioadhesives hydrogels with and without AMP after 1 and 5 days. **(B)** Quantification of viability of W-20-17 cells incorporated within hydrogels without (control) and with AMP (GelAMP) using live/dead assays on days 1, 3, and 5 post encapsulation. **(C)** Representative phalloidin (green)/DAPI (blue) stained images of cell-laden bioadhesive with and without AMP after 1 and 5 days. **(D)** Quantification of metabolic activity of W-20-17 cells encapsulated in hydrogels after 1, 3, and 5 days. **(E)** Schematic diagram of the extraction and encapsulation of mouse calvarial bone sutures in 3D hydrogel network. **(F)** Representative images of calvarial bone sutures encapsulated within 7 % and 15% (w/v) bioadhesives to visualize growth and diffusion of cells at days 10, 20 and 30 post encapsulation. **(G)** Quantification of metabolic activity of migratory stromal cells from encapsulated bone sutures. Hydrogels were formed at 120 sec visible light exposure time (** $p < 0.01$, *** $p < 0.001$), **** $p < 0.0001$)…… ……110

Figure 21. *In vivo* evaluation of bioadhesive hydrogels using a mouse calvarial defect model. (A) Schematic diagram of *in situ* application of bioadhesive hydrogels in a mouse calvarial defect model. **(B)** 7% and 15% bioadhesive hydrogels were delivered to artificially created bone defects in mouse calvaria

(yellow arrowheads), and photopolymerized for 1 min using a commercially available dental curing light. 7 and 14 days after implantation, samples remained in place, without any sign of detachment. **(C)** Histological evaluation (H&E staining) of the 15% (w/v) bioadhesives at day 0 post implantation. Representative H&E images for **(D)** 7% (w/v) and **(E)** 15% (w/v) bioadhesive treatment, and **(F)** untreated sample after 42 days post implantation. …. ……114

Figure 22. Quantitative evaluation of new bone formation using µCT analysis. (A) Representative micro-CT images for untreated defect, and defects treated with 7% and 15% bioadhesives on days 28 and 42 post-implantation **(B)** Quantitative analysis of bone surface area and **(C)** and bone volume. Data are represented as mean ± SD (*p < 0.1, **p < 0.01, ***p < 0.001, ****p < 0.0001, n=5)..…….. …..…117

Figure 23. Physical characterization of bioadhesive hydrogels. (A) Synthesis and photocrosslinking process of bioadhesive hydrogels. **(B)** Young's and **(C)** Elastic modulus, and **(D)** extensibility of the adhesive hydrogels produced by using 15% (w/v) total polymer concentration and different SN content. **(E)** *In vitro* degradation properties and **(F)** swelling ratios in Dulbecco's phosphate buffered saline (DPBS) for 7% and 15% (w/v) adhesive hydrogels with and without AMP.....……...……...…….. …..…119

Figure 24. *In vitro* and *ex vivo* adhesion properties of adhesives hydrogels. (A) Adhesion strength of bioadhesive hydrogels and a commercially available adhesive (CoSEAL™) to porcine gingiva based on ASTM standard wound closure test (F2458-05). **(B)** The *in vitro* lap shear strength of the bioadhesive hydrogels and a commercially available adhesive (CoSEAL™) on titanium substrate, based on a modified ASTM standard (F2255-05). Data are represented as mean ± SD … ……..…..… …….. ……121

Figure 25. *In vitro* antibacterial properties of bioadhesive hydrogels against different aerobic/anerobic and G+/- bacteria. (A) Quantification optical density (OD) growth of *p. gingivalis* bacteria cultured in different solutions with and without AMP, and a commercial antibiotic (SMZ-TMP) as control. **(B)** Quantification of colony forming units (CFUs) for bioadhesive hydrogels with and without AMP (0, o.1, 0.2, and 0.4 % (w/v)), seeded with *p. gingivalis bacteria* (day 4). Quantification of colony forming units for bioadhesive hydrogels with and without AMP (0.4 % (w/v)), seeded with **(C)** *MDR e. coli*, **(D)** *MRSA* and **(E)** *staphylococcus aureus.* (*p < 0.05, **p < 0.01 and ****p < 0.0001). ….. …..…122

Figure 26. *In vitro* cytocompatibility and proliferation of hMSCs. (A) Representative live/dead images of hMSCs cells seeded on the surface of antimicrobial bioadhesive hydrogels with different SN content after 1 and 5 **days**. **(B)** Representative phalloidin (green)/DAPI (blue) stained images of cells seeded on bioadhesives after 1 and 5 days. **(C)** Quantification of viability of cells seeded on the hydrogels using live/dead assays on days 1, 3, and 5 post encapsulation. **(D)** Quantification of metabolic activity of hMSCs seeded on the surface of hydrogels after 1, 3, and 5 days. …..…..……..…..……..……..…..…….. …..…124

Figure 27. *In vitro* cytocompatibility and osteogenic differentiation of hMSCs. (A) Representative fluorescent images of calcian AM (green: live) and ethidium homodimer I (red: dead) for hMSCs seeded on the surface of well-plate (control), bioadhesive hydrogels containing AMP, with and without SNs, and Bio-OSS bone graft after 7 and 15 days. Representative images of **(B)** Alcian Blue, **(C)** Alizarin Red, and **(D)** Von Kossa staining for hMSCs seeded on the surface of well-plate (control), bioadhesive hydrogels containing AMP, with and without SNs, and Bio-OSS bone graft after 7 and 15 days. …..…..……..…..…126

Figure 28. *In vivo* biocompatibility and biodegradation of hydrogels in a rat subcutaneous implantation model. (A) Representative H&E, and immunohistochemical images for **(B)** CD68 marker for detection of macrophages and **(C)** CD3 marker for detection of T cells (lymphocytes) for bioadhesives containing 0, 1000, and 10000 µg/ml SN for up to 56 days after subcutaneous implantation in rats. ….…128

Figure 29. *In vivo* evaluation of the bioadhesive hydrogels in a critical sized mandibular bone defect model miniature pig model. The representative CT images for bioadhesive hydrogels and Bio-OSS bone graft after application in a large defect in miniature pig mandible at **(A)** day 0 and **(B)** 60 post application. ….……..……..……..……..……..……..……..……..……..……..……..……..……..……130

Fig 30. Outline of the study to test the efficacy of the adhesives for PI treatment in a minipig model. …..131

Figure 31. (A) Representative images of tooth extraction process and closure of the wound in miniature pigs. **(B)** Representative CT images of the pig mandible, showing the area related to extracted teeth after 2 months healing. A tooth regrowth was observed in one defect site. …..……..……..……..……..…132

Figure 32. (A) Representative images of secondary tooth extraction process, implant placement, and closure of the wound in miniature pigs. **(B)** Representative CT images of the pig mandible, showing the implants after 2 months healing (two months after implant placement). …..……..……..……..……..…133

Figure 33. Representative images of ligature and implant abutment placement in miniature pigs, two months after implant placement. Two silk ligatures were used per implant to induce peri-implantitis through bacterial accumulation. …..……..……..……..……..……..……..……..……..……..……..……134

Figure 34. Representative photographic and CT images of the implants 3 months after ligature placement. A significant bone loss was observed around the implants. …..……..……..……..……..……..……134
Fig. 35. Representative images of implants with ligature and high plaque index, measurement of clinical parameters, mechanical debridement process, grafting with bioadhesive hydrogels, and closure of the wound in miniature pigs. ……..……..……..……..……..……..……..……..……..……..……135

Figure 36. Representative images of peri-implant defects after treatment with **(A)** bioadhesive hydrogels and **(B)** Dynablast, a commercial bone graft as control. …..……..……..……..……..……..……..……136

Figure 37. Peri-implant prosthetic parameters. **(A)** Total changes in and **(B)** change in straight buccal changes probing pocket depth (PD) values for the implants treated with bioadhesive hydrogels, and Dynablast and untreated controls. Data are represented as mean ± SD (*$p < 0.05$, $n \geq 3$). …..……..……136

Figure 38. Analysis of bone regeneration and quality. **(A)** Micro computed tomography (µ-CT) images for the implants treated with bioadhesive hydrogels, and Dynablast and untreated controls at different angels. **(B)** changes in total linear bone height calculated from CT images. **(B)** bone volume fraction (BV/TV) and **(D)** Bone surface density (BS/BV) for all the samples, calculated from µ-CT images. Data are represented as mean ± SD (*$p < 0.05$, **$p < 0.01$, ***$p < 0.001$, $n \geq 3$). …..……..……..……..……..……137

ACKNOWLEDGMENT

First, I would like to acknowledge University of California, Los Angeles, particularly the Department of Chemical and Biomolecular Engineering, for providing me with an excellent atmosphere for doing research.

A special gratitude to my supervisor, Dr. Nasim Annabi for her support.

Besides my advisor, a very special gratitude goes out to my thesis committee: Prof. Andrea Armani, Professor Andrea Kasko, Professor Harold G. Monbouquette, for all their support and guidance.

I am also grateful all the supportive people at both UCLA and Northeastern University, including Prof. Panagiotis Christofides, Dr. Flavia Pirih, Dr. Huiying Li, Prof. Behrooz Satvat, and Prof. Arthur Coury, and Dr. Giuseppe Intini who always supported me spiritually and with their incredible knowledge.

And finally, last but by no means least, also to my lab mates, who are always available in the battlefield, thank you all for your support and assistance. Thanks for all your encouragement!

Part of Chapter 1 is reprinted and adapted with permission from (G. Trujillo-de Santiago, R. Sharifi, K. Yue, E. Shirzaei Sani, S. Saheb Kashaf, M. Moisés Alvarez, J. Leijten, A. Khademhosseini, R. Dana, N. Annabi, "Ocular adhesives: Design, chemistry, crosslinking mechanisms, and applications", Biomaterials, 2019, 197, 345-367. Copyright 2019 Elsevier. Co-author contributions: All the authors contributed to writing and revision of the manuscript. N. Annabi was the P.I.

Parts of Chapter 2 and 3 are reprinted and adapted with permission from (E. Shirzaei Sani, R. Portillo Lara, Z. Aldawood, S. H. Bassir, D. Nguyen, Alpdogan Kantarci, G. Intini, N. Annabi, "An Antimicrobial Dental Light Curable Bioadhesive Hydrogel for Treatment of Peri-Implant Diseases", Matter (Cell Press), 2019, 1, 4, 926-944. Copyright 2019 Elsevier. Co-author contributions: R. Portillo Lara helped with ex vivo tissue culture and writing. Z. Aldawood, S. H. Bassir, and G. Intini helped with *in vivo* calvarial model. D. Nguyen and Alpdogan Kantarci helped with antimicrobial studies on *P. gingivalis*. N. Annabi was the P.I.

Parts of Chapter 2 and 3 are reprinted and adapted with permission from (E. Shirzaei Sani, A. Kheirkhah, D. Rana, Z. Sun, W. Foulsham, A. Sheikhi, A. Khademhosseini, R. Dana, N. Annabi, Sutureless repair of corneal injuries using naturally derived bioadhesive hydrogels, Science Advances, 2019, 5, eaav1281. Copyright 2019 American Association for the Advancement of Science. Co-author contributions: A. Kheirkhah, Z. Sun, and W. Foulsham helped with *in vivo* corneal model in rabbits. D. Rana and A. Sheikhi helped with adhesion and mechanical characterization. R. Dana and N. Annabi were the P.Is.

Parts of Chapter 2 and 3 are reprinted and adapted with permission from (E. Shirzaei Sani, R. Portillo-Lara, I. Noshadi, W. Yu, B. M. Geilich, A. Spencer, T. J. Webster, and N. Annabi, “Engineering adhesive hyaluronic acid/elastin like polypeptide hybrid hydrogels for tissue engineering applications”. ACS Biomaterials Science. Copyright 2019 3 American Chemical Society. Co-author contributions: R. Portillo Lara helped with writing. A. Spencer, I. Noshadi, W. Yu, and B. M. Geilich helped with physical characterization and antimicrobial assays. T. J. Webster provided antimicrobial facility. N. Annabi was the P.I.

VITA

2018-2020	Graduate Student Researcher Department of Chemical and Biomolecular Engineering, UCLA
2015-2018	Graduate Student Researcher Department of Chemical Engineering, Northeastern University
2012	M.S. in Chemical Engineering, Sharif University of Technology, Iran
2010	B.S. in Chemical Engineering, University of Sistan and Baluchestan, Iran

Selected Publications

Book Chapter

1. R. Portillo-Lara*, **E. Shirzaei Sani***, N. Annabi, "Biomimetic orthopedic materials" in "Orthopedic Biomaterials – Advances and Applications", **2017**. Springer, pp. 109-139. (*Equal contribution)

Journal Articles

1. D. Mohsen, **E. Shirzaei Sani**, A. Youssef, A. M. Soliman, N. Zandi, E. Mostafavi, N. K. Alam, N. Annabi, "Bioactive and elastic nanocomposites with antimicrobial properties for bone tissue regeneration". *ACS Applied Biomaterials*, **2020**, 3, 5, 3313–3325.

2. **E. Shirzaei Sani**, R. Portillo Lara, Z. Aldawood, S. H. Bassir, D. Nguyen, Alpdogan Kantarci, G. Intini, N. Annabi, "An Antimicrobial Dental Light Curable Bioadhesive Hydrogel for Treatment of Peri-Implant Diseases", *Matter (Cell Press)*, **2019**, 1, 4, 926-944.

3. A. R. Spencer, **E. Shirzaei Sani,** J. R Soucy, C. C Corbet, A. Primbetova, R. A Koppes, N. Annabi, "Bioprinting of a cell-laden conductive hydrogel composite", *ACS applied materials & interfaces,* **2019,** 11, 34, 30518-30533.

4. **E. Shirzaei Sani**, A. Kheirkhah, D. Rana, Z. Sun, W. Foulsham, A. Sheikhi, A. Khademhosseini, R. Dana, N. Annabi, Sutureless repair of corneal injuries using naturally derived bioadhesive hydrogels, *Science Advances*, **2019**, 5, eaav1281.

5. B. Saleh, H. Kaur Dhaliwal, R. Portillo Lara, **E. Shirzaei Sani**, R. Abdi, M. Amiji, N. Annabi "Local immunomodulation using an adhesive hydrogel loaded with miRNA-laden nanoparticles promotes wound healing", *Small*, **2019,** 15, 36, 1902232.

6. G. Trujillo-de Santiago, R. Sharifi, K. Yue, **E. Shrizaei Sani**, S. Saheb Kashaf, M. Moisés Alvarez, J. Leijten, A. Khademhosseini, R. Dana, N. Annabi, "Ocular adhesives: Design, chemistry, crosslinking mechanisms, and applications", *Biomaterials*, **2019**, 197, 345-367.

7. **E. Shirzaei Sani**, R. Portillo-Lara, I. Noshadi, W. Yu, B. M. Geilich, A. Spencer, T. J. Webster, and N. Annabi, "Engineering adhesive hyaluronic acid/elastin like polypeptide hybrid hydrogels for tissue engineering applications". *ACS Biomaterials Science & Engineering*, **2018**. [Featured on the cover of journal]

8. J. R. Soucy, **E. Shirzaei Sani**, D. Diaz Vera, R. Portillo Lara, F. Dias, S. M. Mithieux, A. S. Weiss, A. N. Koppes, R. A. Koppes, N. Annabi, " Photocrosslinkable Gelatin/Tropoelastin Hydrogel Adhesives for Peripheral Nerve Repair", *Tissue Engineering part A***, 2018**.

9. M. M Fares, **E. Shirzaei Sani**, R. Portillo Lara, R. B Oliveira, A. Khademhosseini, N. Annabi, "Interpenetrating network gelatin methacryloyl (GelMA) and pectin-g-PCL hydrogels with tunable properties for tissue engineering", *Biomaterials science*, **2018**, 6, 11, 2938-2950

10. N. Annabi*, Y. Zhang, A. Assmann, **E. Shirzaei Sani**, G. Cheng, A.D. Lassaletta, A. Vegh, B. Dehghani, G. U. Ruiz-Esparza, X. Wang, Sidhu Gangadharan, A.S. Weiss, Ali Khademhosseini*, "Engineering a highly elastic human protein-based sealant for surgical applications", *Science Translational Medicine,* **2017**, 9(410). [Featured on the cover of journal, News coverage]

11. N. Annabi, D. Rana, **E. Shirzaei Sani**, R. Portillo-Lara, J. L. Gifford, M. M. Fares, S.M. Mithieux, A.S. Weiss, "Engineering a sprayable and elastic hydrogel adhesive with antimicrobial properties for wound healing", *Biomaterials*, **2017**, 139, pp. 229-243.

Introduction

Sutures and staples have been widely used to reconnect incisions for recovering tissue structure and function. They hold tissues in close proximity in order to facilitate healing and resist applied mechanical loads. Although they are commonly used after surgery, these methods are not sufficient for many clinical applications, especially to prevent the leaking of liquids from incisions. Sealing wound tissue using sutures and staples can also be challenging, time consuming, and may not be possible in regions of the body that are not readily accessible. Additionally, piercing tissues in order to place sutures and staples can further damage the surrounding wound area, and can increase the risk for infection. Sealant materials have attracted attention as alternatives to seal and reconnect tissues, or incorporate implant devices into tissues due to their ease of application and versatility. Surgical sealants combined with sutures have been reported to more effectively seal wounds than sutures alone, and provide a reduced infection rate and patient blood loss. To successfully develop sealants for the clinical practice, materials must provide adequate mechanical and adhesive properties for sealing the incision site without limiting tissue function, movement, or causing adverse effects. In addition, in order to avoid the introduction of multiple foreign materials in the recipient and additional lesions caused by sutures and staples, it would be desirable to develop sealants that work effectively on elastic and fragile tissues without requiring the prior application of sutures or staples.

An ideal adhesive should meet a number of characteristics depending on their specific application and the anatomical parts involved in the medical intervention. Generically, it should be biocompatible, non-toxic, comfortable for the patient, easily and rapidly applied, be able to attach to the ocular tissue, quickly seal the injured area, mimic the mechanical properties of the tissue, be permeable to nutrients and gases and offer a microbial barrier. Specific applications,

such as corneal sealing, demand other characteristics like transparency and a refractive index similar to the cornea. Some other applications such as Peri-implant diseases (PIDs), require multifunctional bioadhesives which not only must be biocompatible and biodegradable, but also must possess antimicrobial and osteoinductive properties. Additional general desirable characteristics include cost-effectiveness, long storage stability, and the possibility of incorporating drugs or biological compounds [1-3].

Using adhesive biomaterials is a suitable alternative for wound closure due to their characteristics, such as simple and painless application, and short implementation time. In this regard, various types of surgical materials have been used for sealing, reconnecting tissues, or attaching devices to the tissues. Based on the final application and the anatomical parts involved in the medical intervention, it is important to design these tissue adhesives with some specific characteristics such as: i) high biocompatibility, ii) easy and rapid application, iii) strong adhesion to the target tissue, iv) biomimetic mechanical properties, v) permeability to nutrients and gases, vi) supporting tissue regeneration, and vii) antimicrobial properties in the case of infected wounds. However, commercially available surgical adhesives have many drawbacks and generally only possess one of the properties mentioned above.

In this project, we aimed to develop new class of adhesive biomaterials for different surgical applications. The main goal is to engineer adhesive hydrogels that possess some characteristics such as high biocompatibility, easy and rapid application, strong adhesion to the target tissue, biomimetic mechanical properties, permeability to nutrients and gases, supporting tissue regeneration, and antimicrobial properties in the case of infected wounds.

In particular, the aims of this research will be summarized as follows:

- Chemical modification of naturally derived biopolymers such as gelatin, elastin like polypeptides (ELPs), and hyaluronic acid (HA), and PEG in order to fabricate photocrosslinkable/non-photocrosslinkable adhesive hydrogels
- Engineering novel and multifunctional bioadhesives by incorporating different nanomaterials into biopolymer structure. These multifunctional adhesives can be used for different surgical applications such as cornea, lung, bone, cartilage and dental applications.
- Engineering antimicrobial and drug loaded bioadhesives for a variety of surgical applications, using antimicrobial metal oxides and AMPs.

The engineered adhesive hydrogels particularly examined in some surgical applications as follow:

- Engineering a flexible and transparent gelatin-based adhesive for corneal tissue sealing and repair which possess tunable mechanical stability and physical properties similar to the stiffness of the native cornea. Also, it is needed to be highly adhesion to the cornea, while retaining appropriate biodegradability and high cytocompatibility *in vitro*. Finally, the adhesive hydrogels must possess high biocompatibility and retention as well as corneal regeneration after the application. To do this, a rabbit stromal cornea defect model was used.
- In the second part of this proposal, the goal is to fabricate multifunctional adhesives through incorporation of different drugs and nanomaterials. In particular, first we engineered antimicrobial adhesives by incorporating ZnO nanoparticles (NPs) or antimicrobial peptides (Tet213) to the structure of the biopolymer prior to photopolymerization. The suggesting application of this adhesive hydrogel was cartilage tissue repair.

- The multifunctional adhesive hydrogels developed in previous sections will be further modified by incorporation of SNs in order to induce osteoinductivity of the hydrogels. These adhesives can be used for a wide range of applications, such as bone, and dental tissue engineering.
- These multifunctional adhesive hydrogels exhibited high biocompatibility, mechanical stability and tissue integration in different animal models such as subcutaneous implantation in rats, and a mouse calvarial defect model. Our engineered multifunctional adhesives with tunable physical and adhesive properties can be used as a platform for sealing and repair of various tissues such as bone, lung, skin, and arteries.

1. CRITICAL LITERATURE REVIEW

In this section, we first review the adhesion mechanism of the adhesive materials to the host tissues. We then review a spectrum of tissue engineering adhesives going from synthetic materials (cyanoacrylates, PEG-based and dendrimers) to natural based ones (proteins and polysaccharides). We cover fundamental biomaterial aspects such as chemical nature, preparation methods, and physicochemical properties. We focus our discussion on the advantages and challenges of these materials as adhesives based on clinical and scientific reports.

1.1. Theory and Mechanism of the adhesion

An adhesive is usually liquid or semi-liquid material, that can adhere the surfaces of two or multiple objects together when applied and it can resist against separating forces. A variety of mechanisms for adhesion and bioadhesion have been investigated and reported in literatures, which can be categorized into four main mechanisms including mechanical interlocking, chemical

bonding, diffusion theory, and electrostatic theory [1-3]. Generally, in the actual environments, a combination of various mechanisms takes place, although the adhesion may predominantly arise from one of these mechanisms. In this section, the most dominant adhesion mechanisms are briefly discussed.

1.1.1. Mechanical Interlocking

Mechanical interlocking is a mechanism of adhesion in which the adhesive material infiltrates into the pores, microscopic surface roughness, and irregularities of objects' surfaces and mechanically lock and bond the surfaces of the substrates together. Amalgam, which is traditionally used for filling the tooth cavities is a well-known example of this mechanism. In mechanical interlocking method, the surface pretreatment is crucial in order to obtain the required surface topography for highest adhesion. However, there are reports that showed good adherence between smooth surfaces. Thus, the significant role of mechanical interlocking in adhesion is still uncertain [4, 5].

1.1.2. Intermolecular Bonding

Intermolecular bonding is the main mechanism of adhesion between adhesive materials and substrates, which is caused by intermolecular (or interatomic) forces and the bonds between atoms/molecules of adhesive material on one side and the atoms/molecules on the surface of the substrates on the other (e.g. chemical bonds, primary interactions or secondary forces). Several types of chemical bonds or primary forces (e.g. covalent, ionic, and metallic bonds) can be formed in the interface of the adhesive and the substrate. Due to high energy of the primary bonds, they usually provide a strong adhesion. However, formation of strong primary bonds sometimes requires chemical modification of the surface as well as incorporation of specific groups into the chemical structure of adhesive, using primers, coupling agents and adhesion promoters [6-8].

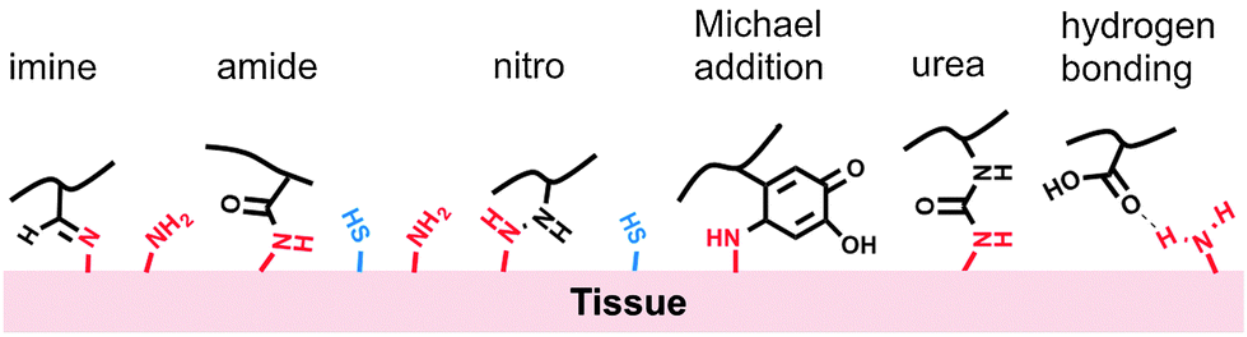

Figure 1. Different chemical/physical bonds formed between adhesive and surrounding tissues [4].

Secondary forces including hydrogen bonds, π–π stacking forces, dipole-dipole interactions, and van der Waals forces also play an important role in the adhesion mechanism. Although the strength of secondary forces is significantly lower than primary bonds, these types of interactions are the main considerable adhesion mechanism in many adhesion systems especially in the cases that the number of sites for secondary forces is comparatively higher than other type of forces. In some studies, a several approaches have been examined to describe the mechanism of the adhesion between adhesive and substrate. Basically, the physical forces are attributed to electron donor–acceptor interactions. For example, Lewis acid and base as well as hydrogen bond can be considered as electron donor – acceptor interactions. The donor and acceptor properties enable molecules to form molecular bonding complexes that assist formation of tougher adhesions [9-11]. Generally, chemical bonding such as primary and secondary bonds or a combination of both is the most important mechanism of adhesion between bioadhesive and tissue as substrate. In Figure 1 represents different chemical or physical bonds (primary and secondary) which can form between adhesive and surrounding tissues.

1.1.3. Chain Entanglement

Chain entanglement theory particularly has been proposed to describe the adhesion of two similar polymers as well as binding between two different polymers. Based on this mechanism,

macromolecules of the polymer diffuse mutually into the contact interface (with a approximate thickness of 1–100 nm), to form a layer of interpenetrated polymer chains. To occur the chain entanglement, the polymer macromolecules must possess enough mobility. Therefore, the chain entanglement does not happen in highly crosslinked or crystalline polymers. Also, amorphous polymers below their glass transition temperature do not show any chain entanglement due to lack of sufficient molecule mobility. Moreover, the interdiffusing macromolecules should be mutually soluble in each other. Diffusion mechanism has been also used in some bioadhesive systems to explain some adhesion phenomena [12]. For instance, in mucoadhesive drug delivery systems, the main bioadhesion mechanism is because of interpenetration of glycoproteininc network of mucus and the adhesive polymer chains. This diffusion of macromolecules into the glycoproteins network takes place when the polymer chains are transported to close contact and it is highly depended on the interface topological features, diffusion coefficient, chemical potential coefficient, and the solubility parameters of adhesive material and glycoproteins [13].

1.1.4. Electrostatic Bonding

Electrostatic bonding is another mechanism of adhesion which generally happens when two materials with different electronic charges get close together. In this case, transferring electrons happens to balance the Fermi levels, which causes the formation of a double layer of electron charge in the interface of the adhesive and the substrate and induces the electrostatic forces. Generally, electrostatic forces appear in some metals and semi-conductors due to presence of charged double layers. However, this mechanism does not appear in bioadhesion of non-metallic systems [13,14]. One example of this mechanism in bioadhesive systems is electron transfer in the contact area between adhesion between bioadhesives and glycoprotein of mucus due to electron transfer [15,16].

In the next section, the most common adhesive biomaterials (e.g. synthetic and naturally derived) used for surgical applications will be briefly introduced.

1.2. Synthetic Polymer as Tissue Adhesives

Adhesives engineered from synthetic biomaterials are one of the major bioadhesives that have been used in several biomedical and surgical applications. These materials possess different characteristics such as high tunability of the chemical composition, mechanical and physical characterizations, adhesive properties, and degradation kinetics, to be used in different surgical applications. Synthetic adhesives also exhibit additional advantages such as ease of production, high purity, and low cost. Cyanoacrylates and polyethylene glycol (PEG) derivatives are the most common synthetic bioadhesives, which will be briefly introduced in this section.

1.2.1. Polycyanoacrylates Adhesives

Polycyanoacrylates, or simply cyanoacrylates (also called superglue), are a group of synthetic and versatile tissue adhesives which have been utilized n as superglues in general household uses or as bioadhesives in biomedical and surgical applications [5]. Cyanoacrylates were used for the first time for wound closure in the early 1960s [6]. In the past decades, these adhesives repeatedly used for many surgical applications such as: closure of topical skin incisions, trauma-induced skin lacerations, microbial barrier and blocking the passage of blood, body fluids or air [5, 6]. In addition, cyanoacrylates are extensively used by ophthalmologists in ocular surgeries, although their application for any biomedical application has not been approved by FDA till today [7]. For instance, they are used as an off-label in wound repair [8-15], leaking blebs [16-21], retinal detachment [22-25], stromal thinning repair [26], corneal descemetoceles [27], and exposure

keratopathy [26, 28], scleral reinforcement [29], punctual occlusion [30, 31], blepharoplasty [32-34] and temporary tarsorrhaphy [26, 35, 36].

Cyanoacrylates are monomeric alkyl esters of α-cyanoacrylic acid, which can be catalytically polymerized through a condensation reaction between alkyl cyanoacetate and formaldehyde (Figure 2a)[5] [37]. Generally, cyanoacrylates have a high tendency to participate in polymerization reactions via an anionic or zwitterionic mechanism. These polymerization reactions are initiated through a nucleophilic attack by weak bases such as water, amines (amino acids), as well as alcohols, which are present in the living tissues, and can later propagate to form alkyl methacrylate polymers [38]. In the case of surgical applications, the initiation reaction by amino acid residues of proteins is key for the fast strong binding of cyanoacrylate adhesives to tissues [39]. This strong binding, as well as suitable biomechanical strength and quick polymerization (*i.e.* within 10 s to 60 s), make cyanoacrylates as attractive adhesives for different biomedical applications.

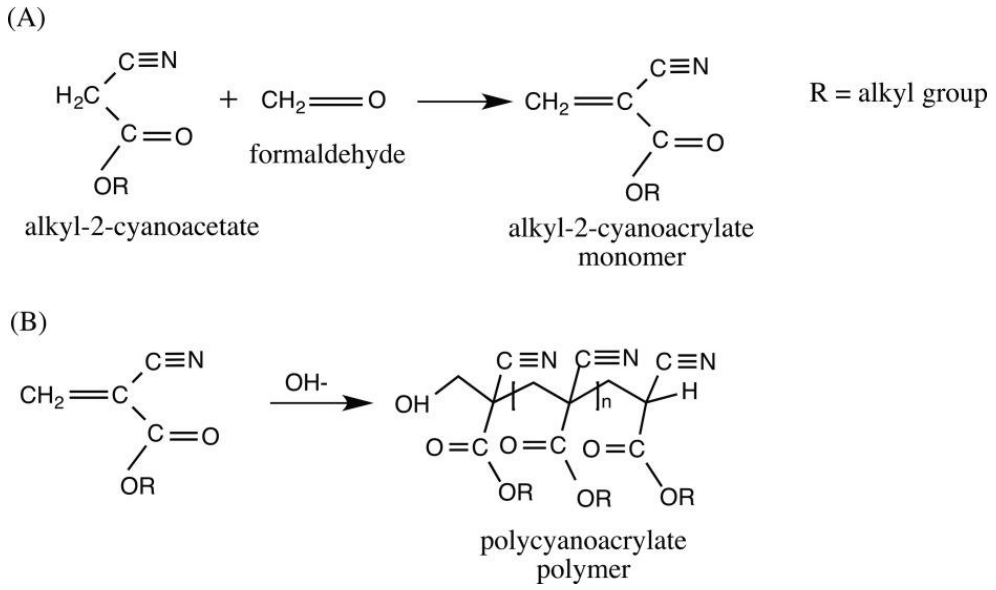

Figure 2. (A) Polymerization and (B) degradation reactions of cyanoacrylate-based adhesives [5].

Polycyanoacrylate adhesives offer a fast, operative, relatively inexpensive and easy closure and treatment of wounds (if used correctly) [5]. However, its use has been associated with several drawbacks including discomfort to the patient, cytotoxicity, uncontrollable polymerization, irregular rough surfaces, exothermic reaction, inflammatory responses, inhibit of collagen remodeling and wound healing, and even pancreatic tumor development [6]. In addition, these adhesives generally work effectively on dry surfaces. Moreover, they are not generally biodegradable and there are some safety concerns related to their degradation products. Also, their application is limited to topical usages [5].

Cytotoxicity is one of the biggest challenges related to cyanoacrylates adhesives and it has been frequently reported as a significant drawback of this class of adhesives especially those with short side chains such as methyl and ethyl groups [40]. The presence of these groups causes the rapid degradation of the adhesives into cyanoacetate and formaldehyde (Figure 2b) [5], which can accumulate in tissues and induce acute and chronic inflammation [7, 41]. Several derivatives of cyanoacrylate esters (e.g. *n*-butyl, *n*-heptyl, methoxypropyl, and octyl cyanoacrylates), have been developed to reduce cytotoxicity and polymerization rate [42, 43]. It has been reported that cyanoacrylates with shorter alkyl chains exhibited higher reactivity, faster degradation rate and higher cytotoxicity effects on tissues compared to those with longer alkyl chains [44]. Moreover, it has been reported that the tissue binding strengths of cyanoacrylate adhesives were inversely correlated with the lengths of alkyl side chains (*e.g.*, butyl cyanoacrylate had a greater binding strength than octyl cyanoacrylate) [45].

Further modification of polycyanoacrylate based adhesives is needed to eliminate many of the side-effects associated with applications in biomedical and surgical fields. Moreover, engineering hybrid materials composed of cyanoacrylates and biocompatible polymers can be

envisioned to afford better bioadhesives with enhanced biocompatibility.

1.2.2. PEG–based Adhesives

Another group of frequently used tissue adhesives in medical sciences is based on poly(ethylene glycol) (PEG). These bioadhesives are favorable due to high water solubility, low protein adhesion, nontoxicity, biocompatibility, and generally cannot be easily recognized by the immune system (nonimmunogenic) [6]. In addition, the PEG backbone can be easily modified with chemical functional groups, which makes it very versatile. For example, several functionalization techniques have been reported to synthesize PEG hydrogels with different biochemical cues, and in order to tune their biodegradability and biomechanical properties [46-48]. This flexibility of the applications make PEG based adhesives very attractive for different surgical applications such as sealing suture lines, vascular graft, cerebrospinal fluid (CSF), corneal defects and lung defects [6]. In this section, we review PEG-based materials, those already in clinical use, and others currently under research and development.

Different PEG-based adhesives approved by FDA to be used in surgical applications. For instance, ReSure® is PEG-based bioadhesive which is the only FDA approved sealant for ocular tissues. This product particularly approved for sealing clear corneal incision (CCI) wound leaks, as well as preclusion of fluid egress after cataract surgery [49]. ReSure® sealant developed as a two components kit, 4-arm PEG with NHS-terminated backbones and trilysine amine solution as crosslinker. These two components can quickly form a stable hydrogel after mixing (less than 30 sec). It has been shown by clinical studies that ReSure® has significant advantages over sutures. For example, it can tolerate higher intraocular pressures (11-29 mmHg) [50], and it is more effective in averting fluid egress in cataract surgery, and also in single-plane incisions (*i.e.* 4.1% and 34.1% for ReSure® and suture groups respectively) [49] as well as prevention of the

recurrence of epithelial ingrowth [51]. This bioadhesive possesses several advantages such as comfort to the patient, good healing, and lubricious properties elimination of virus transmission. However, some drawbacks and disadvantages have been reported for ReSure. For instance, it is a two components-based adhesive which requires mixing before the application. In addition, the polymerization reaction is very fast (14–17 s), which make its application challenging for the ophthalmologist. Furthermore, ReSure has a limited application to only seal not actively leaking incisions. Also, it has a very short stability after the application (>3 days) [52].

FocalSeal is another FDA approved PEG-based adhesive which is a nontoxic, non-immunogenic and bioabsorbable polyethylene glycol (PEG) based synthetic hydrogel, which can be photopolymerized by blue-green light particularly for air leakage sealing post lung surgery [53]. The clinical result shows 77% of patients treated with FocalSeal have no postoperative air leak, compared to 9% of control group [6]. However, the photochemical polymerization has three-step delivery requiring application of a primer layer followed by a PEG-based adhesive material and subsequent light exposure [5]. Therefore, engineering a single component sealant, which does not need a primer for better adhesion might be more suitable for thoracic surgery.

Other approaches for production of PEG-based hydrogels have been reported in the literature for other surgical applications. One approach is fabrication of three-dimensional (3D) crosslinked hydrogel networks due to easy chemical modifications of PEG backbones. For example, PEG backbones can be chemically functionalized with acrylate, methacrylate, or other groups suitable for free radical polymerization. These functionalized PEG macromolecules can be photopolymerized in the presence of photoinitiators (e.g. Eosin Y or Irgacure 2959), upon exposure to visible light [46] or ultra violet (UV) light [54] and form 3D hydrogel network [55].

PEG backbones also can be functionalized with nucleophilic groups, which are capable to

react quickly with electrophilic groups of another martial. However, it is challenging to find the appropriate nucleophile-electrophile reaction which can rapidly goes forward under physiological conditions without generating any toxic by-product. Furthermore, these reactions need very high degree of chemoselectivity among the designed nucleophile-electrophile pairs, due to the presence of different competitive functional groups such as amines, thiols, hydroxyls, and carboxylates of the native tissues. This can interfere or effect the crosslinking reaction.

Different parameters can affect mechanical and biological characteristics of PEG-based adhesive hydrogels including polymer concentration, molecular weight, and crosslinking technique and chemical functionalities. For example, in the photocrosslinkable adhesive systems, visible light crosslinking is usually advantageous over UV light lower cytotoxicity risks and also higher penetration into the bulk of hydrogel or tissue. It has been reported that polymer concentration play an important role in mechanical properties as well as cell spreading and viability. Generally, by increasing prepolymer concentration, the adhesive stiffness and modulus enhances, which normally results lower cell viability [56]. Molecular weight of the PEG prepolymer is another factor that can affect cell viability, mechanical properties as well as swellability of PEG based hydrogels such as PEGDA and PEGMA. This particularly affect the crosslinking density of the resulting adhesive hydrogel. For example, physical properties of PEGDA hydrogels can be extensively tuned by altering PEG molecular weight, which makes them suitable for different surgical applications such as lung sealing and ophthalmology. PEG-based hydrogels are known to inhibit non-specific binding of cells. However, enhanced cell interactions with PEG hydrogels can be achieved via chemical modification to introduce peptide cell binding motifs. For example, PEGDA hydrogels can be modified by a Michael addition of cysteine-bearing RGD peptides to enable specific RGD-integrin attachment of HCECs. This flexibility of chemical

modification might provide more functions of PEG-based adhesives.

Although PEG-based bioadhesives exhibited many advantages such as fast crosslinking reaction, good adhesion to different tissues, high biocompatibility, non-toxic degradation products, and low to moderate inflammatory response, some concerns and drawbacks have been reported about their applications including high water uptake capacity (> 400% of the original volume), which needs more caution especially in the case of applying to closed spaces in order to eliminate excess pressure build up on the surrounding tissues (e.g., nerve compression)[6]. Furthermore, the application of the adhesive is more effective on relatively dry surfaces which makes it difficult to apply in many surgical systems [5].

1.2.3. Dendrimer-based Adhesives

Dendrimers are generally repetitive hyperbranched macromolecules (polymers), which possess unique physicochemical properties including multifunctionality, highly tunable chemical structures, monodispersed molecular weights, and high surface area to volume ratio [57-60]. These characteristics made them attractive biomaterials in the field of surgical sealants and adhesives [61, 62]. A dendrimer can be synthetized by the chemical condensation of successive layers of monomers (divergent synthesis) from a central moiety, or by the synthesis of multiple branches to later fuse them to a central core (convergent synthesis). In any case, the result is a highly symmetric and hyper-branched macromolecule that is structurally composed of three main zones: the central core, the internal branching layers, and the peripheral moieties [61, 63, 64].

One or more simple chemical compounds as well as many natural metabolic compounds are suitable monomer candidates for synthesizing dendrimers. For instance, natural metabolites including amino acids, such as lysine, valine, and leucine [60], sugars [65], α-hydroxy acids, fatty acids [63], and chemical intermediates found in metabolic pathways, such as succinic acid, fumaric

acid, citric acid, and pyruvic acid [66, 67] are among the appropriate monomers for the formation of dendrimers. In addition to these small-molecule monomers, PEG-based macromers, polycaprolactone (PCL), and polytrimethylene carbonate (TMC), suggest additional structural flexibility resulting higher tunability to be used in different biomedical and surgical applications [1].

1.3. Naturally Derived Tissue Adhesives

1.3.1. Protein-based Adhesives

Protein-based adhesives are another group of commercially available tissue adhesives and sealants used for surgical and clinical application. These biomaterials can readily crosslink in the presence of suitable crosslinking agent, and at the same time form strong covalent bonds with the tissue surface. Proteins has high potential to be used as surgical adhesives, due to their natural source, and some other advantages over synthetic-based adhesives that will be explained in this section.

In addition, other groups also used protein-based materials to repair ocular tissues. So far, several natural proteins such as fibrin, collagen, gelatin, and silk [68], have been studied with the aim of repairing or sealing ocular wounds. Some of these materials have received FDA approval for use as tissue adhesives (but not for ophthalmological us specifically), and some, mainly fibrin-derived products, have become well-established commercial products. Examples are Cryoseal (Thermogenesis, CA, USA), Evicel (Johnson & Johnson, NJ, USA), Tisseel and Artiss (Baxter, CA, USA), and BioGlue (Kennesaw, GA, USA) [69]. Vitagel (Orthovita, PA, USA), a system to prepare fibrin glue from the patient blood, was recently approved and launched. Many other protein-based sealants are still at the research and development stage.

1.3.2. Fibrin and Fibrinogen-based Adhesives

One of the most widely used family of surgical sealants are fibrin sealants or glues which is basically based on the biological process of fibrin clot formation. Fibrin is an elastic and filamentous protein produced through the catalyzed reaction of the enzyme thrombin with fibrinogen. This reaction naturally takes place in the last stages of the coagulation cascade, forming an interacting fibrous network or blood clog. Chemical structure and functionalities of the fibrin and fibrinogen [70-73], and the process of clot formation have been described in detail in literature [74]. These adhesives have been used for different surgical applications: as an assistant to hemostasis in cardiopulmonary bypass surgeries or treatment of splenic injuries, used simultaneously with by conventional surgical techniques to control the bleeding, hemostasis on the incised liver surface, sealing lung defects as well as corneal repair [5].

Fibrin glue (sealant) typically is composed from two major components, thrombin (bovine or recombinant) and fibrinogen (generally derived from human plasma), which rapidly form a crosslinked adhesive hydrogel upon mixing [5]. These bioadhesives have shown fast curing, biocompatibility, biodegradability, and re-absorbability *in vivo* [75, 76]. The adhesive strengths of fibrin sealants, as measured by the lap shear method, range from 1 kPa to 27.9 kPa as a function of fibrin concentration and gelation time. For example, a 7.2 mg/mL fibrin glue rendered a clot with an adhesive resistance of 1 kPa after gelation for 5 min, whereas a 34.5 mg/mL fibrin glue showed an enhanced resistance of 27.9 kPa at a gelation time of 90 min [77]. In general, the adhesive strengths of fibrin glues are lower than other crosslinked protein-based biomaterials, but are sufficient for a vast range of ocular applications.

Despite the mentioned advantages, fibrin-based adhesives still have some important drawbacks such as risk of transferring blood-borne disease, allergic reactions, viral contamination

and infection, long process of synthesis and batch-to-batch product variations, requiring ancillary equipment, insufficient tissue adhesion and relatively high price [5, 78].

1.3.3. Serum Albumin-based Adhesive

Albumins are another group of natural proteins that have been extensively used for developing tissue adhesives. Serum albumin is the most abundant component of the mammalian blood, is a globular and highly water-soluble protein in the range of 66.5-65.0 kDa. Human serum albumin is a multicomponent protein which contains 585 amino-acid residues, 17 pairs of disulfide bridges, and one free cysteine [79]. The 3D structure of human serum albumin has been resolved [80]. Progel is another FDA-approved pleural air leak sealant which is based on human serum albumin and a PEG crosslinker [6]. Progel has been introduced to the market to be used in lung procedures only in conjunction with sutures for better sealing. Trials with pulmonary resection patients showed that Progel application in conjunction with suturing and stapling was superior to the use of suturing and stapling only. However, the high cost of human-based albumin and the potential for disease transmission, due to the fact that it is a blood-derived product, are concerns with Progel. Another limitation of Progel is that it lacks a pro-hemostatic function, which may cause additional problems when applying the sealant to bleeding wounds. As a result of this, only 35% of patients treated with Progel after pulmonary resection were found to be air-leak free [5, 6]. Albumin-based adhesives have been also considered for cornea repair applications. For instance, BioGlue (Cryoline Inc.) [69], is a commercially available albumin-based adhesive approved by the FDA as a sealant for cardiac surgeries in 1999, has also been used for ophthalmic surgeries. This adhesive is composed of 45% bovine serum albumin (BSA) and 10% glutaraldehyde as a crosslinking agent. Glutaraldehyde promotes covalent bonds between the lysine residues of both albumin and the tissue, resulting high mechanical stability and strength [81]. However, using

glutaraldehyde is associated with several biological risks. First, unreacted glutaraldehyde is highly cytotoxic [82]. In addition, the serum albumin normally extracted from animal sources which may also propose immunological risks. The use of recombinant versions of human serum albumin (*i.e.*, produced in Pichia pastoris) might contribute to overcome safety concerns and reduce batch-to-batch variability of albumin-based sealants and procedures [83, 84]. Overall, the experimental evidences suggest that albumin-based adhesives are an appropriate family of biomaterials for different surgical applications. However, the safety concerns related to animal sources of albumin require resolution due to immunological problems, while recombinant based albumins are not generally cost-effective.

1.3.4. Collagen and Gelatin-based Adhesives

Collagen is the main structural protein and the most abundant protein in the extracellular matrix (ECM) of the the connective tissues in mammalians. Therefore, as expected, collagen-based materials have been explored extensively for engineering of surgical adhesives. The chemical structure, architecture and physiochemical and physiological properties of collagen fibrils have been widely studied elsewhere [85-87].

In addition to “native collagen welding,”, the collagen originated from animal sources as well as recombinant-based collagens have also been fabricated in different ways to produce surgical adhesives; *i.e.*, films or coatings [88-90], soldering [91], hydrogels [92], and vitrigels [93]. Collagen-coated surfaces exhibit good properties as substrates for the adhesion and proliferation of corneal epithelial cells. Kim *et al.* reported that transparent poly(lactic-co-glycolic acid) (PLGA) films coated with collagen type I were suitable for use as a substratum for corneal tissue regeneration or inclusively as a material for artificial corneas for transplantation [88]. Collagen has been also developed as a soldering material for different surgical applications such as corneal

repair and wound healing [91, 94]. For instance, Noguera *et al.* developed a collagen-based laser-activated solder to repair corneal wounds [91]. Solder patches, fabricated by casting a concentrated solution of chemically modified collagen, followed by freeze drying, were used to repair incisions of 2 and 3 mm made *ex vivo* on rabbit corneas. The chemically modified collagen used to fabricate the patches was prepared by reacting bovine or porcine collagen I with glutaric anhydride. The free amines within the collagen chain reacted with the anhydride to produce a material that underwent a thermal transition between 40 and 45 °C and had a sufficient number of carboxylic groups to crosslink with the cornea tissue upon exposure to low intensity laser light. Other collagen-based adhesives including collagen crosslinked with transglutaminase [95], collagen-immobilized vinyl alcohol scaffolds to support epithelium growth [96], collagen-based hydrogel scaffolds [92, 97], PEG-stabilized carbodiimide crosslinked collagen–chitosan hydrogels [98], alginate microsphere-collagen hydrogels [99], recombinant collagen versions [100], collagen–phosphorylcholine interpenetrating network hydrogels [101], collagen- and glycopolymer-based hydrogel [102], and collagen hydrogels crosslinked with carbodiimides [103] also have been used for different surgical and tissue engineering applications.

Gelatin, the partially hydrolyzed form of collagen, is another promising candidate for surgical applications. This biopolymer is highly water-soluble and can be crosslinked by different methods in order to develop naturally derived adhesives and hydrogels with appropriate properties for surgical applications and tissue regeneration. For example, our group has synthesized a novel composite class of elastic and antimicrobial adhesive hydrogels, for the clinical management of chronic nonhealing wounds using two biopolymers derived from native ECM proteins, gelatin and tropoelastin [104]. These adhesives were photocrosslinked via exposure to visible light due to chemical functionalization of the prepolymer backbones (methacrylation). Moreover, the

incorporation of antimicrobial peptide Tet213 into the adhesive hydrogels, instilling antimicrobial activity against Gram (+) and (-) bacteria. The physical properties (e.g. porosity, degradability, swellability, mechanical, and adhesive properties) of the engineered hydrogel could be fine-tuned by varying the ratio of MeTro/GelMA and the final polymer concentration. The engineered adhesive hydrogels supported *in vitro* mammalian cellular growth in both 2D and 3D cultures. The subcutaneous implantation of the hydrogels in rats confirmed their biocompatibility and biodegradation *in vivo.*

Our group also introduced another gelatin-based sealant with promising characteristics such as low cost, high adhesion to the native tissue, high biocompatibility, and biodegradability using UV-crosslinkable gelatin methacryloyl (GelMA). The adhesive hydrogels showed tunable physical properties and high adhesion superior to clinically used fibrin- and poly(ethylene glycol)-based glues. Chronic *in vivo* experiments in small as well as translational large animal models proved GelMA to effectively seal large lung leakages without the need for sutures or staples, presenting improved performance as compared to fibrin glue, poly(ethylene glycol) glue and sutures only. Furthermore, high biocompatibility of GelMA sealant was observed, as evidenced by a low inflammatory host response and fast *in vivo* degradation while allowing for adequate wound healing simulateneously. Combining these results with the low costs, ease of synthesis and application of the material, GelMA sealant is envisioned to be commercialized not only as a sealant to stop air leakages, but also as a biocompatible and biodegradable hydrogel to support lung tissue regeneration.

Gelatin-microbial transglutaminase (gelatin-mTG) is another gelatin-based adhesive which is used as an adhesive for ophthalmic applications [105-107]. Yamamoto *et al.* inferred vitrectomy with artificial posterior vitreous detachment (PVD) followed by retinal tear and detachment to

rabbits [105]. Then, the authors used a Gelatin-mTG complex to treat the animals. After administration, the material adhered and sealed retinal tears for several days without noticeable inflammatory reaction. Chen *et al.* conducted additional *in vitro* adhesion studies on bovine retinal tissue using a similar gelatin-mTG biomimetic material and reported lap shear strength at wet conditions ranging from 15 to 45 kPa [107]. These values were comparable to those reported for other soft-tissue glues, suggesting that mTG-crosslinked gelatin may be an efficacious, friendly, and safe adhesive for ophthalmic applications.

1.3.5. Silk-based Adhesives

Another group of protein-based adhesive used for surgical applications are silk-based biomaterials [68, 108]. For example, photocrosslinkable silk fibroin proteins has been used using visible light as light source and vitamin B (riboflavin) as a photoinitiator [68]. The engineered adhesive material exhibited possessed many characteristics needed for flexible tissues such as cornea. This bioadhesive exhibited good transparency, high adherence to the native cornea, and tunable elastic modulus (200-500 Pa).

1.4. Polysaccharide-based Adhesives

Polysaccharides are another important fa of biopolymers, including chitin and chitosan, dextran or chondroitin. represent various biopolymers that are ubiquitously found in living organisms. Polysaccharides are composed of a variety of monosaccharides and generally have linear or branched structural building blocks. Biochemical and physiochemical properties of polysaccharides can be tuned by changing the compositions of sugar monomers, functional groups, and varying chemical crosslinking agents[5]. These biomaterials typically can be extracted from animal or plants. Therefore, they are generally biocompatible and biodegradable, which makes them suitable for different applications in pharmaceutical, cosmetic, food, and biomedical

industries. Chondroitin sulfate, dextran, and hyaluronic acid (HA), are the most commonly used natural polysaccharides in engineering tissue adhesives for different surgical applications.

1.4.1. Chondroitin-based Adhesives

Chondroitin sulfate (CS) is a linear sulfated polysaccharide (glycosaminoglycan) composed of varying ratios of *N*-acetylgalactosamine and glucuronic acid units. Conjugation of the sulfate groups can take place at different functional sites along the chain with different degree of functionalization. This material is one of the key components of the cartilage tissues in mammalians body. The long-term biosafety of CS has been well documented. Therefore, it is widely used as a dietary supplementary element to prevent and treat osteoarthritis, although its medical effects are not clinically approved.

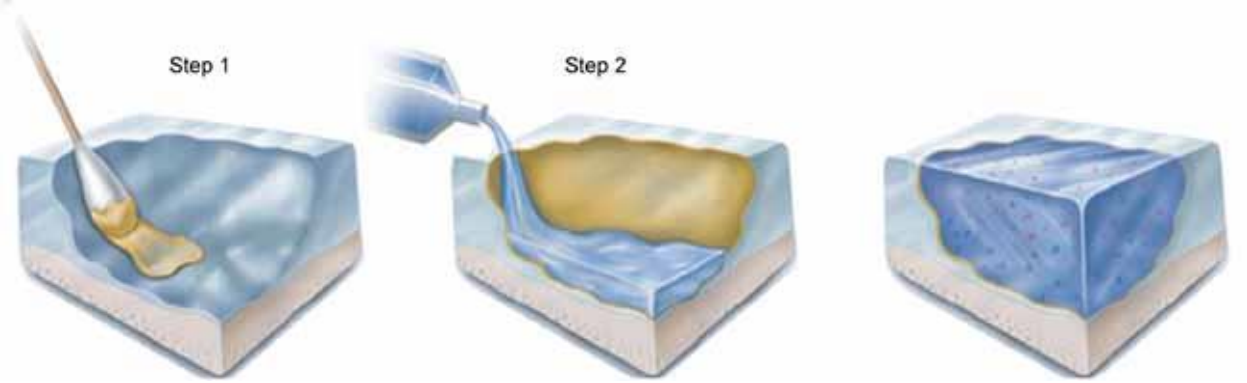

Figure 3. Schematic illustration of application, and crosslinking of a bioadhesive which shows biointegration of adhesive hydrogel (dark blue) to cartilage tissue (light blue) using functionalized CS, which covalently binds biomaterial to cartilage tissue surface [109].

Different chemical modification techniques have been used to engineer CS-based adhesives for a variety of biomedical applications. For instance, Elisseeff *et al.* developed a reaction system between CS and glycidyl methacrylate to engineer methacrylated CS derivative that can be photopolymerized [110]. Physical properties Byof the adhesives could be tuned by varying different parameters such as degree of functionalization, prepolymer concentration, and

photocrosslinking conditions. Furthermore, the adhesive hydrogels exhibited high cytocompatibility and metabolic activity using 3D encapsulated chondrocytes, which showed the potential application of the adhesives in cartilage tissue engineering.

In another study, using reactive aldehyde groups of sodium periodide as crosslinking agents, CS was crosslinked via amine groups and formed an adhesive hydrogel (Figure 3) [109]. This adhesive hydrogel was used as an adhesive layer between the implanted biomaterials and native cartilage tissues has been demonstrated, which showed strong adhesion and stable integration (over five weeks *in vivo*) to repair wounded cartilage tissues [111]. NHS-activated chondroitin sulfate derivative has also been reported by Strehin and Elisseeff *et al.*, which could react with amine-bearing PEG crosslinkers to form stable hydrogels with amide linages. In addition, when applied to tissues, the NHS-ester groups could also react with amine groups on tissue surfaces, suggesting enhanced tissue adhesion and applications in regenerative medicine [112, 113].

These bioadhesives have the capability of sealing small incisions of the NHS-activated CS/amine-PEG adhesive in *ex vivo* and *in vivo* swine models. Tested on a 6.0-mm defect made in the swine cornea, this chondroitin sulfate-based adhesive was able to restore maximum IOP greater than 200 mmHg. The adhesive was also showed to be non-toxic to major types of cells found in the cornea. In addition, histological results demonstrated minimal inflammatory response and no scar formation after two weeks of application [112, 113].

Based on these results, the CS-based adhesives showed promising candidates in different tissue engineering applications such as cartilage and ophthalmic tissue repair. The excellent biosafety of CS, superior surgical performance, and the versatile chemistry for tailored properties of the adhesives are the desirable advantages of CS-based tissue adhesive.

1.4.2. Dextran-based Adhesives

Dextran is another polysaccharide that has certain branches along a linear chain. The main linear part is composed of glucose via the alpha-1,6-linkages. Since dextran lacks multiple reactive substitutional groups such as amine and carboxylic acid groups, the application of this biomaterial in surgical fields is limited and requires further chemical modifications. The most common chemical modification of dextran is based on the controlled oxidation reaction by periodide which has also reported for chondroitin sulfate. Subsequently, the oxidized aldehyde-containing dextran derivatives could react with amine-bearing crosslinkers to form hydrogels via the imine linkage formation. Other options include photocrosslinkable dextran derivatives with methacrylate groups [114] and enzyme-responsive dextran materials with tyramine motifs [115].

The engineered dextran-based adhesive was also tested in a sutureless automated lamellar therapeutic keratoplasty setup to evaluate its ability to fix grafts. A three-month *in vivo* study in a rabbit model proved that the graft sealed to corneal remained clear and attached for 90 days, Epithelialization on the glued graft was observed within 7 days with no indication of apparent signs for inflammation or scarring. This study demonstrated that dextran-based adhesives are easy alternative techniques in treating corneal diseases [116].

The dextran-based ophthalmic adhesives have been carefully investigated *in vitro* and *in vivo* to demonstrate their excellent performance in closing corneal wounds and fixing grafts to the ocular surfaces. The biocompatibility has been examined by histological experiments to prove that the adhesives did not induce inflammation nor interfering with tissue regeneration.

1.4.3. Hyaluronic Acid-based Adhesive

Hyaluronic acid (HA) is an anionic, nonsulfated glycosaminoglycan composed of 2-acetamide-2-deoxy-D-glucose and D-glucuronic acid units. HA plays a key role in cellular

migration in the wound healing process and it can be naturally found in connective, epithelial, neural tissues as well as the gel filled in eyes. It has also. Therefore, it is a very attractive biomaterial for the development of tissue bioadhesives, surgical sealants as well as scaffolds for different tissue engineering applications. Generally, HA-based adhesives require chemical modification of the polysaccharide backbone resulting photocrosslinkable derivatives. For instance, Grinstaff *et al.* used methacrylic anhydride in order to chemically bind methacrylate groups to the HA molecules [89]. The resulting methacrylated HA (MEHA) was photopolymerized in the presence of ethyl eosin and triethanolamine photoinitiator using a low-density argon laser (514 nm, 200 mW) to form a HA-based bioadhesive. The *in vivo* results in a rabbit corneal laceration model (3 mm defect size) corneal showed successful *in situ* polymerized and sealing the incision. No leakage was observed in more than 97% of the defects in rabbit eyes with at least 7 days sealant stability (n=38). In addition, neither *in vivo* cytotoxicity nor inflammation responses was observed. Moreover, proliferation of stromal cells and deposition of new extracellular matrix at the wound sites were observed at day 7 post surgery, suggesting rapid tissue regeneration of the sealed corneal. Moreover, the IOP values measured for this HA-based ocular adhesive were 5-10 mmHg by day 1, and increased to 10-15 mmHg by day 7. This study suggested that HA-based adhesives could also be developed for various surgical applications (i.e. ocular applications) [89]. Despite of the high biosafety and biocompatibility of HA-based adhesives, these bioadhesives have some drawbacks such as high cost, short shelf life (fast degradation), and in some cases low solubility [6].

1.5. Summary

Engineering synthetic and natural based adhesives has been extensively studied for different biomedical and surgical applications. In this section, we critically reviewed the most common

bioadhesive materials such as cyanoacrylates, PEG based adhesives, proteins and polysaccharides based adhesives. These bioadhesives possessed several advantages as well as drawbacks which mentioned in this section. Due to importance of this filed in the healthcare system, many surgcical adhesives have been introduced and undergo preclinical and clinical trials, in order to be approved by FDA as surgical adhesives. The current surgical adhesives in the market possess some advantages and disadvantages that some most common adhesives are summarized in table 1.

Table 1. Comparison of surgical adhesives/sealants on the market.

Name	Major Components	Advantages	Disadvantages
Cyanoacrylate adhesives	Cyanoacrylate monomer	- Low cost - High adhesion - Fast polymerization	- Toxic monomer - Highly rigid - Non-degradable
Bioglue (CryoLife Inc., Kennesaw, GA)	Bovine albumin and glutaraldehyde	- High adhesion - Hemostatic properties	- Toxicity of glutaraldehyde
Coseal (Cohesion Technologies, Inc., Palo Alto, CA)	Glutaryl-succinimidyl ester and thiol-terminated PEG	- Biocompatibility - Low cost	- Low adhesion (<30kPa) - Low burst pressure (<2 kPa) - Low shear strength (<70 kPa)
Fibrin-based sealants (e.g., Evicel, Ethicon Inc., Bridgewater, NJ)	Fibrinogen and thrombin	- Biocompatibility - Hemostatic properties	- Possible disease transmission from blood products - Low burst pressure (<4 kPa) - Low adhesion (<30 kPa)
FocalSeal (Genzyme, Cambridge, MA)	Eosin-based primer and PEG	- Biocompatibility - Bioabsorbable	-Additional of primer -complex delivery and crosslinking procedure
Progel™ (Davol Inc., Woburn, MA)	Human albumin and a NHS-activated PEG	- Medium burst pressure (~4 kPa) - High adhesion (~75 kPa) - High shear strength (~200 kPa)	- Possible disease transmission from blood products - High cost - High chance of recurring leaks (~65%)

2. EXPERIMENTAL

2.1.Synthesis of Photocrosslinkable Adhesive Hydrogels for tissue engineering and surgical applications

Here we describe a general method for chemical functionalization of biopolymers, in order to engineer photocrosslinkable hydrogels. To do this, we modify the polymer backbone with methacrylate or acrylate groups. This method applied to synthesize methacrylated gelatin, HA, and acrylated PEG.

2.1.1. Synthesis of gelatin methacryloyl (GelMA)

GelMA was synthesized as previously described elsewhere [117, 118]. Briefly, 10 g porcine or cold water fish gelatin (Sigma-Aldrich) was dissolved in 100 ml phosphate buffered saline (PBS) and heated at 60 °C for 30 min. Then, 8 ml methacrylic anhydride (Sigma-Aldrich) was added drop-wise to the gelatin solution under vigorous stirring at 60 °C for 3 h. The solution was then diluted with PBS and dialyzed (Spectrum Laboratories, MWCO = 12-14 kDa) against deionized water at 50 °C for 5 days to remove any unreacted methacrylic anhydride. After sterile filtration, the solutions were subsequently lyophilized for 4 days, and the final GelMA product was stored at -80 °C until experimental use.

2.1.2. Synthesis of methacrylated hyaluronic acid (MeHA)

Methacrylated HA (MeHA, molecular weight, 1.6×10^6 Da) was synthesized as described previously [119]. Briefly, methacrylic anhydride (MA) was added to a solution of 1 %(w/v) HA in deionized water (DW) and reacted on ice (4 ºC) for 24 h. During the reaction, the pH was adjusted to 8 using 5 N NaOH. The solution was then purified using dialysis tubes (MW cutoff 6-8 kDa) against DW for 48 h. Lastly, the product was lyophilized and stored at -20 °C [120].

2.1.3. Synthesis of amine functionalized ZnO or laponite SN

Synthesis of 4-Aminophenyldiazonium Tetrafluoroborate solution (2.74 M): 3.71 g (34 mmol) of phenylenediamine was cooled to 0 ºC in an ice bath. 10 ml (76 mmol) of tetrafluoroboric acid solution was then added dropwise under vigorous stirring. Next, 2.2 ml (17 mmol) of tertbutylnitrite (2T:1P) was added to the solution and the solution was left to stir for 30 minutes. The solution was then stored at -5 ºC.

Functionalization of Metal Oxide or laponite NPs: 50 mg of ZnO or SN was added to a mixture of 1 ml ethanol and 1 ml deionized water. 200 µl of ammonium hydroxide (NH4OH) was then added to the mixture to increase the pH (above pH 9, ZnO or laponite SN should be negatively charged, measured by a pH paper) and activate the formation of the aryl radical. 124 µl of 4-Aminophenyldiazonium Tetrafluoroborate solution was diluted into 1.475 mL of deionized water to produce a 0.213 M solution. Next, 200 µl of 0.213 M solution was added to the reaction. After 1 hr of stirring, the solution underwent 5 cycles of centrifugation (1000-2000 rpm)/redispersion in water/ethanol solution (1:1 ration, 25 ml) for 8-10 times (25-28 min) to remove the excess aryldiazonium salt.

2.1.4. Synthesis and expression of elastin like polypeptide (ELP)

The photocrosslinkable ELP sequence was expressed as described in our previous study [121]. This ELP sequence consisted of 70 repeats of the pentapeptide VPGVG, in which the first valine was replaced with an isoleucine every five pentapeptides (i.e., $[[VPGVG]_4IPGVG]_{14}$). In addition, Lys-Cys-Thr-Ser (KCTS) residues were added to both sides of the ELP sequence to render it photocrosslinkable. *Escherichia coli* (*E. coli*) was used as a host to express the protein. The purification of the ELP was performed using inverse transition cycling [122]. The purified ELP solution was then dialyzed in a water bath, and stored at room temperature after lyophilization.

2.2. Fabrication of Adhesive hybrid hydrogels

2.2.1. Fabrication of MeHA/ELP hybrid hydrogels

To form MeHA/ELP hybrid hydrogels, different concentrations of MeHA (1 and 2% (w/v)) and ELP (0, 5, 10 and 15% (w/v)) were mixed in a 0.5% (w/v) solution of Irgacure 2959 in deionized water as a photoinitiator at 4 °C. The precursor solutions were then placed in either tensile (12 mm length, 6 mm width, 1.5 mm height) or compression molds (8 mm diameter, 2 mm height) made of polydimethylsiloxane (PDMS), and photocrosslinked using UV light (6.9 mW/cm^2, EXFO OmniCure S2000) for 120 sec. MeHA/ELP-ZnO hydrogels were prepared by directly adding different concentrations of 20 nm ZnO nanoparticles (0.1% and 0.2% (w/v)) (mkNANO) to the MeHA/ELP precursor solution containing 2% MeHA and 10% ELP. The mixture was gently mixed and photocrosslinked as described before.

2.2.2. Fabrication of visible light crosslinked GelMA-based hybrid hydrogels

Lyophilized GelMA biopolymers were dissolved in a solution containing TEA (1.8% w/v) and VC (1.25% w/v) in distilled water (at room temperature for fish GelMA and 37 °C for porcine GelMA). Eosin Y disodium salt (0.5 mM) was dissolved separately in distilled water. The biopolymers/TEA/VC solution was mixed with Eosin Y, and 70 mL of the final solution was placed into polydimethylsiloxane (PDMS) cylindrical (diameter: 6 mm; height: 2.5 mm) molds for compressive tests, or rectangular (14 × 5 × 1 mm) molds for tensile tests. The resulting solution was photocrosslinked via exposure to visible light (450-550 nm) for 240 s, using a LS1000 FocalSeal Xenon Light Source (Genzyme) for the eye adhesive. Prior to experimentation, hydrogels were incubated in DPBS for 30 min to remove any unreacted photoinitiators. GelMA-AMP hydrogels were formed by dispersing 2 mg of AMP Tet213 (CSCScientific, Inc.) with TEA (1.8% (w/v)) and VC (1.25% (w/v)) in 1 mL distilled water. The lyophilized biopolymers were dissolved in the AMP/TEA/VC solution, and the complete hydrogel precursor solutions were then

photocrosslinked as described previously.

2.3. Mechanical characterization of the engineered hydrogels

Hydrogels were prepared using compression or tensile molds as described before, and incubated for 2 h in DPBS. The dimensions of the hydrogels were then measured using a caliper. An Instron 5542 mechanical tester was used to perform tensile and cyclic compression tests. For the tensile test, hydrogels were placed between two pieces of double-sided tape within tension grips and extended at 1 mm/min until failure. Then, the tensile strain (mm) and load (N) were measured using the Bluehill 3 software. Elastic modulus of the engineered hydrogels was calculated from the slope of the stress-strain curves. For the unconfined compression tests, hydrogels were loaded between compression plates in a Dulbecco's phosphate-buffered saline (DPBS) water bath. Cyclic compression tests were performed at 70% strain level and a rate of 1 mm/min by performing 10 cycles of loading and unloading. Then, the compressive strain (mm) and load (N) were measured using the Bluehill 3 software. Then the modulus of elasticity (Young's modulus) was determined by obtaining the slope of the linear region (0.05-015 mm/mm strain) on the loading stress (kPa) versus strain (mm/mm) curve. Energy loss was calculated by obtaining the area between the loading and unloading curves for cycle 8 (n=4).

2.4. *In vitro* adhesion tests

In vitro burst pressure test: Burst pressure of engineered adhesive hydrogels, as well as Evicel® (Ethicon, Somerville, NJ, USA) and Coseal™ (Baxter, Deerfield, IL, USA) were obtained by using American Society for Testing and Materials (ASTM) standard (F2392-04) and as described previously [104]. Porcine intestine was placed between two stainless steel annuli, from a burst pressure apparatus in which the upper piece had a 10 mm diameter hole in its center. A 2 mm diameter defect was created by a 18 gauge syringe needle in the center of porcine intestine. 30 µl precursor solution was pipetted onto the defect on the intestine and photocrosslinked by

visible or UV light. The sealed intestine was then placed into the burst pressure testing apparatus, and the burst pressure was directly recorded by a connected to a wireless sensor (Pasco)/PC. For each experiment, at least 3 samples were tested.

In vitro lap shear test: Shear resistance of the adhesive hydrogels, as well as two commercially available adhesives, Evicel® and Coseal™ was determined based on a modified ASTM standard (F2255-05) for lap shear strength of tissue adhesive materials. As the substrate, two pieces of glass slides (10 mm × 50 mm) were coated with gelatin solution and was dried at room temperature. A 10 µl prepolymer solution was then photocrosslinked between two pieces of glass slides. The shear strength of the samples was then tested using an Instron mechanical tester (model) by tensile loading with a strain rate of 1 mm/min. The shear strength of the materials was calculated at the point of detaching. For each experiment, at least 3 samples were tested.

In vitro wound closure test: Wound closure of the adhesive hydrogels, Evicel® and Coseal™ was calculated by using the ASTM F2458-05 standard [58]. Porcine skin was obtained from a local butcher and cut into small strips (1 × 2 cm), with excess fat was removed. Tissues were immersed into PBS before testing to prevent drying in the air. The tissues were fixed onto two pre-cut poly(methyl methacrylate) slides (20 mm × 60 mm) by superglue. 6 mm spaces was kept between the slides using the porcine skin. The tissue was then separated in the middle with a straight edge razor to simulate the wound. 100 mL of polymer solution was administered onto the desired adhesive area and crosslinked by light. Maximum adhesive strength of each sample was obtained at the point of tearing at strain rate of 1 mm/min using a mechanical tester (n=5)

2.5. *In vitro* swellability of the adhesive hydrogels

Adhesive hydrogels were prepared and lyophilized as described before. Once the dried weights of the hydrogels were recorded, the samples were then immersed in DPBS for 24 h. The swollen gels were removed at different time points from the buffer solution and weighed. The

swelling ratio was calculated using Equation 1, where SR is swelling ratio, W_S is swollen weight of the hydrogel, and W_0 is the initial dried weight before swelling (n = 4):

$$SR = \frac{W_s - W_0}{W_0} \quad (1)$$

2.6. Pore size determination

The average pore size of the engineered hydrogels was evaluated using SEM analysis. Adhesive hydrogels containing different concentrations prepolymer solutions were prepared and lyophilized as described before. The samples were then mounted on aluminum stubs using conductive carbon paint and coated with gold/palladium prior to SEM analysis. A Hitachi S-4800 scanning electron microscope was used to obtain at least 10 SEM images from each sample. ImageJ software was then used to quantify the average pore size of the engineered hydrogels.

2.7. *In vitro* cell studies

2.7.1. Cell lines

NIH 3T3 cells (ATCC) were cultured at 37 °C and 5% CO_2 in Dulbecco's Modified Eagle Medium (DMEM) media (Gibco), containing 10% (v/v) fetal bovine serum (FBS) and 1% (v/v) penicillin/streptomycin (Gibco). hMSCs (Lonza) were cultured at 37 °C and 5% CO_2 in complete Mesenchymal Stem Cell Growth Medium (MSCGM™, Lonza). Cells were maintained in tissue culture treated polystyrene flasks and passaged 1:6 at 70% confluency. hMSC of passage 3-5 were used for all studies. Human corneal fibroblast cells were cultured at 37 °C and 5% CO2 in DMEM: Nutrient Mixture F-12 (DMEM/F12) (Sigma) containing 10% (v/v) FBS, 1% (v/v) Antibiotic/Antimycotics (Sigma) and 1% (v/v) L-glutamine (Sigma). Preosteoblast mouse stromal cells (W-20-17) at 37 °C and 5% CO_2 in Minimum Essential Medium (MEM) Alpha media (Gibco), containing 10% (v/v) fetal bovine serum (FBS) and 1% (v/v) penicillin/streptomycin (Gibco).

2.7.2. 2D cell seeding on adhesive hydrogels

Hydrogels were formed by pipetting 7 μL of precursor solution between a 3-(trimethoxysilyl) propyl methacrylate (TMSPMA, Sigma-Aldrich) coated glass slide and a glass coverslip separated with a 100 μm spacer. In the case of MeHA/ELP hydrogels,1% MeHA and 10% ELP concentrations were photocrosslinked upon UV light exposure (6.9 mW cm^{-2} UV light (365 nm)) for 30 sec. The hydrogels were then seeded with NIH 3T3 cells (5×10^6 cells/ml) and maintained at 37 ºC and 5% CO_2 for 5 days.

For GelMA hydrogels, W-20-17 cells with the density of 3×10^6 cells/ml was seeded on the surface of visible light crosslinked hydrogels (60 sec).

2.7.3. 3D cell encapsulation within the engineered hydrogels

For 3D cell encapsulation, a cell suspension of hMSC (5×10^6 cells/ml) was prepared by trypsinization and re-suspension into MSCGM™. The cell suspension was centrifuged to form a cell pellet and the media was discarded. The hydrogel precursor containing 2% MeHA and 10% ELP was prepared in cell culture media containing 0.5% (w/v) photoinitiator and mixed with the cell pellet. 7 μl of the resulting mixture were pipetted and hydrogels were formed by pipetting 7 μL of the precursor solution between a TMSPMA coated glass slide and a glass coverslip separated with a 100 μm spacer and photocrosslinked upon exposure to UV light for 30 sec. The resulting microgels (8 mm diameter, 100 μm thickness) were then immersed in culture medium for 2 h and then washed three times with culture medium to remove any unreacted materials. Lastly, the glass slides with the encapsulated hMSCs were placed in 24 well plates and incubated in MSCGM™ at 37 °C and 5% CO_2. Similar method was used to encapsulate W-20-17 cells within GelMA hydrogels.

2.7.4. Determination of cell proliferation

Cell proliferation was evaluated using a commercial PrestoBlue assay (Fisher) on days 0, 1, 3 and 5 according to instructions from the manufacturer. Briefly, 40 µl of PrestoBlue dye (10% of medium volume) was added to 360 µl of medium (total volume=400 µl). Cell seeded scaffolds were incubated in the PrestoBlue/medium solution for 1 h at 37 °C. The fluorescence intensity of the resulting solutions was recorded at 535-560 nm excitation and 590-615 nm emission wavelength at different culture times on days 1, 3, and 5. The relative fluorescence intensity of negative controls was recorded using a hydrogel without cells, culture medium, and PrestoBlue dye, and subtracted from all the samples to account for the background.

2.7.5. Determination of cell viability

A commercial calcein AM/ethidium homodimer-1 live/dead assay (Invitrogen) was used to evaluate cell viability according to instructions from the manufacturer. Cell viability was evaluated after 1 h (day 0), and then after 1, 3 and 5 days of culture. Briefly, culture medium was removed from the wells containing cell-seeded hydrogels and the samples were then incubated with 0.5 µl/ml of calcein AM and 2 µl/ml of ethidium homodimer in DPBS for 15 min in the dark at 37 °C. Live cells are stained green, whereas dead cells are stained red. The cell-seeded hydrogels were imaged with a ZEISS Axio Observer Z1 inverted microscope. Lastly, cell viability was calculated as the ratio of live cells to the total number of cells using ImageJ software.

2.7.6. Determination of cell adhesion and spreading

Cell spreading in 2D and 3D cultures was visualized by fluorescent staining of F-actin microfilaments and cell nuclei. Briefly, cell seeded hydrogels were fixed in 4% (v/v) paraformaldehyde (Sigma-Aldrich) for 20 min, and washed three times with DPBS at days 1, 3, and 5 post-seeding. Samples were then permeabilized in 0.1% (w/v) Triton X-100 (Sigma) in DPBS for 20 min. Next, samples were incubated with Alexa-fluor 488-labeled rhodamine-

phalloidin (2.5% (v/v) in 0.1% BSA, Invitrogen) for 45 min. Samples were washed three times with DPBS, and stained again with 1 µl/ml DAPI (4',6-diamidino-2-phenylindole, Sigma-Aldrich) in DPBS for 5 min. Lastly, the cell seeded hydrogels were washed three times with DPBS and fluorescent image acquisition was carried out using an Axio Observer Z1 inverted microscope.

2.7.7. Histological evaluation of the chondrogenic differentiation of 3D encapsulated hMSCs

hMSCs were 3D encapsulated in MeHA/ELP hydrogels as described before, and incubated at 37 ºC in MSCGM™ for 35 days. The cell laden hydrogels were harvested at different time points, on days 0, 7, 14, 21, and 35 post encapsulation, fixed in 4% paraformaldehyde for 4 h, and incubated in 30% sucrose overnight at 4 ºC. After fixation, the hydrogels were mounted in a Tissue-Plus optimal cutting temperature (OCT) compound (Fisher HealthCare), and flash frozen using dry ice. A minimum of ten 14-µm thick cryosections were obtained from each sample using a CM3050 S research cryostat (Leica). The cryosections were then stained in accordance with standard histological procedures using an Alcian blue solution (Millipore, 30 minutes), and counterstained using Hematoxylin (Sigma-Aldrich, 10 minutes). The stained samples were then mounted in DPX Mountant for histology (Sigma-Aldrich) and visualized using an Axio Observer Z1 inverted microscope.

2.8. Determination of *in vitro* antimicrobial activity of adhesive hydrogels

2.8.1. Bacteria seeding on adhesive hydrogels

MRSA (ATCC) was used to evaluate the *in vitro* antimicrobial properties of MeHA/ELP-ZnO hydrogels. MRSA stock cultures were hydrated and streaked for isolation on tryptic soy agar (Sigma). For all bacteria experiments, a single colony was used to inoculate 5 ml of tryptic soy broth (TSB; Sigma-Aldrich). The inoculated TSB was then placed on an incubator shaker set at 200 rpm for 18 hours at 37 °C. The optical density of the bacteria suspension was then adjusted to

0.52 at 562 nm, which corresponded to a cell density of 10^9 colony-forming units (CFU) per ml. Lastly, the resulting solution was serially diluted in TSB over a 3-log range to a density of 10^6 CFU/ml.

MeHA/ELP-ZnO hydrogels were placed in separate wells of a 48-well plate and sterilized under UV light. Each scaffold was then seeded with 1 ml of bacteria solution, and the plate was incubated at 37 °C and 5% CO_2 for 24 h. Following incubation, the scaffolds were transferred to a new well plate and washed 3 times with DPBS to remove any remaining bacteria from the hydrogels.

P. gingivalis (ATCC 33277) was grown in an anaerobic system at 37 °C for 7 days in Brain Heart Infusion (BHI) agar (Oxoid, Hampshire, UK).

2.8.2. Colony-forming units (CFU) assay

Adhesive hydrogels were seeded with MRSA and incubated as described before. After incubation, hydrogels were retrieved from the well plate and placed in 1.5 ml microcentrifuge tubes with 1 ml DPBS. The handling of the samples was minimized during transfer to avoid disruption of the bacterial biofilms on the hydrogels. The hydrogels were then vortexed at 3000 rpm for 15 min to strip all adherent bacteria from the hydrogels into DPBS. The resulting suspension was then serially diluted in DPBS over a 3-log range and three 20 µL drops of each dilution were plated on tryptic soy agar[123]. After 24 h of incubation at 37°C and 5% CO_2, the number of MRSA colonies that formed on each plate was counted and raw CFU totals were calculated based on the dilution factor.

For *P. Gingivalis*, similar procedure was followed, with some differences. The bacteria were seeded on Columbia Blood agar plates (BioMérieux, Marcy l'Etoile, France) after the 15 min vortexing step. Plates were incubated at 37 °C in anaerobic chamber for 96 hours.

2.8.3. BacLight™ live/dead assay

MeHA/ELP hydrogels were seeded with MRSA and incubated as described before. After incubation, the hydrogels were stained using BacLight™ Bacterial Viability kit (ThermoFisher) according to instructions from the manufacturer. Following staining, the samples were visualized using an Axio Observer Z1 inverted microscope.

2.8.4. SEM imaging of bacterial clusters on adhesive hydrogels

Adhesive hydrogels were seeded with MRSA or *P. Gingivalis* and incubated as described before. After incubation, the samples were fixed in a solution of 2.5% glutaraldehyde (Sigma-Aldrich) and 4% paraformaldehyde (Sigma-Aldrich) at 4 °C for 2 h and after dehydration in a series of ethanol/water solutions (30% to 100% v/v), lyophilized for 48 h. Lastly, the samples were mounted on SEM stubs, sputter coated with 6 nm of platinum, and visualized using a Hitachi S-4800 SEM.

2.9. Animal studies

2.9.1. Rabbit corneal surgeries

1. Slit Lamp Biomicroscopy: Slit lamp biomicroscopy was performed under general anesthesia using a Topcon system. Slit lamp photographs was also taken at the time of examination. With a 16x magnification, using slit and broad beams, transparency of the bioadhesive/defect area and surrounding cornea was evaluated (using the Fantes grading scale [124], which is based on visibility of iris details). To assess the migration of corneal epithelium over the adhesive/defect area, slit lamp photography with fluorescein staining was performed, and the area of the corneal epithelial defect was measured using Measure Area tool of the ImageJ [125] for each time point.

2. Anterior Segment Optical Coherence Tomography: AS-OCT was performed under

general anesthesia. AS-OCT is a non-contact imaging modality that provides high-resolution cross-sectional images. A spectral-domain AS-OCT (Spectralis, Heidelberg Engineering, Germany), with an axial resolution of 3.9-7µm, was used. Line scans (8 mm long) was performed at 0, 45, 90, and 135 degrees in the central cornea. To evaluate degradation of the bioadhesive and the stromal bed, their thickness (in microns) was measured in the center and at 0.75 and 1.5mm in both directions. To evaluate bioadhesive adhesion, the thickness of any gap between the bioadhesive and corneal tissue was measured in microns.

2.9.2. *Subcutaneous implantation of the adhesive hydrogels in rats*

Rat subcutaneous implantation protocol was approved by the Institutional Animal Care and Use Committee (Protocol No. 15-1248R) at Northeastern University. Male Wistar rats (200–250 g) were purchased from Charles River Laboratories (Wilmington, MA, USA) and kept in the animal core facility at Northeastern University (Boston, MA, USA). MeHA/ELP hydrogels (2% MeHA, 10% ELP) were prepared under sterile conditions in cylindrical (2 × 6 mm disks) molds. Anesthesia was induced by isoflurane (2-2.5%) inhalation, followed by SC buprenorphine (0.02 to 0.05 mg/kg). Six 8-mm incisions were created on the posterior dorsomedial skin of the animals, and lateral subcutaneous pockets were prepared by blunt dissection. Hydrogels were then implanted into the subcutaneous pockets, followed by suture and recovery from anesthesia. Implanted samples were retrieved with the adjacent tissues after euthanasia at days 3, 14, 28, and 56 days post implantation.

2.9.3. Mouse calvaria defect model

Experiments were performed according to the Guide for the Care and Use of Laboratory Animals (IACUC approval IS00000535) at Harvard School of Dental Medicine. A random distribution of male and female mice was utilized throughout the reported *in vivo* studies. After

general anesthesia, two 2 mm diameter defects were created in the both right and left sides of mouse skull (calvaria) using dental drills. 10 µl of the hydrogel prepolymers solutions were injected in the defect sites (7% and 15% (w/v)) and photopolymerized using a dental light curing unit (420-480 nm, 1500 mW) for 1 min. The animals recovered from anesthesia. The calvaria tissues were collected at different time points (1, 7 and 14 days) after implantation.

2.9.4. Ligature induced peri-implantitis model in minipigs calvaria defect model

- Tooth extraction: The animals were placed in lateral recumbency and the mouth was kept open with a mouth gag. The head was positioned using a moldable surgery cushion. Adhering to the surgical principle of adequate access, sulcular incisions were performed around the premolars. Additionally, a slight mesial vertical releasing incision was performed to allow a careful elevation of a full thickness flap. Standard dental instruments (forceps, elevators) were used to loosen and extract teeth. Crowns of the molars were vertically and horizontally separated (iChiropro). Root remnants were either removed with special root elevators or were drilled out with the same dental drill under adequate irrigation. Extraction sockets were cleaned. The lingual soft tissue was loosened from the bone plate and the mucoperiosteal flap was gently retracted with an elevator. Afterwards, the alveolar bone crest was down-leveled for 1 to 2 mm and sharp bony edges were smoothened. The buccal and lingual mucoperiosteal flaps were repositioned and closed using single sutures (Vicryl® 2/0). The animal was then turned to the other side and the surgical procedure was repeated in an identical manner on the other side of the mandible.

- For the bone graft study, 3 teeth past the mandibular canines bilaterally were extracted. Immediately following the extractions, the extraction sockets were assigned randomly to a treatment. The sockets were grafted with the antimicrobial and osteoconductive hydrogel and were

compared to commercial graft and the untreated samples. The CT scans were taken at the following time points after the extractions: 1-2 days, 1 month, 2 months.

- For the peri-implantitis study: implant placement, ligature placement, ligature replacement: Following eight weeks of healing the anesthetized mini pigs was placed analogous to the procedure of the first stage surgery. The alveolar ridge was accessed through a full-thickness flap using a slightly lingual, mid-crestal incision in combination with slightly curved vertical releasing-incisions at its mesial and distal end. The flap was then elevated and held back using special retraction hooks. Implant sites were prepared according to a standard and approved drilling protocol using rotating pilot and twist drills in ascending order (diameter). After careful removal of bone debris from the drill holes with sterile 0.9% physiological saline, implants were inserted automatically. After gingival former fixation (PF 4.0, height 3.2 mm), mucoperiosteal flaps were repositioned and closed tension-free with single sutures (Vicryl® 2/0). A single silk ligature (4.0) was placed around the abutment and slightly pushed downwards into the pocket and were sutured in the peri-implant mucosa, not only to facilitate plaque accumulation, but also to hold the ligatures in position. This finally will lead to a monolayer partly “submucosal” application. Ligatures were checked and maintained every week after placement. We check the ligatures every week to make sure they are in the place. We will replace them if they slip off. For ligature checking and replacement, pigs will need to be anesthetized. After 8 weeks, the ligatures were removed and replaced with new silk ligatures.

- Hydrogel treatment: Two weeks after replacement of silk ligatures (10 weeks after first ligature placement), the hydrogel treatments were started. In this step, the hydrogels were administered to the defect site using a pipette and were cured with a dental light curing system for 2 min to form

an adhesive gel around the dental implant (or in the bone defect site). To reduce the burden of the animals and follow the 3R principles, bleeding on probing (BOP) and pocket depth (PD) measurements were only performed at time of sacrifice. These measurements will help to characterize the progressive peri-implant bone loss by an increase in PD, and more profuse BOP ($p < 0.001$). In addition, PD measures of the extent and severity of periodontal pathology. The presence and degree of bleeding upon gentle periodontal probing (BOP) provided a measure of the presence of inflammation within the periodontal tissues. BOP was evaluated as present if bleeding was evident within 10 s after probing, or absent, if no bleeding was noticed within 10 s after probing. There is no concern related to blood clotting, since this test was performed right before euthanasia. PD was measured from the mucosal margin to the bottom of the probeable pocket. Each two measurements (mesial and distal) were performed at the lingual and buccal site. The statistical analysis was performed using a commercially available software program (SPSS® 18.0, SPSS Inc.). Mean values of all parameters were calculated.

2.9.5. Histological and immunohistofluorescent evaluation of in vivo biocompatibility

After explantation, adhesive hydrogels with the surrounding tissue were fixed, mounted, flash frozen, and cryosectioned as described before. Immunohistofluorescent staining was performed on cryosections according to a methodology previously described in the literature[121, 126]. Anti-CD3 [SP7] (ab16669) and anti-CD68 (ab125212) (Abcam) were used as primary antibodies. An Alexa Fluor® 594-conjugated antibody (Invitrogen) was also used as the secondary antibody. All samples were then stained again using DAPI. Lastly, the fluorescent images were taken using an Axio Observer Z1 inverted microscope.

2.10. Statistical analysis

At least 3 samples were tested for all experiments, and all data were expressed as mean ± standard deviation (*$p < 0.05$, **$p < 0.01$, ***$p < 0.001$ and ****$p < 0.0001$). T-test, one-way, or two-way

ANOVA followed by Tukey's test or Bonferroni test were performed where appropriate to measure statistical significance (GraphPad Prism 6.0, GraphPad Software).

3. RESULTS

3.1. Highly Elastic and Flexible Adhesive hydrogels for Surgical and Tissue Engineering Applications

3.1.1. Synthesis and structural characterization of photocrosslinkable adhesive hydrogels

The goal is to develop highly elastic, flexible and adhesive naturally derived biomaterials which are rapidly photocrosslinkable and promote long-term soft tissue regeneration such as cornea, lung, arteries and heart. To engineer the adhesive hydrogels, we utilized a visible light crosslinking system and different naturally derived biomaterials that their physiochemical properties can be finely tuned based on the application. In this section, we particularly focus on one possible application of these elastic bioadhesives which are developed for treatment and closure of corneal stromal defects and corneal lacerations [127].

Over 1.5 million new cases of corneal blindness are reported every year [128], of which only well under 5% are treated by corneal transplantations due to donor tissue shortage and the high expense of transplantation surgery [129]. Corneal injuries and infections are common causes of corneal scarring, stromal thinning, which can lead to tissue and vision loss [130]. In severe or progressive cases of corneal stromal inflammation, the stromal matrix may breakdown significantly to a point where the structure integrity of the eye is endangered. Current standards of care for treatment of corneal stromal defects include use of cyanoacrylate glue, tissue grafting, or corneal transplantation. However, these methods generally have significant drawbacks. For example, cyanoacrylate glue is associated with low biocompatibility, poor transparency, rough surface,

difficult handling, and poor integration with corneal tissues [131, 132]. Grafting requires donor tissues, advanced surgical skills, and specialized equipment. Tissue grafting can also be associated with transplant rejection and suture-related complications such as cheese-wiring through surrounding necrotic tissue, neovascularization, and microbial entrapment [129, 133]. Furthermore, using allogeneic tissue for grafting carries a high risk of immune reactions, specifically in those with acute injuries or infections [134]. Considering the magnitude of this problem, coupled with the shortage of donor corneas worldwide, cost-effective and cell-free biomaterial implants are highly desirable clinically [128].

Adhesive biomaterials have risen as a promising approach for the treatment of corneal stromal loss, particularly in emergency situations. Generally, biomaterials used for engineering corneal substitutes must employ physical, structural, and physiobiological characteristics similar to the native cornea. An ideal biomaterial for corneal repair and regeneration must possess (i) biocompatibility and biodegradability, (ii) mechanical stability and stiffness, (iii) high transparency, (iv) high adhesion to the native tissue, (v) capability of cell support and endogenous tissue regeneration, and (vi) clinical compliance, to minimize regulatory and scientific challenges, of specialized cleanrooms and immune rejections [135]. In addition, the engineered biomaterial must be easily applicable and rapidly crosslinkable *in situ.*

Biomaterials used as tissue adhesives for corneal sealing and repair can be categorized into two classes: (i) synthetic adhesives (e.g., cyanoacrylates and polyethylene glycol (PEG)-based adhesives) and (ii) naturally derived adhesives (e.g., fibrin, polysaccharide, collagen-based adhesives, etc.) [136]. Natural biopolymers tend to have excellent biocompatibility, but they often have low mechanical stability and adhesion. Synthetic biopolymers also enable customization of desired properties; however, they may not lead to tissue regeneration and biointegration [135].

Currently, no available adhesive has been designed for long-term integration with the cornea even though significant research has been devoted to developing adhesives that can close corneal incisions (as opposed to "filling in" defects). For example, ReSure® (Ocular Therapeutix, Inc., MA, USA), a PEG-based adhesive, is the only Food and Drug Administration (FDA)-approved ocular sealant in the US, which is designed to seal corneal incisions in cataract surgery [132]. However, ReSure® lacks the ability to fill stromal defects. It also possesses poor adhesion, especially in wet condition, and falls off quickly [136]. OcuSeal® (Beaver-Visitec International, MA, USA) is another PEG-based adhesive used in Europe for sealing corneal incisions, but it cannot be used for filling stromal defects, due to uncontrollable and rapid polymerization, which prevents sufficient time for thorough application [137]. Li *et al.* also formulated a dual-thiol and acrylate gelatin based hydrogel for ocular tissue regeneration; however, the use of UV-light crosslinking can cause corneal or retinal photochemical cytotoxicity or DNA damage [138, 139]. Other natural adhesives, including collagen vitrigel [140, 141], fibrin [142], gelatin (GelFilm® & GelFoam®) [143], alginate [144], and chitosan [145], have also been developed for ocular regeneration applications. However, there is no existing hydrogel adhesive which combine both regenerative and adhesive properties and can properly mimic natural healing of corneal tissue [132]. Additionally, many of these biomaterials lack high adhesion to corneal tissue and long retention, appropriate optical properties (e.g. coloration and curvature), transparency, and proper stiffness required to fully integrate with the biomechanical properties of the native cornea [136].

To address the unmet need of a biocompatible adhesive hydrogel for corneal tissue repair, we have engineered a gelatin-based adhesive biomaterial, GelCORE, which can be used for quick and long-term repair of corneal stromal defects. The proposed bioadhesive hydrogel is made of a chemically modified form of gelatin and photoinitiators, which can be photocrosslinked after short-time

exposure to visible light (450-550 nm). Upon completion of photocrosslinking, a solid and transparent hydrogel that firmly adheres to the corneal tissue is formed. The mechanical properties of the engineered hydrogel adhesive were optimized to mimic the stiffness of the native cornea. In addition, the adhesive formulation was modified to obtain high adhesion strengths to the cornea, while retaining appropriate biodegradability and high cytocompatibility *in vitro*. The adhesion characteristics of the bioadhesives were then tested based on standard adhesion tests provided by American Society for Testing and Materials (ASTM) and compared to commercially available adhesives. *Ex vivo* tests on explanted rabbit eyes were also performed to evaluate the retention and burst pressures. Finally, *in vivo* tests were conducted using a rabbit stromal cornea defect model to test the biocompatibility and retention of the biomaterial, as well as corneal regeneration after application.

3.1.2. Synthesis *and structural characterization of adhesive hydrogels*

We synthesized a transparent, flexible, and adhesive photocrosslinkable hydrogel for the treatment of corneal stromal defects. The engineered hydrogel, GelCORE, mimicked the mechanical properties of the native cornea and comprised with a chemically modified form of hydrolyzed collagen, which provides enzymatic degradation sites as well as physiological cell adhesion motifs [146]. UV crosslinkable gelatin-based sealants for sealing and repair of lung tissues [146] and sclera [138] have been reported. However, the use of UV light can induce DNA damage [147], and can cause corneal or retinal photochemical toxicity [148, 149], as well as carcinogenesis [150]. Specifically, UV-A (the longer wavelength) can cause retinal damage deeper within the eye (i.e., macular degeneration) and UV-B (the shorter wavelength) causing damage to the surface of the eye (i.e., photokeratitis or corneal sunburn) [151]. This limits the use of UV-mediated crosslinking techniques for corneal repair. To overcome the biosafety concerns associated with UV-initiated

crosslinking, we investigated a visible light crosslinking system to form GelCORE adhesives, where light intensity is well under the maximum permissible exposure (MPE) limit [152]. In our work, the adhesive hydrogels could be crosslinked through a free radical polymerization process, in the presence of a type 2 initiator Eosin Y, as well as triethanolamine (TEA) and N-vinylcaprolactam (VC) as co-initiator and co-monomer respectively (**Fig. 4a**).

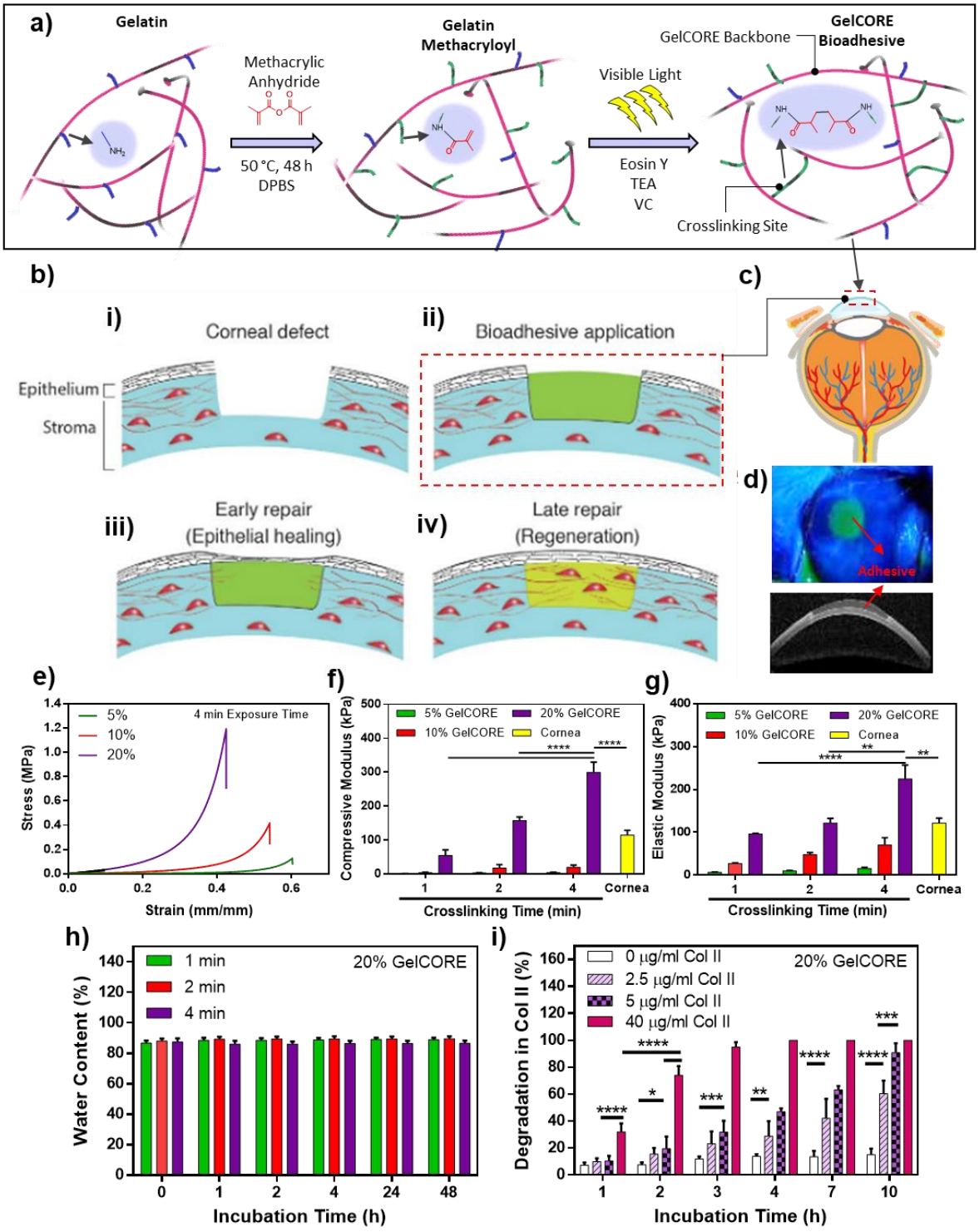

Figure 4. Synthesis, application, and *in vitro* characterization of GelCORE adhesive hydrogels. (a) Schematic of the chemical reaction for GelCORE formation and photocrosslinking of the prepolymer solution with Eosin Y (photoinitiator), TEA (co-initiator) and VC (co-monomer). **(b)** Schematic diagram for the application of GelCORE for rapid and

long-term repair of corneal injuries which include **(i)** formation of stromal defect, **(ii)** application of the bioadhesive, **(iii)** regeneration of the epithelial layer and **(iv)** stromal regeneration. **(c)** The prepolymer solution is injected into the corneal defect and exposed to visible light, forming **(d)** an adhesive GelCORE hydrogel. **(e)** Representative compressive stress-strain curves, **(f)** compressive (Young's) moduli, and **(g)** elastic moduli of GelCORE adhesive hydrogels fabricated using 5%, 10%, and 20% (w/v) total polymer concentration with varying photocrosslinking time points. **(h)** Water content of GelCORE adhesives produced by using 20% (w/v) polymer concentration and varying visible light exposure times at 37 ºC in DPBS over time. **(i)** *In vitro* degradation of 20% (w/v) GelCORE adhesive (4 min photocrosslinking time), in different concentrations of collagenase type II solution in DPBS and 37 ºC over time. All hydrogels were polymerized by using 0.1 Mm Eosin Y, 1.5% (w/v) TEA and 1% (w/v) VC in distilled water. Data are reported as mean ± SD (*$p<0.05$, **$p<0.01$, ***$p<0.001$, ****$p<0.0001$ and $n \geq 3$).

The visible light crosslinking scheme has been proven to improve cell viability, compared to UV crosslinked systems [153-155]. Briefly, the visible light photons excite the photoinitiator molecules (Eosin Y) to a triplet state, which allow them to accept hydrogen atoms from co-initiator molecules (TEA). The deprotonated radicals then undergo vinyl-bond crosslinking with comonomer (VC) via chain polymerization. This will result in accelerated gelation of the polymeric scaffolds [156]. This visible light photocrosslinking chemistry is an FDA-approved system [157] and has been used previously as a safe photocrosslinking system for biomedical applications [104, 156, 158]. A schematic of the polymer network photocrosslinking process with representative images of the crosslinked adhesive on a corneal defect are shown in **Fig. 4b**. The hydrogel prepolymer solution could be easily and rapidly applied to a corneal stromal defect and photopolymerized allowing the defects with varied shapes and sizes to be quickly sealed, and thus promoting regeneration of new stromal tissue (**Fig. 4b-d**). Accordingly, after creation of corneal stromal defect (**Fig. 4bi**), the GelCORE prepolymer is applied to fill the defect site (**Fig. 4bii**).

Next, in the early stages of healing process, the corneal epithelial layer begins to regenerate (**Fig. 4biii**), and the full stromal regeneration occurs at late repair process (**Fig. 4biv**).

In order to determine the crosslinking density of the hydrogel network, 500 MHz Proton nuclear magnetic resonance (^{1}H NMR) analysis was performed on GelCORE prepolymers and GelCORE hydrogels photocrosslinked at 1, 2, and 4 min visible light exposure times using techniques previously defined [104] (**data is not shown**). Results showed that methacryloyl (methacrylate/methacrylamide, -C=CH_2) functional groups in the GelCORE backbone with characteristic peak 1 at δ=5.3 ppm and peak 2 at δ=5.7 ppm were incorporated in the formation of the crosslinked 3D bioadhesive network. Accordingly, the degree of crosslinking could be calculated by measuring the alteration in integrated areas of the methacryloyl peaks before and after the photocrosslinking process [104]. Based on our results, it was found that the degree of crosslinking increased from 63.4 ± 2.7 % to 88.9 ± 7.9 % when visible light exposure time was increased from 1 to 4 min for 20% GelCORE concentration (**data is not shown**). Comparatively, we previously reported the formation of a UV-crosslinkable gelatin-based hydrogel as a lung sealant, which demonstrated >95% crosslinking density after 3 min UV exposure time [146].

Physical properties (i.e., mechanical properties, *in vitro* swelling ratio, and degradability) of GelCORE adhesive hydrogels were characterized. Mechanical properties of the bioadhesives were determined through compression and tensile tests **(Fig. 4e-g).** Our results revealed that by varying the concentration of GelCORE and the photocrosslinking time, the critical mechanical properties of the hydrogel could be finely controlled to derive formulations with tensile and compressive (Young's) moduli that are comparable to the native cornea **(Fig. 4e-g)**. For instance, the Young's modulus of adhesive hydrogels engineered with 5% (w/v) GelCORE increased from 1.2 ± 0.5 kPa

to 4.5 ± 1.2 kPa as the light exposure time increased from 1 to 4 min, respectively **(Fig. 4f)**. In addition, increasing the prepolymer concentration remarkably enhanced the mechanical properties of the bioadhesives. For instance, the Young's modulus of hydrogels formed by using 4 min light exposure time was increased 66.4-fold from 4.5 ± 1.2 kPa for 5% polymer concentration to 299.9 ± 30.0 kPa for 20% polymer concentration **(Fig. 4f)**. This significantly highlights the wide range of controllable moduli which can be obtained just by changing either polymer concentration or photocrosslinking time. Comparatively, the Young's moduli of the adhesive hydrogels were well encompassing of the range of moduli of native cornea (115.3 ± 13.6 kPa) which is crucial for long term tissue/biomaterial integration and remodeling **(Fig. 4f).** Rizwan *et al*. formed UV crosslinked gelatin-based hybrid patches for corneal tissue regeneration with similar compressive moduli (ranged from 28.8 kPa to 233.3 kPa) when the total polymer concentration changed from 10 to 30% (w/v) [159]. However, the application of this prefabricated graft required advanced surgical skills and equipment [159].

Similarly, tensile tests on GelCORE bioadhesives revealed tunable elastic moduli (**Fig. 4g**) and ultimate tensile strength (UTS) (**data is not shown**) by varying the GelCORE concentration and visible light exposure time. For example, the Young's moduli of adhesive hydrogels engineered with 5% (w/v) GelCORE enhanced from 6.7 ± 0.8 kPa to 16.0 ± 2.1 kPa by increasing the photocrosslinking time from at 1 to 4 min **(Fig. 4g)**. In addition, the Young's moduli of the adhesive hydrogels photocrosslinked at 4 min increased 14-fold from 16.0 ± 2.1 kPa to 224.4 ± 32.3 kPa by increasing the total polymer concentration from 5 to 20% (w/v) **(Fig. 4g)**. Furthermore, the UTS of engineered bioadhesives was consistently increased from 38.0 ± 6.1 kPa to 45.3 ± 4.1 kPa for 20% (w/v) GelCORE, when the photocrosslinking time increased from 1 to 4 min **(data is**

not shown). Similar to compressive tests, these results demonstrated that the elastic moduli of the GelCORE bioadhesives was in the range of native corneal tissue (121.8 ± 11.6 kPa) (**Fig. 4g**). This enhancement in stiffness of the hydrogels at higher polymer concentrations or light exposure time can be due to the higher crosslinking density within the hydrogel network as confirmed by ^{1}H NMR analysis.

In addition to mechanical properties, water content and enzymatic degradation of the engineered adhesive hydrogels were also characterized. The degree of hydration (water content) of the GelCORE adhesives was measured in DPBS (37 °C, 48 h). After 48 h of incubation, no significant differences were observed in the water content of the GelCORE samples synthesized at 1, 2, and 4 min photocrosslinking time. In addition, the degree of hydration did not alter by time, when incubated for 48 h in DPBS (37 °C). Furthermore, the water content of the samples was in the range of 85.9% to 89.5% (**Fig. 4h**) which found to be comparable to the degree of hydration of the native human cornea (85-86%) [160].

The enzymatic degradation of photocrosslinked GelCORE hydrogels were characterized using different concentrations (0, 2.5, 5, and 40 µg/ml) of collagenase type II solution in Dulbecco's Phosphate-Buffered Saline (DPBS) for up to 10 days (**Fig. 4i**). Results showed that the enzyme concentration could directly affect *in vitro* degradation rate of the hydrogels. For example, the adhesives showed 100% degradation after 4 days incubation in 40 µg/ml enzyme concentration. However, 13.8 ± 1.6 %, 28.9 ± 11.1 %, and 46.9 ± 2.4 % degradation was obtained after 4 days, when the samples were incubated in 0, 2.5, and 5 µg/ml enzyme concentrations, respectively (**Fig. 4i**). Moreover, the degradation rate of 20% (w/v) GelCORE bioadhesives increased from 15.1 ±

4.3% to 90.7 ± 7.0% by increasing enzyme concentration from 0 to 5 µg/ml after 10 days of incubation (**Fig. 4i**). The ability to control and tune the degradation rates of the adhesive hydrogels is remarkably advantageous for the implementation of GelCORE as an adhesive for ocular applications. This can promote simultaneous bioadhesive enzymatic degradation and tissue integration, which can result in the new corneal stromal tissue ingrowth.

Overall, the physical characterization of GelCORE adhesive hydrogels demonstrated that the mechanical properties, and *in vitro* enzymatic degradation can be tuned by changing total polymer concentration and photocrosslinking time. This significant degree of tunability suggests that GelCORE bioadhesive could be readily adjusted for various surgical and tissue engineering applications, especially regeneration of corneal stroma defects.

3.1.3. *In vitro* adhesive properties of GelMA adhesive hydrogels

Generally, high adhesion of hydrogels to the adjacent tissue can avoid biomaterial detachment from target tissues *in vivo* and eventually promote potential biointegration. An ideal tissue and biomaterial integration, improves biocompatibility and enhances tissue regeneration under physiological conditions [111]. Herein, we examined critical properties for effective bioadhesion, including shear strength, adhesion strength, and burst pressure, according to ASTM standards for biological adhesives. In these standards, the *in vitro* adhesion strength and sealing properties of GelCORE adhesive hydrogels, produced at various prepolymer concentrations and visible light exposure time, were compared to commercial surgical sealants, Evicel® and CoSEAL™ (**Fig. 8)**.

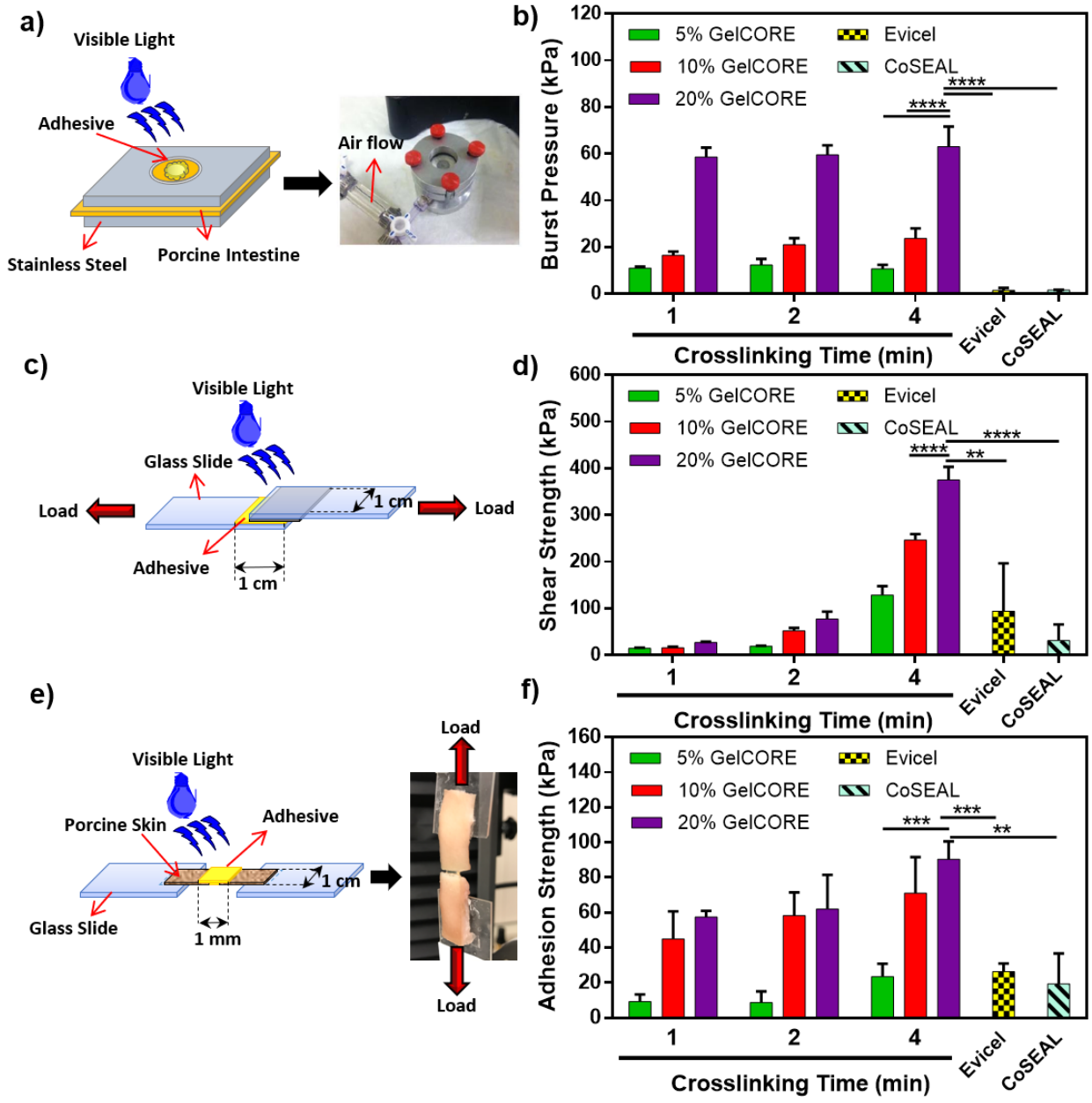

Figure 5. ***In vitro*** **adhesion properties of GelCORE hydrogels using porcine skin and intestine as biological substrates. (a)** Schematic of the modified test for burst pressure measurements (ASTM F2392-04) and **(b)** average burst pressure of GelCORE adhesives ($n \geq 3$) produced with varying polymer concentrations, photocrosslinking times, compared to two commercial adhesives including Evicel® and CoSEAL™. **(c)** Schematic of the modified test for lap shear strength measurements (ASTM F2255-05) and **(d)** average shear strengths of GelCORE adhesives ($n \geq 3$) produced with varying polymer concentrations and photocrosslinking times, Evicel®, and

CoSEAL™. **(e)** Schematic of the modified test for wound closure test (ASTM F2458-05) and **(f)** average adhesive strengths of GelCORE adhesives ($n \geq 3$) produced with varying polymer concentrations and photocrosslinking times, compared to Evicel® and CoSEAL™. Data are means ± SD (*$p < 0.05$, **$p < 0.01$, ***$p < 0.001$, ****$p < 0.0001$).

To investigate burst pressures of the engineered adhesives, air pressure was continuously pumped into a custom designed burst pressure apparatus. The adhesive polymers were applied to seal a standardized defect in a porcine intestine sheet as a biological substrate, based on a modified ASTM standard test, F2392-04 (**Fig. 8a).** Our results showed that the burst pressures of GelCORE adhesives significantly increased from 10.8 ± 1.6 kPa to 63.1 ± 8.5 kPa as the GelCORE concentration was increased from 5% (w/v) to 20% (w/v) at 4 min photocrosslinking time (**Fig. 8b)**. Comparatively, Gratieri *et al.* reported burst pressures of approximately 12 kPa for a chitosan-based adhesive for ocular regeneration [145]. This value is significantly lower than GelCORE-based adhesives presented here. Furthermore, cyanoacrylate glues for corneal repair showed burst pressure of approximately 68 kPa, which is comparable to our engineered adhesives [161]. However, cyanoacrylate glues are generally toxic, and show low biocompatibility and poor transparency [131, 132]. Moreover, a UV-crosslinkable gelatin-based adhesive used for ocular application achieved maximum burst pressure around 12 kPa as well [161, 162], which is below the value obtained for GelCORE adhesives (~58 - 63 kPa for 20% (w/v) polymer concentration at 1 to 4 min light exposure time respectively). Furthermore, burst pressures of GelCORE adhesive hydrogels in all tested concentrations (5, 10, and 20% (w/v)) were significantly higher than both clinically available sealants, with a burst pressure range of 11.1 ± 0.6 kPa to 63.1 ± 8.5 kPa as compared to 1.5 ± 0.7 kPa for Evicel® and 1.6 ± 0.2 kPa for CoSEAL™ (**Fig. 8b)**. GelCORE adhesive hydrogels additionally showed higher burst pressures than values of 0.3 ± 0.3 kPa for

CoSEAL™ as reported by Campbell *et al* [163]. Furthermore, our GelCORE adhesive achieved higher burst pressures than DuraSeal (0.8 kPa) and Fibrin Sealant (0.2 kPa) [163]. Additionally, it was reported that majority modes of failure for these commercial products were related to the cohesive properties of the materials [163]. This indicates that these bioadhesives were simply inherently weak. It should be noted that burst pressure values for 20% GelCORE sealant were not significantly improved when increasing the photocrosslinking time from 1 to 4 min (**Fig. 8b)**.

Next, the shear strengths of the engineered bioadhesives were investigated using a modified test based on ASTM standard F2255-05 (**Fig. 8c**). Similar to the burst pressure results, a wide range of shear stresses were obtained, indicating fine controllability and repeatability of shearing properties. The highest shear strength was observed for 20% (w/v) GelCORE bioadhesive (375.2 ± 28.0 kPa) at 4 min photocrosslinking. This value was significantly higher than lap shear strength of Evicel® (207.7 ± 67.3 kPa) and CoSEAL™ (69.7 ± 20.6 kPa) (**Fig. 8d**). Moreover, increasing the photocrosslinking time from 1 to 4 min improved the shear strength of GelCORE adhesives for all tested concentrations. For example, the shear strength of 10% (w/v) GelCORE adhesive increased from 15.6 ± 2.9 kPa to 246.5 ± 12.6 kPa by increasing photocrosslinking time from 1 to 4 min as shown in **Fig. 8d**.

Finally, the adhesion strengths of the engineered adhesives were investigated using a modified test based on ASTM standard F2458-05 (**Fig. 8e**). Similarly, higher adhesive strength was observed at higher concentrations of GelCORE. For example, 20% GelCORE hydrogels, crosslinked via 4 min visible light exposure, reached adhesive strength of 90.4 ± 10.2 kPa. This value was remarkably higher than that of CoSEAL™ (19.4 ± 17.3 kPa) and Evicel® (26.3 ± 4.7 kPa) (**Fig. 8f)**. This was

also higher than adhesive strengths obtained by other commercially available bioadhesives or sealants such as Quixil (24.6 kPa), Beriplast (24.2 kPa), Tachosil (59.6 kPa), and Tisseel (77.5 kPa) [164]. In addition, it was found that adhesive strengths of the engineered GelCORE adhesives were also affected by the light exposure time. For example, adhesion strengths increased from 57.5 ± 3.5 kPa to 90.4 ± 10.2 kPa as exposure time was increased from 1 to 4 min for a 20% GelCORE hydrogel (**Fig. 8f**).

Overall, the measurement of mechanical and adhesive properties of GelCORE adhesives showed excellent cohesion and adhesion for 20% GelCORE concentration. The wound closure strengths, shear resistances, and burst pressures for a 20% (w/v) GelCORE bioadhesive were significantly higher than clinically available PEG-based (Evicel®) and fibrin-based (CoSEAL™) controls.

3.1.4. *Ex vivo retention and burst pressure resistant of the engineered bioadhesive*

Dimensional stability and retention time for the engineered bioadhesives were investigated on corneal tissues *ex vivo* by using slit lamp biomicroscopy and Anterior Segment Optical Coherence Tomography (AS-OCT) (**Fig. 9**). Upon creation of a corneal defect in explanted New Zealand rabbit eyes (3-mm in diameter and >50%-deep), the adhesive precursor solutions (10 and 20 %(w/v)) were applied to the defect site and exposed to visible light for 1, 2, and 4 min forming a transparent hydrogel with a smooth surface and complete corneal curvature (**Fig. 9a**). The GelCORE hydrogel could strongly adhere to the explanted tissue (**Video S1)**. After application of the bioadhesives, eyes sealed with hydrogels were stored in DPBS at 4 ºC and changes in bioadhesive structure and retention were assessed over time using serial evaluations with slit lamp biomicroscopy and AS-OCT (**Fig. 9a,c**). Upon observation, all examined hydrogels showed firm adhesion to the corneal stroma.

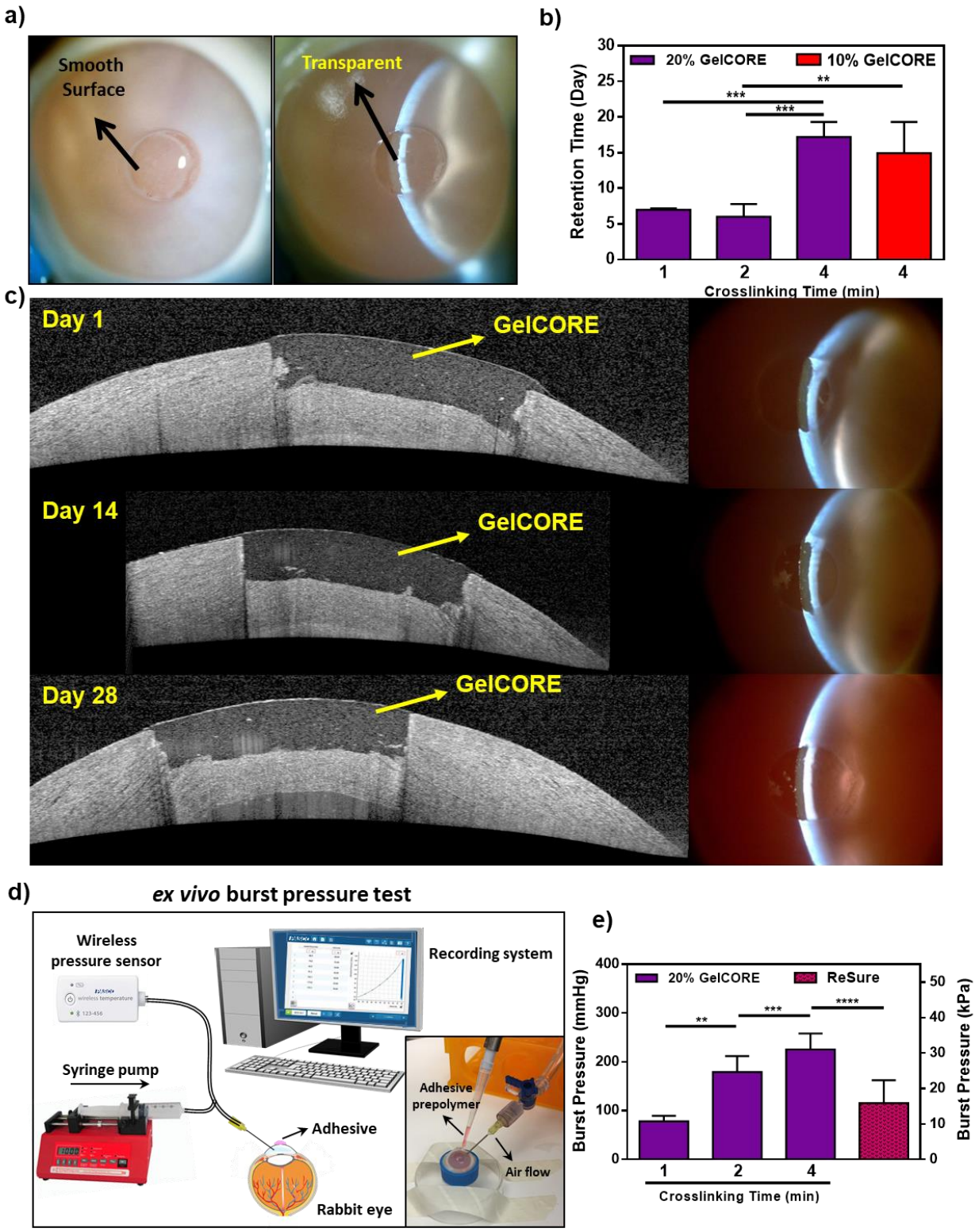

Figure 6. *Ex vivo* application and adhesion properties of GelCORE adhesives. (a) Representative slit lamp photographs from rabbit eyes sealed by GelCORE bioadhesive, and

(b) retention times of GelCORE bioadhesives, formed at various crosslinking times and prepolymer concentrations, on cornea tissues. **(c)** OCT images after *ex vivo* application of GelCORE adhesives to rabbit corneas at days 1, 14 and 28 after application. **(d)** Schematic of *ex vivo* burst pressure set up, including a syringe pump, a pressure sensor and a recording system. **(e)** Average burst pressure of GelCORE adhesives formed by varying photocrosslinking time, compared to a commercially available ocular sealant, ReSure® (control). Data are represented as mean ± SD (*p<0.05, **p<0.01, ***p<0.001, ****p<0.0001, $n \geq 4$).

In addition, results revealed that retention times for 10 and 20% (w/v) GelCORE at 4 min photocrosslinking times were 15 and 17 days, respectively. This was 2.1 and 2.5 times higher than the retention times for 20% GelCORE formed at 1 min exposure time, respectively (**Fig. 9b**). This observation can be correlated to higher adhesion strengths of 10 and 20% (w/v) GelCORE adhesives at 4 min exposure time based on the wound closure test (**Fig. 8f**). It was also noted that for the duration of a 20-day assessment period, the bioadhesives remained uncompromised (thickness and spread were fully retained) and the adhesives were completely attached to the cornea in all tested eyes (**Fig. 9c**). Slit lamp biomicroscopy also corroborated that during this time period, the bioadhesive remained transparent with a smooth surface without any microscopic signs of changes in shape or contour. AS-OCT also confirmed no change in thickness or shape of the bioadhesive after 28 days (**Fig. 9c**).

An *ex vivo* burst pressure test was also performed to measure the burst pressures of bioadhesives on rabbit eyes (**Fig. 9d**). Accordingly, a 2-mm full-thickness incision was created in the cornea, followed by sealing with either GelCORE bioadhesives or ReSure® (as control). For this test, GelCORE adhesive precursors as well as ReSure® were applied to the corneal incision sites in

explanted rabbit eyes and crosslinked *in situ*. The sealed eye was then connected to a burst pressure apparatus, containing a syringe pump and a pressure sensor. Air was injected continuously, increasing pressure until bursting of the sealant (**Fig. 9d**). Burst pressures of explanted eyes sealed with 20% GelCORE adhesives engineered at varying visible light exposure times (1, 2, and 4 min) were measured using a digital wireless sensor (**Fig. 9e**). Burst pressures of the GelCORE adhesives formed at 4 min photocrosslinking were found to be 30.1 ± 4.3 kPa. This was approximately 10 times higher than that of normal eye pressure, and significantly higher than burst pressure of the commercial control, ReSure® (15.4 ± 6.3 kPa) (**Fig. 9e**). Finally, by increasing the photocrosslinking time from 1 to 4 min, burst pressures of 20% (w/v) bioadhesives increased from 10.4 ± 1.5 to 30.1 ± 4.3 kPa (**Fig. 9e**).

Inclusively, the adhesive hydrogels engineered by using 20% GelCORE and photocrosslinked by using 4 min exposure time showed the highest *ex vivo* burst pressure resistance and retention time. Therefore, this hydrogel formulation was selected for *in vitro* cell studies and *in vivo* assessment of retention and cornea tissue regeneration.

3.1.5. *In vitro assessment of cytocompatibility and integration of adhesive hydrogels.*

The optimal bioadhesive for corneal repair should be biocompatible with no cytotoxicity. It should also permit cells of the injured tissue to migrate into the bioadhesive for long-term integration and repair. Therefore, we aimed to evaluate the *in vitro* cytocompatibility and cell migration for the engineered adhesives using 2D cell seeding and scratch tests (**Fig. 10**).

To accomplish this, cytocompatibility of engineered hydrogels was assessed *in vitro*. The viability, adhesion, proliferation, and metabolic activity of human cornea fibroblast cells (keratocytes)

seeded on GelCORE adhesives were evaluated by using a commercial kit for live/dead assay, and PrestoBlue tests. In addition, the results were compared to viability and methanolic activity of the cells seeded on tissue culture well-plates and ReSure sealant as controls. The results showed that the cells seeded on both tissue culture well-plate control and bioadhesives (20% GelCORE) exhibited high viability (> 90%) after 1, 4, and 7 days post seeding (**Fig. 10a-b, 10d**). In contrast, the cell viability for ReSure sealant was significantly lower than GelCORE adhesive (<65%) during the same time period (**Fig. 10c,d**). The quantification of cell metabolic activity also confirmed this observation, where the metabolic activity of keratocytes seeded on ReSure was 1.2 and 2.8-fold lower than the cells seeded on GeCORE adhesive on days 1 and 7 post seeding (**Fig. 10e**). In addition, metabolic activity of keratocytes seeded on GelCORE adhesive increased consistently from 4008 ± 1795 RFUs at day 1 to 31139 ± 697 RFUs at day 7 post seeding, respectively (**Fig. 10e**). Furthermore, Actin/DAPI staining exhibited an increase in cell spreading on GelCORE bioadhesive over time (**data is not shown**).

The *in vitro* scratch assay also revealed that keratocytes seeded on the surface of adhesive hydrogels could migrate to the scratched area (400-500 µm distance) in less than 24 h (**Fig. 10f-g**). In addition, to quantify the migration to the wound area, we compared cell density in the scratched area to the surrounding cell density. The results showed that the relative cell density for GelCORE adhesive hydrogels was significantly higher than that of the control (tissue culture plate) 1, 2, and 3 days after creating the scratch (**Fig. 10h**). For example, the relative cell density for GelCORE hydrogel was 94.4 ± 3.4 % which was 36% higher than the control. This indicates that cell migration and proliferation on the surface of GelCORE adhesives were higher than that of the control (**Fig. 10h**).

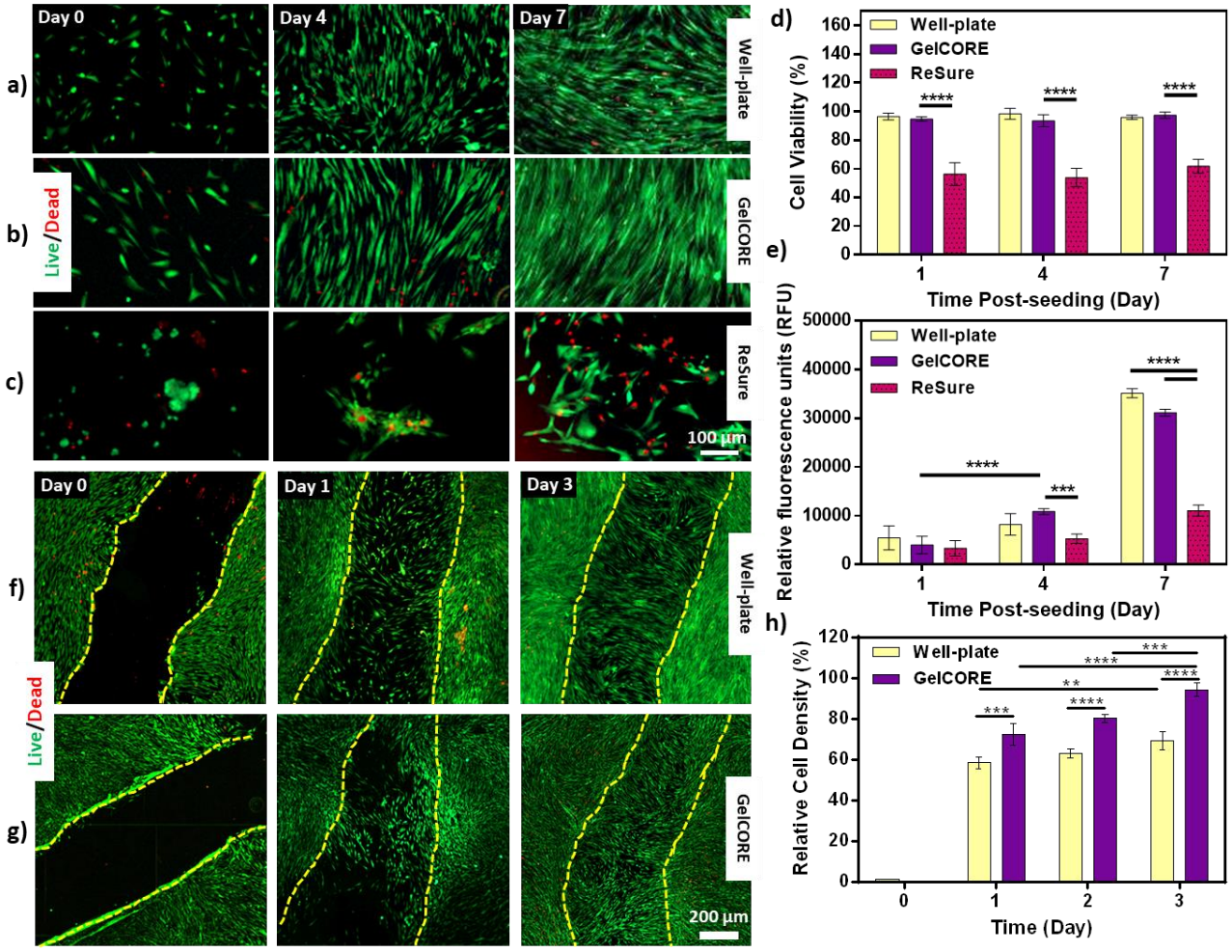

Figure 7. ***In vitro*** **cytocompatibility of GelCORE bioadhesives.** Representative live/dead images from corneal fibroblast cells seeded on **(a)** tissue culture well-plate, **(b)** GelCORE adhesives, and **(c)** ReSure sealant on day 1, 4 and 7 post seeding (scale bar = 100 µm). **(d)** Quantification of cell viability on GelCORE bioadhesives compared to tissue culture well-plate and ReSure after 1, 4, and 7 days of culture. **(e)** Quantification of metabolic activity of corneal fibroblast cells seeded on control (tissue culture well-plate), GelCORE hydrogels, and ReSure after 1, 4, and 7 days. Representative live/dead images of corneal fibroblast cells grown on **(f)** tissue culture well-plate and **(g)** GelCORE hydrogels on a 2D scratch assay at days 0, 1 and 3 after scratching. **(h)** Quantification of relative cell densities migrated to the scratched area on GelCORE adhesives and control samples, at days 0, 1, 2, and 3. GelCORE hydrogels at 20% (w/v) final polymer concentration were used for 2D cell culture studies (photocrosslinking time: 4 min). Data is represented as mean ± SD (**p < 0.01, ***p < 0.001 and ****p < 0.0001, n ≥ 3).

Many researchers investigated cytotoxicity and biocompatibility of synthetic bioadhesives and sealants *in vitro* and *in vivo,* and the cytotoxic nature of some of the synthetic bioadhesives has been widely reported [82, 136, 165, 166]. For example, Chen *et al.* reported high level of corneal cytotoxicity for methoxypropyl cyanoacrylate and N-butyl cyanoacrylate, while fibrin glue, showed minimal cytotoxicity in their studies [165]. However, cyanoacrylate-based adhesives showed a higher capability to seal corneal incisions compared with fibrin glue. In another study, Fürst *et al.* showed high *in vitro* and *in vivo* toxicity of BioGlue, which is a sealant based on bovine serum albumin and glutaraldehyde crosslinker [82]. Their results revealed that crosslinked BioGlue released significant amounts of glutaraldehyde that can cause cytotoxic and histotoxic effects on lung, arteries, and liver [82]. In addition, it has been reported that BioGlue may cause serious nerve injury, mineralization, and coagulation necrosis [136] which dramatically reduces its possible application in ophthalmic surgeries [136]. In contrast, our results indicated that GelCORE adhesive hydrogels prepared with visible light-initiated system are nontoxic to keratocytes. In addition, the adhesive hydrogel can support proliferation, adhesion and spreading, and metabolic activity of corneal cells *in vitro*. Therefore, GelCORE adhesive hydrogels maybe able to effectively enhance the healing process of corneal defects.

3.1.6. In vivo assessment of GelCORE bioadhesives in a rabbit stromal defect model.

In our previous studies, we confirmed *in vivo* biocompatibility of UV and visible light crosslinked gelatin-based bioadhesives. This was done via subcutaneous implantation of disk-shaped hydrogels in rats [104] and *in situ* polymerization of gelatin-based sealants on incisions created on porcine lungs [146]. In addition, we also confirmed *in vivo* biocompatibility of photocrosslinked gelatin hydrogel through direct injection into the myocardium and *in situ* polymerization [117].

Our results showed that the hydrogels could degrade after two weeks without inducing significant inflammatory response while promoting tissue formation.

Herein, for the first time, we assessed the use of our engineered bioadhesives specifically designed for corneal sealing in a corneal injury model in New Zealand white rabbits. This was done by creating 50%-deep corneal defects in rabbit cornea (**Fig. 8a-b**) in order to evaluate, the biocompatibility and biointegration of the engineered GelCORE hydrogels for repair and sealing of corneal defects. After creating a half-thickness corneal stromal defect, a 20% (w/v) GelCORE bioadhesive precursor was applied into the defect site (**Fig. 8c**) followed by *in situ* polymerization via visible light for 4 min (**Fig. 8d**) ($n \geq 4$). Immediately after photocrosslinking, there was a firm adhesion of the bioadhesive to the corneal defect.

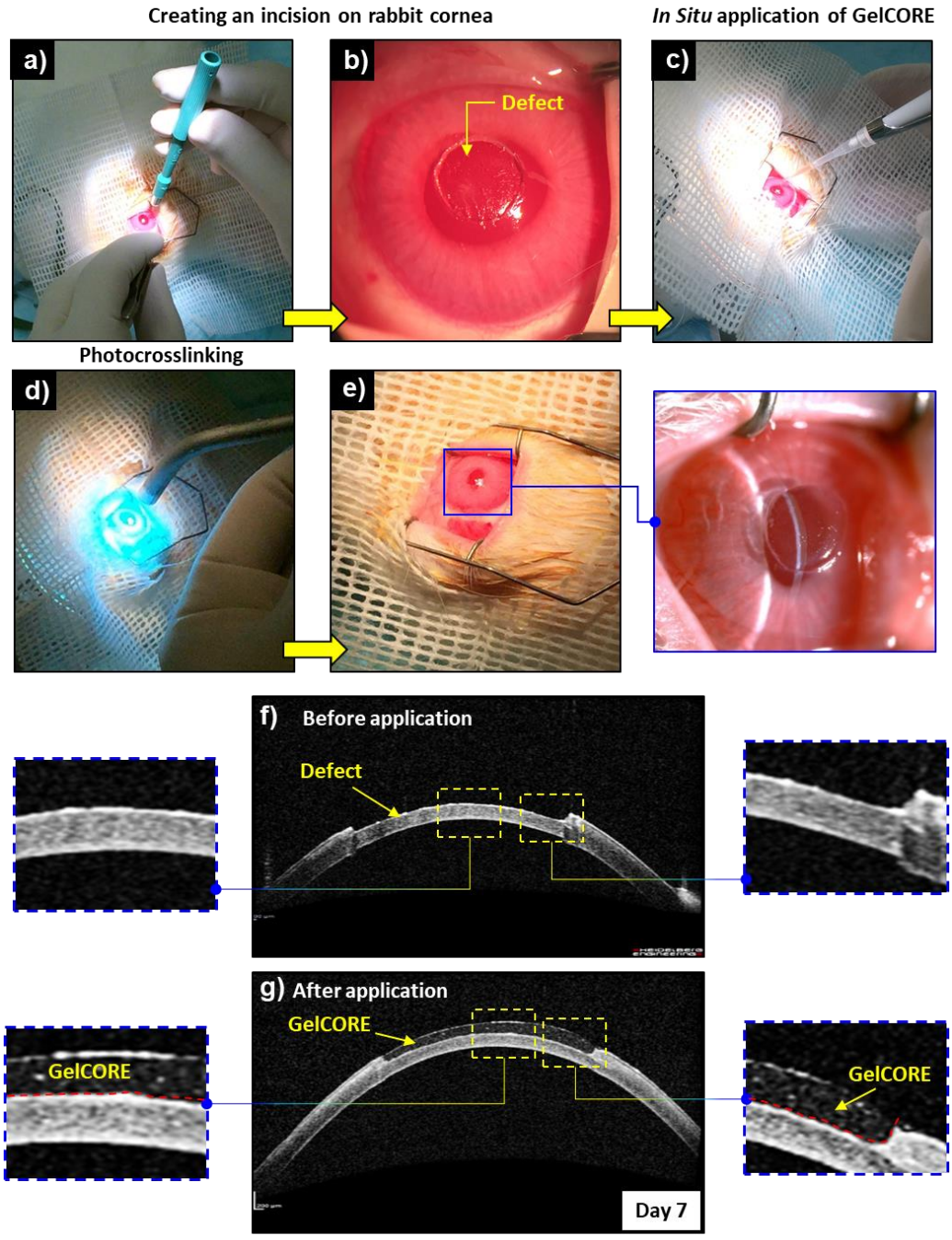

Figure 8. ***In vivo*** **application of GelCORE bioadhesives into corneal defects in rabbits**. **(a-b)** Representative images for creating a 50%-depth corneal stromal defect on rabbit eye. **(c)** *In situ* application of GelCORE prepolymer solution into corneal defect. **(d)** Photocrosslinking and **(e)** formation of a transparent GelCORE adhesive hydrogel on corneal stromal defect. AS-OCT images **(f)** before and **(g)** after treatment with GelCORE. 7 days after application, the

bioadhesive still had a smooth surface. GelCORE hydrogels were prepared by using 20% (w/v) total polymer concentration and 4 min light exposure time.

In addition, one day post-surgery, the implanted bioadhesives were transparent, revealing a smooth surface. In addition, the surrounding cornea was transparent and non-inflamed (**Fig. 8e**). AS-OCT also confirmed that the hydrogel was able to completely fill the defect and adhere to the stromal bed (**Fig. 8f,g**). One week after surgery, the bioadhesive could be still observed on the defect site in the cornea and remained transparent (**Fig. 8g**).

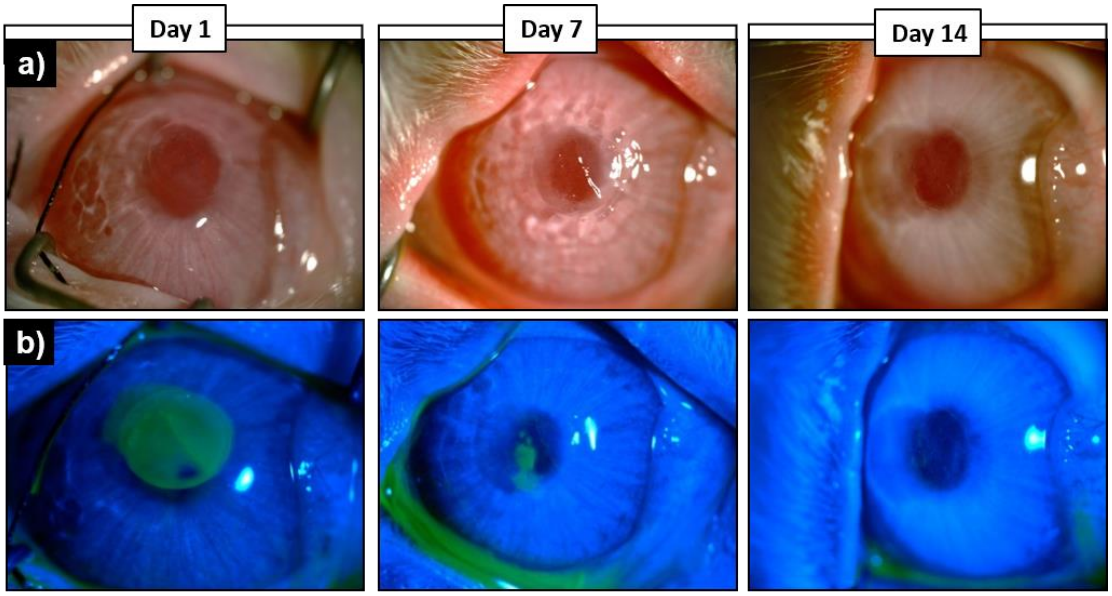

Figure 9. Corneal re-epithelialization after *in vivo* application of the bioadhesive to corneal defects in rabbit cornea. (a) Representative slit lamp photographs and **(b)** cobalt blue with fluorescein staining after *in vivo* application of GelCORE adhesive to rabbit cornea at different time points. Progressive reduction in the size of corneal epithelial defect (green area in the central cornea) implicates epithelial migration over GelCORE.

In addition, as shown in **Fig. 9a**, the adhesive hydrogels remained transparent at days 1, 7 and 14 after application. We also investigated whether there is migration of the epithelium over the adhesive hydrogel in the rabbit cornea. Cobalt blue slit lamp photographs with fluorescein staining

showed progressive reduction of the size of corneal epithelial defect (**Fig. 9b**), clearly implicating the migration of the epithelium over the bioadhesive, (fluorescein stains epithelial defects in green). By day 14 after application, the corneal epithelial defect over the bioadhesive was completely healed (**Fig. 9b**).

Moreover, histological evaluation of cryo-sectioned tissues revealed the strong adhesion of GelCORE bioadhesive to the stromal tissue after application (**Fig. 10b**). In addition, the results showed growth of non-inflammatory stromal tissue without any dominant deposition of a fibrous collagenous capsule after 14 days of application (**Fig. 10d**), which was similar to native cornea (**Fig. 10a**). Furthermore, histological assessment showed that thickness of the corneal stromal layer for GelCORE treated samples (582.2 ± 95.8 µm) was in the same range as that of the native rabbit cornea (554.9 ± 39.1 µm) (**Fig. 10e**). The stromal layer in untreated samples could not regenerate properly (**Fig. 10c**) and exhibited a thickness of 177.9 ± 39.3 µm (**Fig. 10e**). The thickness of the corneal epithelial layer was also evaluated histologically. Results revealed no statistically significant differences in the thickness of corneal epithelial layers in GelCORE treated, untreated, and native corneas (**Fig. 10f**). However, untreated samples showed comparatively larger standard deviation for thickness of corneal epithelial layer as compared to native tissue which indicates heterogenous re-epithelialization of untreated samples (**Fig. 10f**). The thickness of the corneal epithelial layer was also evaluated histologically. Results revealed no statistically significant differences in the thickness of corneal epithelial layers in GelCORE treated, untreated, and native corneas (**Fig. 10f)**. However, untreated samples showed larger standard deviation for thickness of corneal epithelial layer as compared to native tissue which indicates heterogenous re-epithelialization of untreated samples (**Fig. 10f)**. The immunostaining results (DAPI staining) also

indicated homogenous re-epithelialization in GelCORE treated group (**Fig. 10g-ii**) after 14 days, similar to native cornea (**Fig. 10g-i**).

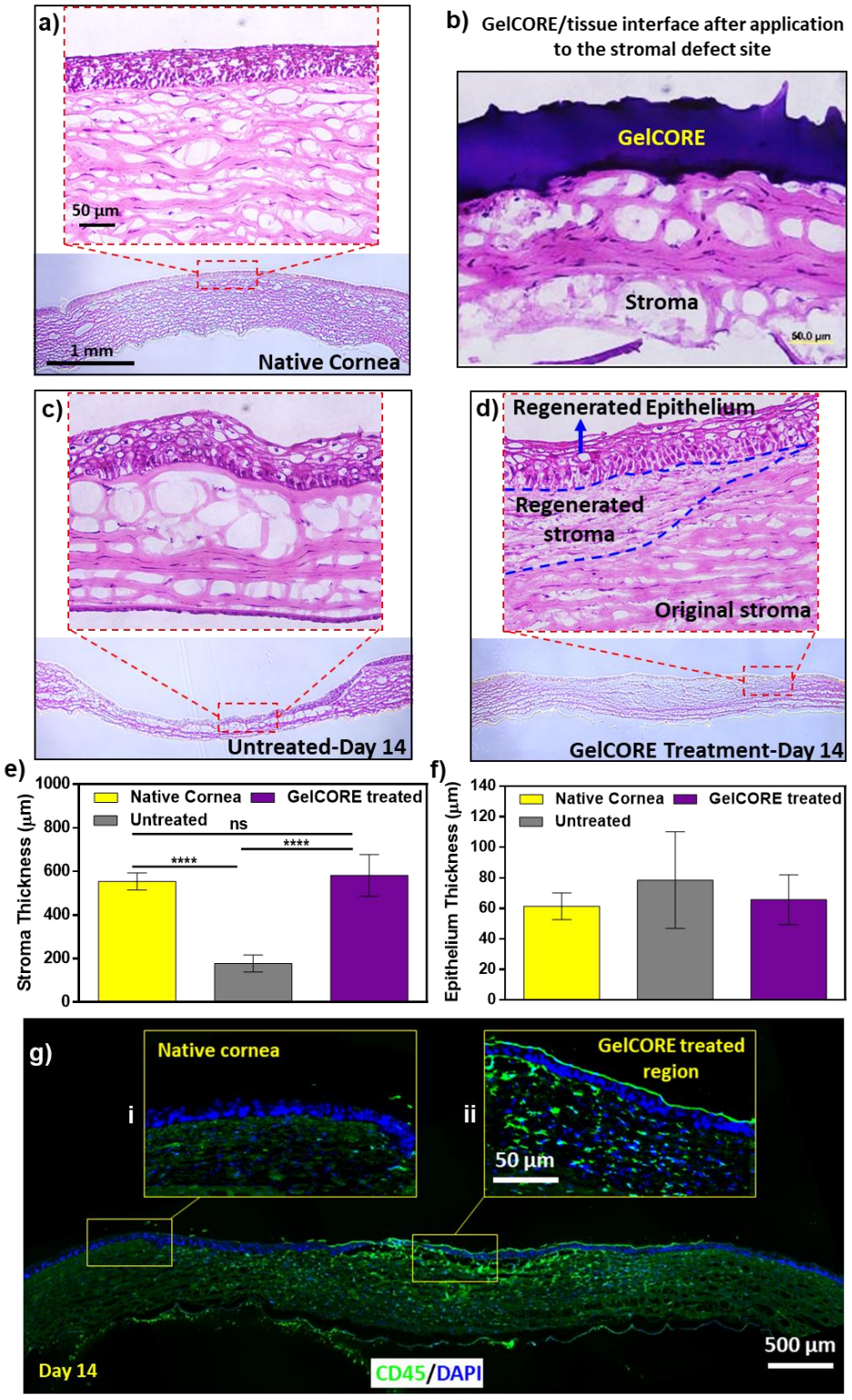

Figure 10. Histological analysis after application of GelCORE bioadhesive in a rabbit corneal stromal defect model. Representative Hematoxylin and Eosin (H&E) histopathology images from **(a)** native rabbit corneas (without defect), and **(b)** rabbit cornea after application of GelCORE in a 50%-depth stromal defect. Histological images for **(c)** untreated stromal defect (without bioadhesive), and **(d)** the defect treated with bioadhesive at day 14 post-surgery (scale bar = 50 μm, and 1 mm). **(e)** The thickness of stromal layer for the native cornea, GelCORE-treated, and untreated eyes at day 14 post-surgery obtained from histological images. **(f)** The thickness of epithelial layer for native cornea, GelCORE treated and untreated eyes at day 14 post-surgery obtained from histological images. **(g)** Representative fluorescent immunohistochemical image (DAPI and CD45 marker) **(i)** from the area without defect, and **(ii)** from corneal stromal defect treated with GelCORE bioadhesive at day 14 post-surgery. GelCORE hydrogels were prepared at 20% (w/v) total polymer concentration and 4 min light exposure time. Data are represented as mean ± SD (**$p < 0.01$, ***$p < 0.001$ and ****$p < 0.0001$, $n \geq 3$).

Moreover, leukocyte infiltration was detected by expression of CD45 maker in the GelCORE treated corneas, showing normal inflammatory responses during the regeneration process *[167]*(**Fig. 10g-ii**). In addition, an autologous tissue regeneration was observed for the defects treated with GelCORE bioadhesive after 14 days of application (**Fig. 10g-ii**). The cell nuclei within the new tissue showed the similarities between regenerated tissue and native tissue (**Fig. 10g**).

Other researchers have also aimed to develop tissue-engineered transplants for the treatment of corneal epithelial defects and stromal ulcers to reduce the dependence on donor corneas. However, the majority of these methods are based on prefabricated membranes [140] or patches [159], which typically require surgical equipment and skills. In addition, most of these prefabricated transplants are "passive" cell-based approaches which are potentially associated with high cell loss during implantation and immunogenicity [168, 169]. In contrast, our approach utilizes a biocompatible adhesive for sutureless and cell-free sealing and treatment of corneal stromal defects without

requiring advanced surgical procedures. Additionally, different tissue adhesives, including fibrin-based (i.e., fibrin glue, Tisseel®) and PEG-based (i.e., ReSure®) bioadhesives, have also been tested for ophthalmic applications. The major drawback of these adhesives is that they lack high adhesion to wet corneal tissue, nor do they have long retention [136]. Fibrin-based adhesives may also have the risk of transmitted diseases from pooled and single blood donors [170]. PEG-based bioadhesives also suffer from similar limitations including uncontrolled crosslinking which are impractical in a clinical setting, and lack the required mechanical properties that would efficiently promote regeneration [136].

Finally, an important feature of the GelCORE biomaterial is its ability to permit normal regenerative responses while it fills in corneal stromal defects of different size and geometry. This can lead to corneal tissue regeneration, encourages faster recovery of patients, reduces the need for future visual rehabilitative measures, and in some cases circumvent the need for corneal transplantation. Overall, our results showed that the bioengineered GelCORE hydrogels possess many advantages highlighted throughout this paper making them a promising substance to be used for corneal repair.

3.2. Multifunctional Photocrosslinkable Adhesive Hydrogels for Surgical and Tissue Engineering Applications

Hydrogels are three-dimensional (3D) networks of polymers with high water content and high permeability for the diffusion of essential nutrients and oxygen[171]. As hydrogels mimic the composition and structural properties of the native extracellular matrix (ECM), they possess remarkable potential to be used as scaffolds for regenerative medicine and tissue engineering applications [172]. However, hydrogel-based tissue-engineered scaffolds should not only have

high regenerative capacity and biocompatibility, but they should also possess adequate mechanical properties similar to the physiological tissues [104]. In addition, hydrogels intended for tissue repair should be able to adhere to the native tissues and remain mechanically stable in the defect site, for a period of time that allows for the regeneration of the damaged tissue [118]. Furthermore, the delivery of progenitor or terminally differentiated cells in combination with regenerative hydrogels could potentially accelerate biointegration and tissue repair at the site of injury [111]. This is particularly important in the context of tissues whose intrinsic regenerative capacity is limited, such as cartilage and bone. In addition, microbial infection is still one of the most severe postoperative complications in clinical orthopedics which can be treated by combining antimicrobial agents with hydrogels [173]. Hydrogel-based adhesive biomaterials used for tissue engineering often fail to integrate multiple therapeutic strategies into a single comprehensive approach to enhance the clinical efficacy of tissue engineered scaffolds [174]. Therefore, multifunctional biomaterials with optimal mechanical, adhesive, antimicrobial, and differentiation properties, would constitute a more effective therapeutic strategy over conventional single-strategy approaches for different tissue engineering applications.

In this section, we first demonstrate a photocrosslinkable, antimicrobial and elastic adhesive hydrogel engineered from naturally derived polymers (HA and ELP). This adhesive hydrogel could be potentially used for different surgical applications especially cartilage repair [175].

In section 3.2.2, we demonstrate another type of naturally derived, photocrosslinkable and multifunctional adhesive hydrogel with osteoinductive and antimicrobial properties. To engineer this hydrogel, we used GelMA hydrogel as the base material and induced the osteoinductivity of the hydrogel by incorporating silicate NPs. In addition, to impart antimicrobial properties, we incorporated an AMP (tet213) within the adhesive composite hydrogel.

3.2.1. Antimicrobial Adhesive Hydrogels

Various hydrogel-based biomaterials have been widely investigated in the context of cartilage tissue engineering, due to their ability to be used for 3D cell encapsulation, as well as their ease of modification, high water content, injectability, and biocompatibility[176]. For instance, different types of naturally-derived or synthetic-based hydrogels, such as chitosan[177, 178], HA[179-182], polyethylene glycol (PEG)[183], silk[184-186], collagen[187, 188], alginate[189, 190], and recombinant elastin-like polypeptides (ELPs)[191] have been used for the induction of cartilage tissue regeneration and repair[179, 192, 193]. Among the different biomaterials explored for cartilage tissue engineering, HA and ELPs have been shown to possess intrinsic properties that promote the regeneration of cartilage tissues[194-196]. ELPs are stimuli-responsive artificial biopolymers, whose macromolecular structure can be tailored through recombinant DNA techniques[197]. ELPs are derived from elastin, a highly elastic protein that is key for the proper function of cartilage tissues, owing to its role in resisting compressive loads and absorbing the mechanical forces acting on articular joints. Different types of ELPs have been investigated for cartilage tissue engineering, due to their tunable mechanical properties, high elasticity, and their ability to promote chondrogenic differentiation[196, 198]. However, the engineering of ELP-based hydrogels with controllable physical properties that can be rapidly crosslinked *in situ* remains technically challenging[121]. On the other hand, HA is a linear high molecular weight and non-sulfated glycosaminoglycan (GAG), which is one of the main components of the ECM found in connective tissues[199]. HA is involved in many physiological processes such as cell proliferation, migration, and morphogenesis, as well as new tissue formation[179]. It has been widely reported that HA promotes chondrogenesis by interacting with specific cell surface receptors such as CD44 and the hyaluronan-mediated motility receptor (RHAMM)[199-203]. However, previous studies

have reported that HA-based hydrogels undergo rapid biodegradation *in vivo*[204], and lack adequate mechanical stability due to the high hydrophilicity of HA[205]. Furthermore, hydrogels with increasing concentrations of HA often exhibit high mechanical stiffness and reduced elasticity and resilience, which may limit their potential application for cartilage tissue repair[206, 207]. Therefore, previous groups have investigated the engineering of hybrid hydrogels based on the combination of both HA and ELPs[191, 208]. However, these approaches were hindered by complex and time consuming chemistries, as well as uncontrollable and slow crosslinking rates.

In addition to mechanical properties, the adhesive properties of the hydrogels can be finely tuned to enhance the adherence of the biomaterial to the target tissue, and support tissue regeneration under physiological mechanical loads[209]. For instance, Wang *et al*. demonstrated the advantages of applying a primer layer to cartilage to enhance the adhesive strength of the biomaterial at the material-tissue interface[111]. However, the cells encapsulated in the implanted material were primary chondrocytes from another animal, which highly limits its translation into the clinical setting. In another study, Balakrishnan *et al*. developed an adhesive alginate/gelatin based hydrogel for cartilage tissue regeneration[189]. The engineered hydrogel could integrate well with host cartilage and facilitate migration and differentiation of chondrocytes. However, further improvement is required to use this adhesive hydrogel for treatment and management of the early stage of osteoarthritis, where defects are small and often associated with a poor healing mechanism[189]. Although the engineered hydrogels showed promising characteristics as adhesive biomaterials for cartilage tissue regeneration, the incorporation of antimicrobial agents in their structure can further improve their potential applications for cartilage repair in the actual clinical setting, which are generally affected by microbial infections.

Microbial infections are still associated with severe postoperative complications in orthopedic surgeries, due to the low vascularity of cartilage and host protein adsorption to implanted biomaterials *in vivo*[205]. Thus, the incorporation of antimicrobial agents into biomaterials, such as antibiotics, antimicrobial peptides, and metal nanoparticles have been investigated for the prevention of bacterial infection, biofilm formation, and rejection of biomedical implants[210]. Using metal oxide nanoparticles as antimicrobial materials is one of the most promising strategies for overcoming bacterial infections. In this regard, zinc oxide (ZnO) nanoparticles have been shown to elicit antimicrobial activity against antibiotic-resistant bacteria, through the disruption of bacterial cell membranes and the induction of reactive oxygen species[210]. Various types of antimicrobial biomaterials have been developed for cartilage tissue repair through incorporation of ZnO nanoparticles inside the hydrogel networks; however, most of these biomaterials were not adhesive to interlock to the native tissue or they suffered from lack of biocompatibily[211, 212]. Therefore, there is an unmet need to engineer multifunctional antimicrobial hydrogels with tunable biodegradation rates, and adequate mechanical properties and adhesive strength, which can promote cartilage tissue regeneration and repair.

Here, we describe the engineering of a new class of hybrid hydrogel adhesives for tissue engineering applications, based on the free radical photopolymerization of methacrylated HA (MeHA) and a custom ELP with photopolymerizable cysteine groups. In addition, we incorporated ZnO nanoparticles into the engineered hydrogels to impart them with antimicrobial activity. Liquid MeHA/ELP precursors can be readily delivered to the injury site and be rapidly photocrosslinked *in situ* in a safe and controllable manner. Chemical, physical and biological characterization of MeHA/ELP hydrogels, including compressive and tensile modulus/strength, water uptake capacity, porosity, *in vitro* antimicrobial activity, as well as *in vitro* and *in vivo* biocompatibility

were conducted. Furthermore, we evaluated the ability of MeHA/ELP hydrogels to induce the chondrogenic differentiation of 3D encapsulated human mesenchymal stem cells (hMSCs) *in vitro*. MeHA/ELP-ZnO hydrogels hold remarkable potential for cartilage tissue engineering applications, due to their highly tunable physical properties, as well as their intrinsic antimicrobial and chondroinductive properties.

3.2.1.1. Synthesis of MeHA/ELP hybrid hydrogels

In contrast to hydrogels synthesized from a single polymer network, hybrid hydrogels have been shown to better mimic the multifunctional nature of native physiological microenvironments[213]. Furthermore, the combination of different polymers with distinct physicochemical properties enables the fine tuning of the physical and biological properties of the engineered hydrogels[214]. In recent years, both MeHA and ELPs have emerged as remarkably promising biomaterials for various tissue engineering applications including cartilage repair. Since both MeHA and ELPs are derived from naturally occurring polymers, they mimic the composition of the native ECM and provide biologically relevant cues to cells *in vitro*. The genetically-encoded design of ELPs allows the modulation of the physical characteristics of the engineered tissue constructs[197]. Moreover, HA hydrogels have been shown to promote the deposition of cartilage-like ECM by chondrocytes and stem cells from different origins *in vitro*[206, 215]. Despite the remarkable chondroinductive properties of HA-based hydrogels, their uncontrolled *in vivo* degradation rate and poor elasticity often limit their application for cartilage tissue regeneration and repair[206, 207]. Therefore, we hypothesized that the incorporation of highly elastic ELPs into HA-based hydrogels could enhance the elasticity and resilience of the hydrogels, and improve their efficacy for cartilage repair. In addition, due to the slow *in vivo* degradation rate of ELP hydrogels[121], we anticipated that the addition of ELP could be used to modulate the biodegradation of the scaffolds *in vivo.*

Light-controlled radical polymerization is one of the most widely used methods for the local delivery of hydrogels for tissue engineering applications[216, 217]. In contrast to alternative methods such as chemical polymerization, the use of light enables the precise control over hydrogel formation, modification, shape, and the induction of specific responses in smart biomaterials[218]. In addition, due to the fast reactivity of methacrylate groups with radicals, they are one of the most commonly utilized groups for radical polymerization[219].

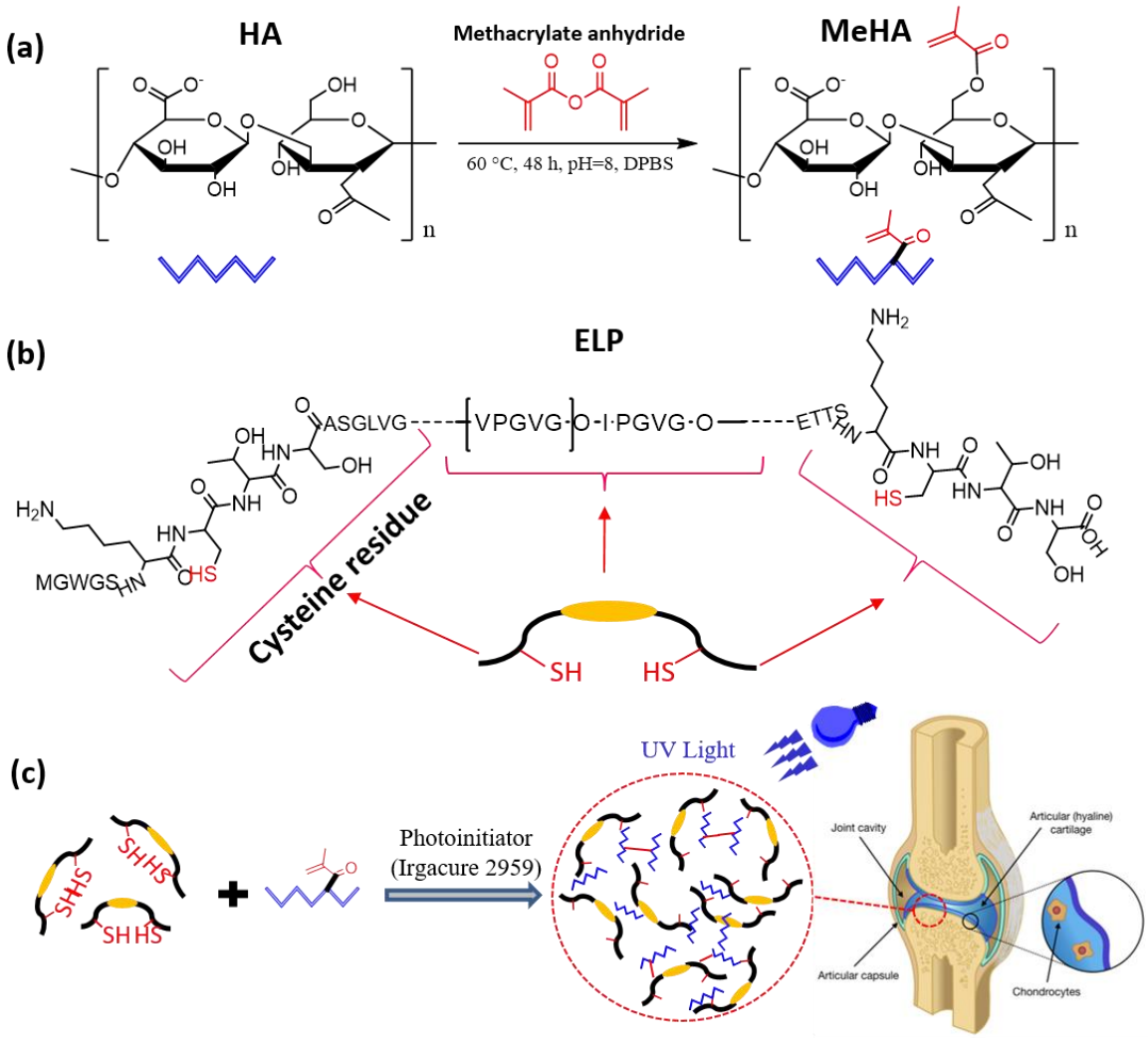

Figure 11. Schematic of MeHA/ELP hydrogel formation and chemical structure. (a) HA methacrylation process to form MeHA, **(b)** chemical structure of ELP, indicating the presence of cysteine residues, and **(c)** schematic diagrams of photocrosslinking of MeHA/ELP hydrogels and potential application of the cell-laden adhesive biocomposite.

Here, we synthesized MeHA by adding methacrylic anhydride to HA under basic conditions, which is one of the simplest and most widely used chemistries to generate photocrosslinkable MeHA (Fig. 11a)[220]. We then synthesized and purified a highly elastic photocrosslinkable ELP, based on a methodology described in our previous study[121]. We have previously shown that hydrogels based on this specific ELP exhibited high elasticity, long-term structural stability, and adequate host integration *in vivo*, without eliciting significant inflammatory responses[121]. The presence of thiol groups from cysteine residues in this ELP sequence allows for the formation of disulfide bonds and rapid photocrosslinking upon exposure to UV light (Fig. 11b). MeHA/ELP hydrogel precursors were prepared by combining different concentrations of MeHA (1 and 2% (w/v)) and ELP (0, 5, 10 and 15% (w/v)) with a 0.5% (w/v) solution of Irgacure 2959 in distilled water as a photoinitiator at 4 ^{o}C. To form MeHA/ELP hydrogels, the precursors were exposed to UV light for 120 sec. Upon exposure to UV light, the methacrylated groups in MeHA reacted with the thiol (-SH) groups in the cysteine residues of the ELPs, which led to rapid photocrosslinking and formation of the 3D hydrogel network[121, 219] (Fig. 11c). In contrast, previous studies on hydrogels synthesized via the combination of HA and ELP polymers suffered from comparatively more complex synthesis and poor processability[191, 208]. For instance, Zhu *et al.* recently described the synthesis of an HA/ELP hybrid hydrogel, in which the ELP required a time consuming (>20 days) chemical modification process (Hydrazine-modified ELP) to be able to react with the aldehyde-modified HA[208]. In addition, the gelation process occurred very rapidly after mixing the two components, which may limit the ability to form the hydrogel *in situ* for clinical applications. In another study, Moss *et al.* also described the engineering of an HA/ELP hybrid hydrogel, which required the incorporation of a third polymer (i.e., PEG diacrylate, PEGDA) as a crosslinker between the ELP and the thiol-modified HA to shorten the crosslinking

time (10-15 min). In contrast, in our study, MeHA/ELP prepolymers can be readily delivered to the affected area, and rapidly crosslinked *in situ* upon exposure to UV light in a controlled manner. The ability to easily control the photocrosslinking process combined with the high adhesion properties of the engineered hydrogel greatly increases the potential for the efficient clinical translation of MeHA/ELP hydrogels for cartilage regeneration and repair.

3.2.1.2.Mechanical characterization of MeHA/ELP hybrid hydrogels

In addition to biochemical stimuli, mechanical cues such as matrix stiffness and elasticity play a crucial role in the regulation of various cell processes and the promotion of new cartilage tissue formation[192]. Therefore, we characterized the mechanical properties of the engineered hydrogels synthesized with different concentrations of MeHA (i.e., 1 and 2% (w/v)) and ELP (i.e., 0, 5, 10 and 15% (w/v)) using cyclic compression test and tensile test (Fig. 12). Our results demonstrated that the unconfined compressive (Young's) modulus of MeHA/ELP hydrogels increased significantly by increasing ELP concentration from 0 to 15%, at both 1 and 2% MeHA concentrations (Figures 11a-b). For instance, for MeHA/ELP hydrogels containing 1% MeHA, the Young's modulus increased from 2.97 ± 2.5 kPa at 0% ELP to 13.1 ± 4.1 kPa at 15% ELP concentration (Figures 11a-b). In addition, the Young's modulus of MeHA/ELP hydrogels at 2% MeHA ranged from 14.8 ± 1.6 kPa to 39.9 ± 7.6 kPa by changing the ELP concentration (Figures 11a-b). Previous studies have reported the engineering of chitosan/HA[221] and fibrin/HA scaffolds[222] with a maximum compressive modulus of 7 kPa and 28 kPa, respectively. In addition, it was reported that the compressive moduli of hydrogels synthesized using different ELPs, such as ELP[KV7F-72][223] and ELP(KCTS-E 31-KCTS][121] were in the range of 4-11 kPa and 5-14 kPa, respectively. In contrast, our results demonstrated that the Young's modulus of hybrid hydrogels synthesized using 10% ELP and 2% MeHA (i.e., 39.9 ± 7.6 kPa) was higher than

those observed in previous studies. This behavior could be explained due to the formation of an interpenetrating network between the MeHA and ELP polymers. Our results also demonstrated that the energy loss at cycle 8 for MeHA/ELP hydrogels increased from 18.8 ± 0.5% to 28.2 ± 2.7% for hydrogels with 1% MeHA, and from 3.4 ± 2.8 to 19.4 ± 3.3% for hydrogels with 2% MeHA by increasing ELP concentration (Fig. 12c). Our previous work on ELP-based hydrogels demonstrated an energy loss of 35 - 51%[121] based on cyclic compression tests, which was remarkably higher than the values obtained for our MeHA/ELP composite hydrogels. The low energy dissipation during loading/unloading and high resilience of MeHA/ELP hydrogels highlight their potential for cartilage tissue repair.

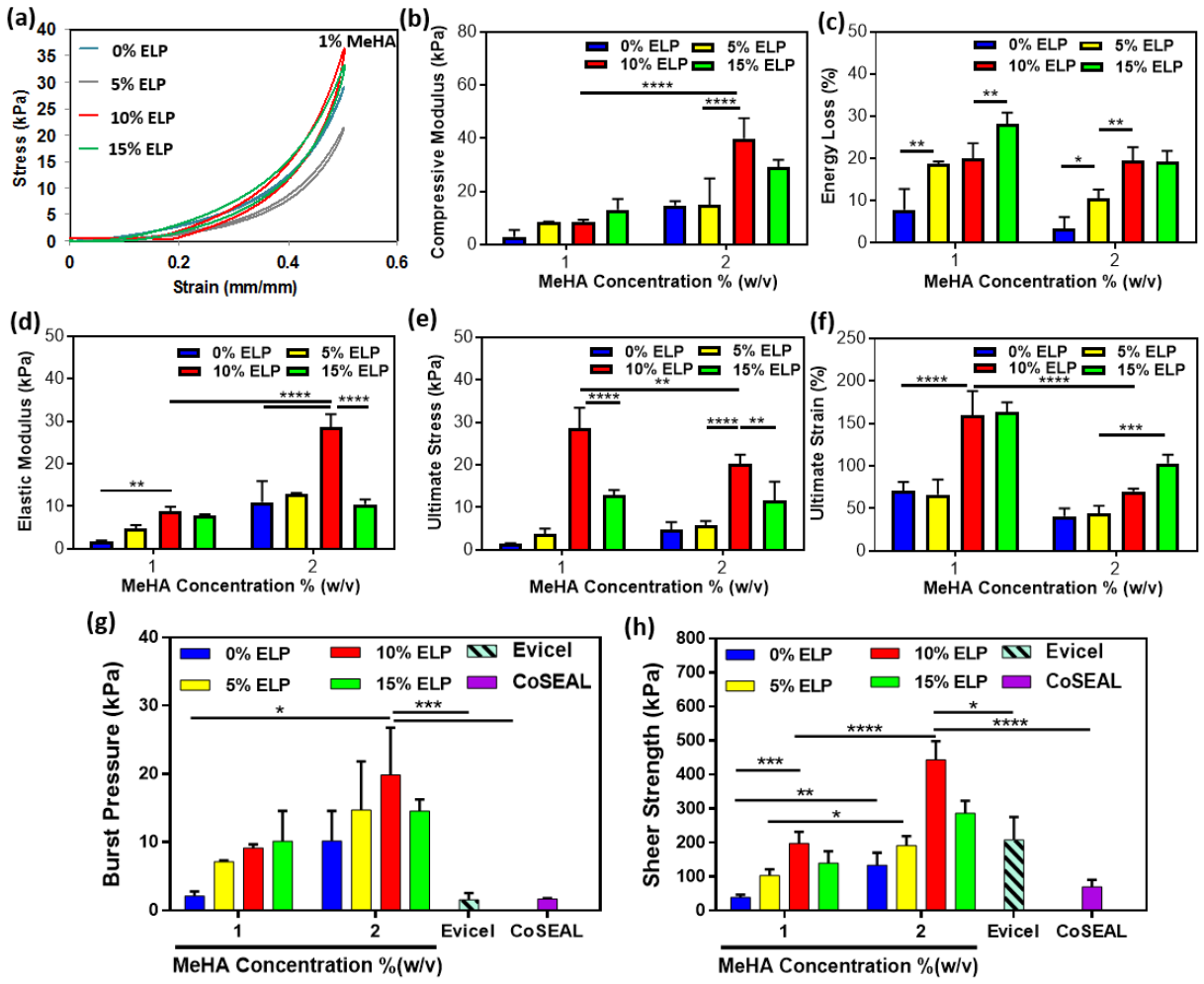

Figure 12. **Mechanical and adhesive properties of photocrosslinkable MeHA/ELP hybrid hydrogels.** **(a)** Representative compressive cyclic stress–strain curves of MeHA/ELP hydrogels produced by using different ELP concentrations and 2% MeHA. **(b)** Compressive (Young's) modulus and **(c)** Energy loss of MeHA/ELP hydrogels produced by using different MeHA and ELP concentrations. **(d)** Elastic modulus, **(e)** ultimate tensile stress and **(f)** ultimate tensile strain of MeHA/ELP hydrogels produced using different MeHA and ELP concentrations. **(g)** burst pressure resistance and **(h)** lap shear strength values for MeHA/ELP hybrid hydrogels produced by using different MeHA and ELP concentrations and commercially available sealants (* $p < 0.05$, ** $p < 0.01$, **** $p < 0.0001$).

The results from tensile tests demonstrated that the elastic modulus, ultimate stress, and extensibility (ultimate strain) of MeHA/ELP hydrogels could also be tuned by varying the concentrations of MeHA and ELP (Figures 11d-f). The engineered hybrids exhibited highly tunable elastic moduli in the range of 1.6 ± 0.4 kPa to 8.8 ± 1.1 kPa for hydrogels with 1% MeHA, and 10.9 ± 4.9 kPa to 28.9 ± 2.9 kPa for hydrogels with 2% MeHA, by varying the ELP concentration (Fig. 12d). In particular, hydrogels synthesized with 10% ELP and 2% MeHA exhibited the highest elastic modulus (i.e., 28.9 ± 2.9 kPa) (Fig. 12d). Our results also showed that the ultimate stress of the engineered materials increased from 1.6 ± 0.0 kPa to 28.7 ± 4.8 kPa for hydrogels with 1% MeHA, when the ELP concentration increased from 0% to 10% (w/v). In addition, the ultimate stress varied in the range of 4.7 ± 1.9 kPa to 20.3 ± 2.1 kPa for hydrogels synthesized with varying concentrations of ELP and 2% MeHA (Fig. 12e). Lastly, it was found that by increasing the ELP concentration from 0% to 15%, the extensibility of MeHA/ELP hybrids increased consistently from 70.9 ± 10.5% to 163.6 ± 11.4%, and from 40.9 ± 9.4% to 103.1 ± 10.3%, for hydrogels at 1% and 2% MeHA, respectively (Fig. 12f).

The mechanical properties of cartilage tissues vary substantially depending on the maturity of the organism, the distance from the articular surface, the development of disease, as well as during physiological compression and tension[224]. Therefore, materials used to engineer hydrogel

scaffolds for cartilage tissue engineering should possess highly tunable mechanical properties to achieve significant clinical relevance. Our results demonstrated that the combination of different concentrations of MeHA and ELP yielded hydrogels with a wide range of highly tunable mechanical properties. Therefore, the remarkable tunability brought about by the incorporation of both biopolymers makes the hybrid hydrogels highly promising biomaterials for engineering cartilage tissue constructs with different mechanical properties.

3.2.1.3. *In vitro* adhesive properties of MeHA/ELP hydrogels

High adhesion of implanted biomaterials to the surrounding tissue *in vivo* can prevent them from detaching from the target site and may promote biointegration. An optimal tissue/biomaterial integration promotes biocompatibility and effective tissue regeneration under physiological conditions[111]. We evaluated the *in vitro* adhesive properties of MeHA/ELP hydrogels using standard burst pressure and lap shear tests, and compared them to those of commercially available adhesives, Evicel® and Coseal™. These tests are particularly important to show the potential integration of adhesive hydrogel to the host tissue[189]. MeHA/ELP hydrogels showed consistently higher burst pressure values than commercially available sealants, as show in Fig. 12g. As expected, burst pressure increased with increasing concentrations of MeHA, with the highest burst pressure observed for hydrogels containing 2% MeHA and 10% ELP (19.87 ± 6.92 kPa). Furthermore, this value was nearly 13 times greater than the burst pressure obtained when using Evicel® (1.54 ± 0.99 kPa) and Coseal™ (1.68 ± 0.11 kPa) (Fig. 12g). The high burst pressure obtained for the engineered hydrogel adhesives is particularly important for cartilage tissue engineering, because it confirms that the hydrogels are able to tolerate *in vivo* intra-articular pressures[189]. In addition to orthogonal forces, tangential forces are applied in the actual *in vivo* conditions. It is expected that the MeHA/ELP adhesive hydrogels would exhibit significant

resistance against intra-articular pressures *in vivo,* due to their high burst pressure. However, further confirmation through animal experiments would be necessary[111, 189].

In agreement with the results of the burst pressure tests, the lap shear experiments indicated that the shear strength of the hydrogels increased with increasing concentrations of MeHA (Fig. 12h). Hydrogels containing 2% MeHA and 10% ELP exhibited the highest shear strength (443.1 ± 55.2 kPa), which constituted a 2-fold increase relative to Evicel® and a >6-fold increase relative to Coseal™. The high burst pressure and shear strength of hydrogels containing 2% MeHA and 10% ELP highlight their potential to be used as bioadhesives for different applications. Particularly, due to the mechanically harsh environment of the joints, presence of physiological shear stresses and loads in cartilage sites[111], it is expected that MeHA/ELP adhesive hydrogels can better adhere to and integrate with the native tissues as compare to those commercial available adhesive materials.

3.2.1.4. Pore characteristics and swelling ratios of MeHA-ELP hybrid hydrogels

The topological cues in physiological microenvironments (such as the porosity of the ECM) are critical in the modulation of cell proliferation and differentiation[121, 225]. Therefore, we characterized the pore characteristics of the engineered hybrid hydrogels using scanning electron microscopy (SEM). SEM images were acquired from lyophilized MeHA/ELP hybrid hydrogels containing 1% (Figures 12a-d) and 2% (Figures 12e-h) MeHA and different ELP concentrations. SEM images showed that the pore size, as well as the number of pores per sample, decreased consistently by increasing both MeHA and ELP concentrations. These observations were further supported by quantitative analysis of SEM images using the ImageJ software (Fig. 13i). For instance, the average pore size of MeHA/ELP hydrogels with 1% MeHA ranged from 66.7 ± 13.2 μm at 15% ELP to 92.0 ± 11.9 μm at 5% ELP (Fig. 13i). Similarly, the average pore size of

MeHA/ELP hydrogels with 2% MeHA ranged from 36.3 ± 6 μm to 70.1 ± 14.6 μm by varying the ELP concentration (Fig. 13i). Previous groups have described the engineering of elastin-based hydrogels that exhibited comparatively smaller pore sizes (i.e., ELP(KCTS-E 31-KCTS]: 6 μm, and α-elastin: 15 μm)[121, 226]. In contrast, the presence of larger pores in MeHA/ELP hydrogels could potentially favor the proper diffusion of nutrients and metabolites from the scaffold, as well as adequate cell proliferation and spreading.

Another important property of hydrogel scaffolds is their ability to undergo volumetric changes, in response to increased water uptake in physiological wet tissues. Therefore, we evaluated the swellability of MeHA/ELP hydrogels, by incubating them in phosphate buffer saline (PBS) at 37 °C for 24 h. Our results demonstrated that the maximum swelling was consistently obtained in all samples at 2 h post-incubation, with no significant changes after 24 h of incubation (Figures 12j and 12k).

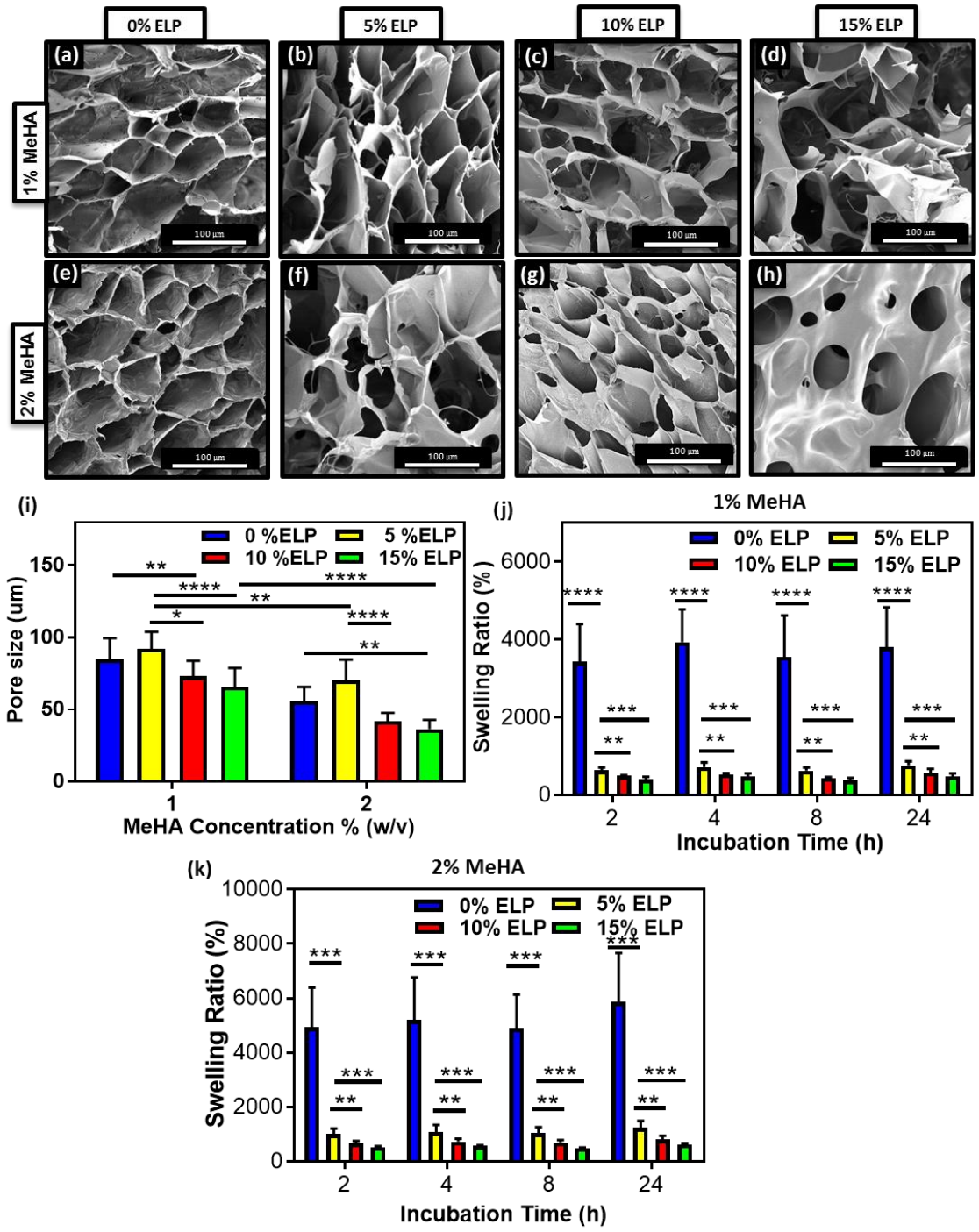

Figure 13. **Pore characteristics and swelling properties of photocrosslinked MeHA/ELP composite hydrogels.** Representative SEM images from the cross sections of the MeHA/ELP hydrogels produced by using 1% MeHA and **(a)** 0, **(b)** 5, **(c)** 10, and **(d)** 15% (w/v) ELP concentrations; and 2% MeHA and **(e)** 0, **(f)** 5, **(g)** 10, and **(h)** 15% (w/v) ELP concentrations (scale bar = 100 µm). **(i)** Effect of MeHA and ELP concentrations on the average apparent pore sizes of MeHA/ELP gels calculated from SEM images.

Swelling ratios of hydrogel produced by using various ELP concentrations and **(j)** 1% or **(k)** 2% (w/v) MeHA at 37 °C in DPBS (* $p < 0.05$, ** $p < 0.01$, *** $p < 0.001$, **** $p < 0.0001$).

In addition, our results also showed that the swellability of the hydrogels was significantly decreased due to the incorporation of ELP in hydrogels for both 1% (Fig. 13j) and 2% (Fig. 13k) MeHA concentrations. For example, the swelling ratios of hydrogels with 1% MeHA decreased from 3804 ± 1030% to 484 ± 76% by increasing ELP concentration from 0% to 15%. This observation could be explained by the fact that ELP based hydrogels contract and lose water content due to molecular rearrangement, at temperatures higher than their transition temperature[227]. Therefore, the combination of ELPs and MeHA could be used to modulate the water uptake capacity of hybrid hydrogels.

The tunable porosity of MeHA/ELP hydrogels allows the tuning of the microstructure of the scaffold to promote cell penetration and new autologous tissue ingrowth, as well as proper vascularization and nutrient diffusion[228]. In addition, previous works have demonstrated that a higher degree of swellability could help promote cartilaginous ECM deposition, but could also impact the mechanical properties of the scaffolds[229]. This characteristic is particularly important in the context of articular cartilage, due to its paramount role in mechanical support and load bearing in articular joints [179]. Furthermore, previous groups have also demonstrated that the swellability of the hydrogels also influences their potential to induce chondrogenic differentiation in 3D encapsulated hMSCs[230].

3.2.1.5. *In vitro* cytocompatilbity and chondrogenic differentiation of 3D encapsulated hMSCs in MeHA/ELP hydrogels

Bioactive scaffolds used for tissue engineering applications not only provide physical support, but they also influence cell survival through their interactions with different cell membrane receptors[231]. Different properties of hydrogel scaffolds have been shown to affect cell viability and proliferation, including material chemistry and functionalization with bioactive motifs, the addition of soluble autocrine factors, as well as nutrient and oxygen diffusion. Thus, we characterized the *in vitro* cytocompatibility and chondroinductive properties of the engineered MeHA/ELP hydrogels using 2D cultures of NIH-3T3 cells (unpublished data) and 3D encapsulation of hMSCs (Fig. 14).

We first evaluated the ability of NIH-3T3 fibroblasts to grow on the surface of MeHA/ELP hydrogels synthesized with 2% MeHA and 10% ELP concentrations (unpublished data). The *in vitro* cytocompatibility of MeHA/ELP hydrogels was evaluated using commercial live/dead and PrestoBlue assays, as well as Actin/DAPI fluorescent staining. These results demonstrated that MeHA/ELP hydrogels could support the proliferation and spreading of metabolically active cells, which is critical for their implementation in tissue engineering applications. For example, NIH-3T3 cells seeded on the surface of the engineered hydrogels showed high cell viabilities (>90%) and spreading during the first 5 days of culture (unpublished data). In addition, our results demonstrated that the metabolic activity (i.e., relative fluorescence units, RFUs) of NIH-3T3 fibroblasts increased more than 3-fold from day 1 to day 5 after cell seeding (unpublished data).

We then evaluated the ability of MeHA/ELP hydrogels to induce chondrogenic differentiation in 3D encapsulated hMSCs (Fig. 14). First, we characterized the viability (Figures 13a-b) and the ability of 3D encapsulated hMSCs to proliferate and spread (Fig. 14c-d) inside the hybrid hydrogels during the first 5 days post-encapsulation. hMSCs encapsulated within the scaffolds exhibited viabilities >90% up to 5 days after encapsulation (Fig. 14e). Previous works on

chondroinductive scaffolds based on the combination of gelatin methacrylamide/MeHA[232] and PEG/collagen[233] have reported significant drops in cell viability during the first week of 3D culture *in vitro*. This response was attributed to the limited diffusion of nutrients and waste across the 3D scaffold, the crosslinking density of the network, and the stress inflicted on cells due to the different encapsulation methods. In contrast, the viability of hMSCs encapsulated in MeHA/ELP hydrogels remained >90% throughout the first week of culture (Fig. 14e).

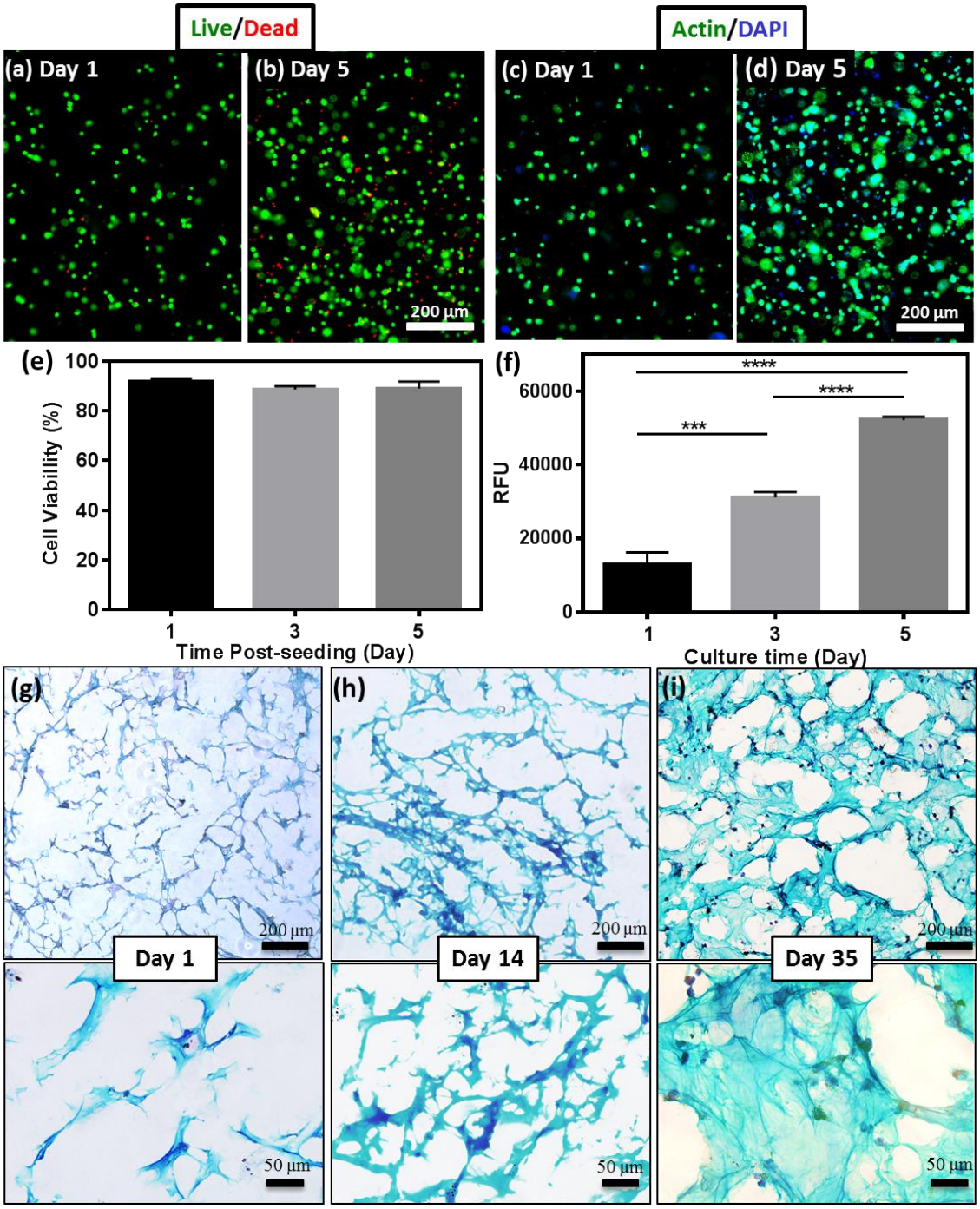

Figure 14. ***In vitro*** **3D encapsulation and differentiation of mesenchymal stem cells (MSCs) inside MeHA/ELP hybrid hydrogels.** Representative live/dead images of MSCs encapsulated within MeHA/ELP hydrogels after **(a)** 1 and **(b)** 5 days. Representative phalloidin (green)/DAPI (blue) stained images of cell-laden MeHA/ELP hydrogels after **(c)** 1 and **(d)** 5 days. Quantification of **(e)** cell viability and **(f)** metabolic activity RFU (relative fluorescence intensity) of MSC laden hydrogel using live/dead and PrestoBlue assays on days 1, 3, and 5 post encapsulation. Representative images of Alcian blue stained

from MSC-laden MeHA/ELP hydrogels to visualize glycoproteins of differentiated cells at days 1, 14, and 35 post encapsulation. Hydrogels were formed by using 2% MeHA and 10% ELP at 120 sec UV exposure time (** $p < 0.001$, *** $p < 0.0001$).

Fluorescent images revealed that hMSCs adopted a distinctive round morphology, which is indicative of chondrocytic lineages *in vitro* (Fig. 14d). Furthermore, these results also showed a consistent increase in the metabolic activity of 3D encapsulated hMSCs, as demonstrated by the PrestoBlue assay (Fig. 14f). In particular, the RFUs of encapsulated hMSCs increased from 12988 ± 3219 on day 1 to 52148 ± 861 on day 5 after encapsulation (Fig. 14f).

Next, we evaluated the cumulative deposition of tissue-specific ECM in MeHA/ELP hydrogels via histological staining. Our results showed that Alcian blue staining produced an increasingly stronger blue coloration in MeHA/ELP hydrogels after 35 days of culture (Fig. 14g-i). These results suggested that the encapsulated hMSCs could deposit cartilage-specific GAGs, in response to the chondroinductive activity of MeHA/ELP scaffolds. Furthermore, the effect of the ECM deposited by the differentiated hMSCs, as well as the cellular proliferation and growth, led to the extensive remodeling of the microarchitecture of the scaffold at day 35 (Fig. 14i), when compared to day 1 post encapsulation (Fig. 14g). Taken together, these results indicated that MeHA/ELP hydrogels could support the growth and proliferation of metabolically active 3D encapsulated hMSCs, as well as aid in the induction of cartilage-specific GAG deposition after 5 weeks of culture *in vitro*. However, MeHA/ELP hydrogels were also stained by the Alcian blue dye, due to the presence of HA in the scaffold. Therefore, further confirmation of the chondrocytic differentiation of hMSCs using alternative methods, such as immunohistochemistry or qRT-PCR will be conducted in the future.

Previous studies have explored the use of ECM-derived molecules to engineer scaffolds for cartilage tissue engineering, as well as for chondrocyte delivery for cartilage repair. For instance, collagen type I is currently being used in the clinic for matrix-based autologous chondrocyte transplantation, and has also been extensively used to engineer hydrogel scaffolds for tissue engineering applications[234-236]. These bioactive hydrogels have been shown to induce chondrogenic differentiation of hMSCs through the interactions between cell membrane integrins and specific peptide motifs in the ECM-derived components of the scaffolds[233]. Other studies have also explored the influence of scaffold chemistry in chondrogenesis, by encapsulating hMSCs in HA-based hydrogels[207, 237, 238]. However, these approaches required prolonged exposure times to UV light (10 min), which could potentially lead to decreased cell viability or DNA damage. In contrast, MeHA/ELP hydrogels can be rapidly crosslinked, which greatly minimizes biosafety concerns associated with UV-based chemistries. In addition, the incorporation of ELPs into MeHA/ELP hydrogels synergizes the bioactivity of the scaffolds, while also enabling the fine-tuning of their physical properties.

3.2.1.6. *In vitro* antibacterial properties of the hybrid hydrogels

The development of infection still constitutes one of the most severe postoperative complications in clinical orthopedics. Infections occur due to bacterial adhesion and colonization across the surface of implanted biomaterials, which ultimately leads to the formation of a biofilm that protects pathogenic bacteria against phagocytosis and antibiotics[173]. In addition, the misuse and over prescription of antibiotics have led to the development of antibiotic-resistant bacteria. Therefore, significant efforts have been made towards the development of antimicrobial hydrogels that can prevent biofilm formation and implant rejection[239, 240]. One of the most promising experimental strategies for overcoming antibiotic resistance in pathogenic bacteria is the use of nanoparticle-based alternatives. For instance, ZnO nanoparticles have been shown to elicit

antimicrobial activity against antibiotic-resistant bacteria, through the disruption of bacterial cell membranes and the induction of reactive oxygen species[210].

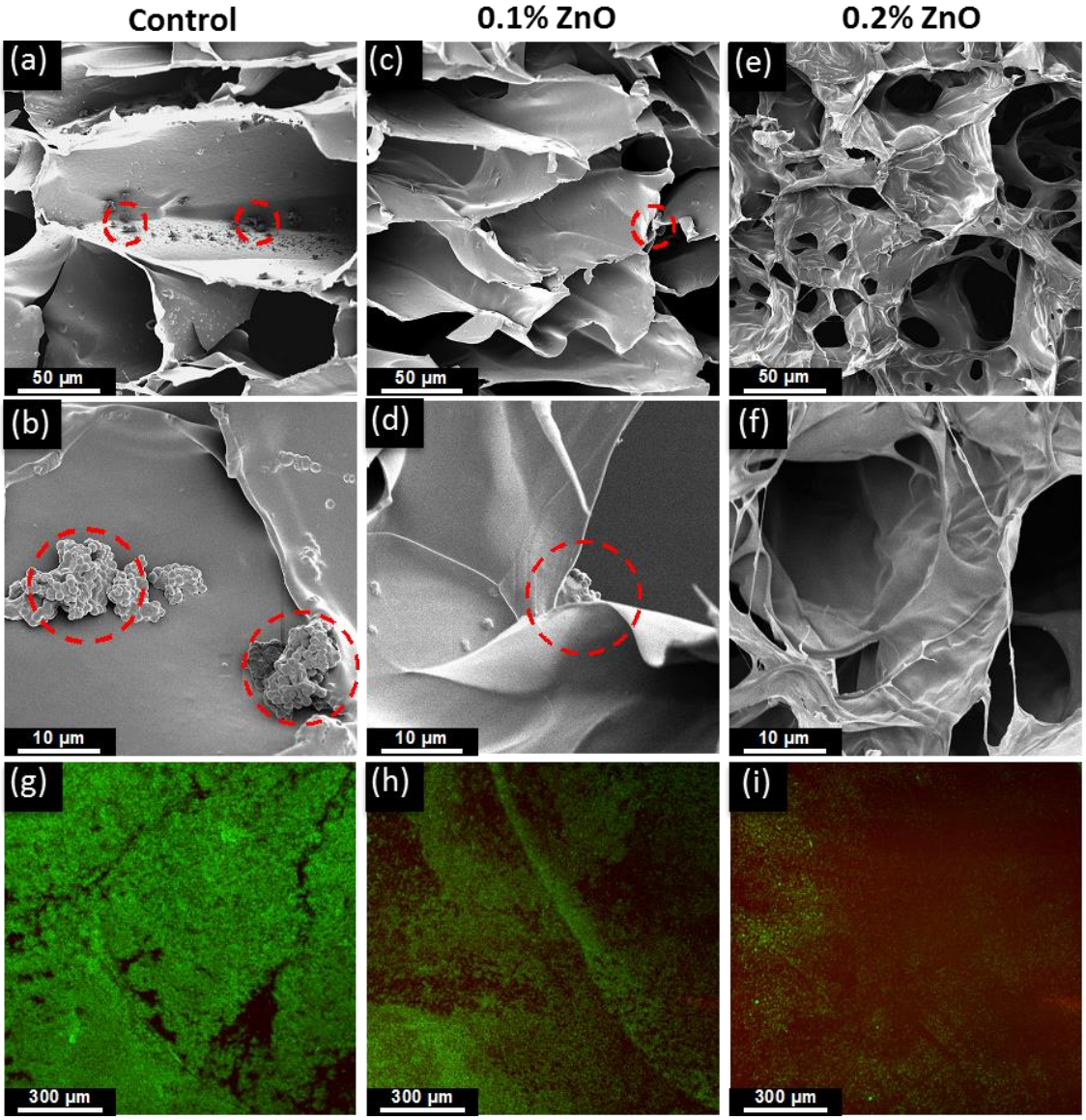

Figure 15. *In vitro* bacterial seeding on MeHA/ELP-ZnO hydrogels with different ZnO concentrations. Representative SEM images of methicillin-resistant Staphylococcus aureus (MRSA) colonization on MeHA/ELP-ZnO hydrogels containing **(a, b)** 0% ZnO, **(c, d)** 0.1% ZnO and **(e, f)** 0.2% ZnO. Clusters of bacteria are shown in dashed circles. **(g)** Representative live/dead images from bacteria seeded MeHA/ELP-ZnO hydrogels containing **(g)** 0% ZnO, **(h)** 0.1% ZnO, and **(i)** 0.2% ZnO after 1 day of incubation. Hydrogels were formed by using 2% MeHA and 10% ELP at 120 sec UV exposure time.

Here, we incorporated different concentrations of ZnO nanoparticles (0%, 0.1% and 0.2% (w/v)) to impart antimicrobial properties to MeHA/ELP hydrogels synthesized using 2% MeHA and 10% ELP concentrations. We investigated the antimicrobial activity of the resulting MeHA/ELP-ZnO nanocomposites against methicillin-resistant *Staphyloccocus aureus* (MRSA). For this, we relied on direct visual inspection of the hydrogels seeded with bacteria via SEM, as well as colony forming units (CFU) and live/dead assays. SEM micrographs showed that the samples containing 0.0% ZnO (controls) exhibited extensive bacterial infiltration within the pores, as well as across the surface of the scaffolds (Fig. 15a-b). The incorporation of 0.1% ZnO into the hydrogel network provided limited protection against MRSA colonization, as shown by the persistence of bacterial clusters located mostly on the surface of the scaffolds (Fig. 15c-d). In contrast, hybrid hydrogels containing 0.2% ZnO exhibited high antimicrobial activity as demonstrated by the complete absence of bacterial clusters both inside and on the surface of scaffolds (Fig. 15e-f). We then evaluated bacterial cell viability within MeHA/ELP-ZnO hydrogels using the BacLight live/dead cell viability assay (Fig. 15g-i). Fluorescent images suggested that the number of viable (green) bacterial cells inside the hydrogels decreased via the incorporation of 0.1 and 0.2% ZnO, when compared to control hydrogels (Fig. 15g-i). These observations were further supported by the CFU assay, which showed that the number of CFUs decreased from 40.7±8.1 at 0.0% ZnO, to 38.3±5.5 at 0.1% ZnO and 28.3±4.7 at 0.2% ZnO concentration.

Previous studies have reported the incorporation of ZnO nanoparticles into chitosan and alginate-based hydrogels to impart antimicrobial properties[212, 241]. However, the incorporation of metal oxide nanoparticles into these types of hydrogels has been shown to exert a negative effect on cell viability. For instance, Mohandas *et al.* reported a >2-fold reduction in cell viability after the addition of ZnO nanoparticles to alginate hydrogels[212]. In contrast, our results demonstrated

that MeHA/ELP-ZnO hydrogels exhibited high antimicrobial activity, without compromising cell viability and spreading (unpublished data). For instance, the RFUs of NIH-3T3 cells measured by the PrestoBlue assay, increased 1.9-fold from day 1 to 5 of culture. In addition, our findings showed that the incorporation of ZnO nanoparticles resulted in no significant changes in both the elastic and Young's moduli of MeHA/ELP hydrogels at 2% MeHA and 10% ELP). Taken together, these results demonstrated that MeHA/ELP-ZnO hydrogels could be effectively implemented in the engineering of chondroinductive adhesive hydrogels that are resistant to bacterial colonization.

3.2.1.7. *In vivo* biodegradation and biocompatibility of the engineered MeHA-ELP hybrid hydrogels

Hydrogels used for tissue engineering applications should not induce inflammatory or foreign body responses when surgically implanted *in vivo*[121]. In addition, they should be effectively biodegraded into biocompatible byproducts, while allowing sufficient time for tissue regeneration. Thus, we evaluated the *in vivo* biodegradation and biocompatibility of MeHA/ELP hydrogels via subcutaneous implantation in rats. For this, cylindrical (8 mm diameter by 2 mm height) hydrogels were synthesized using 2% MeHA and 10% ELP concentrations. Hydrogels were lyophilized and weighed, and the dried samples were then subcutaneously implanted in the dorsum of male Wistar rats. Implanted samples were retrieved and weighed at 3, 14, 28, and 56 days post implantation, and analyzed via direct visual inspection, and histological and immunofluorescent staining. Visual inspection of the explanted samples showed that the average volume of the hydrogels decreased significantly throughout the duration of the experiment (69 ± 11 % after 56 days) (Figures 15a-b). This change in the volume of the samples was likely due to the biodegradation of the hydrogels via enzymatic hydrolysis[121].

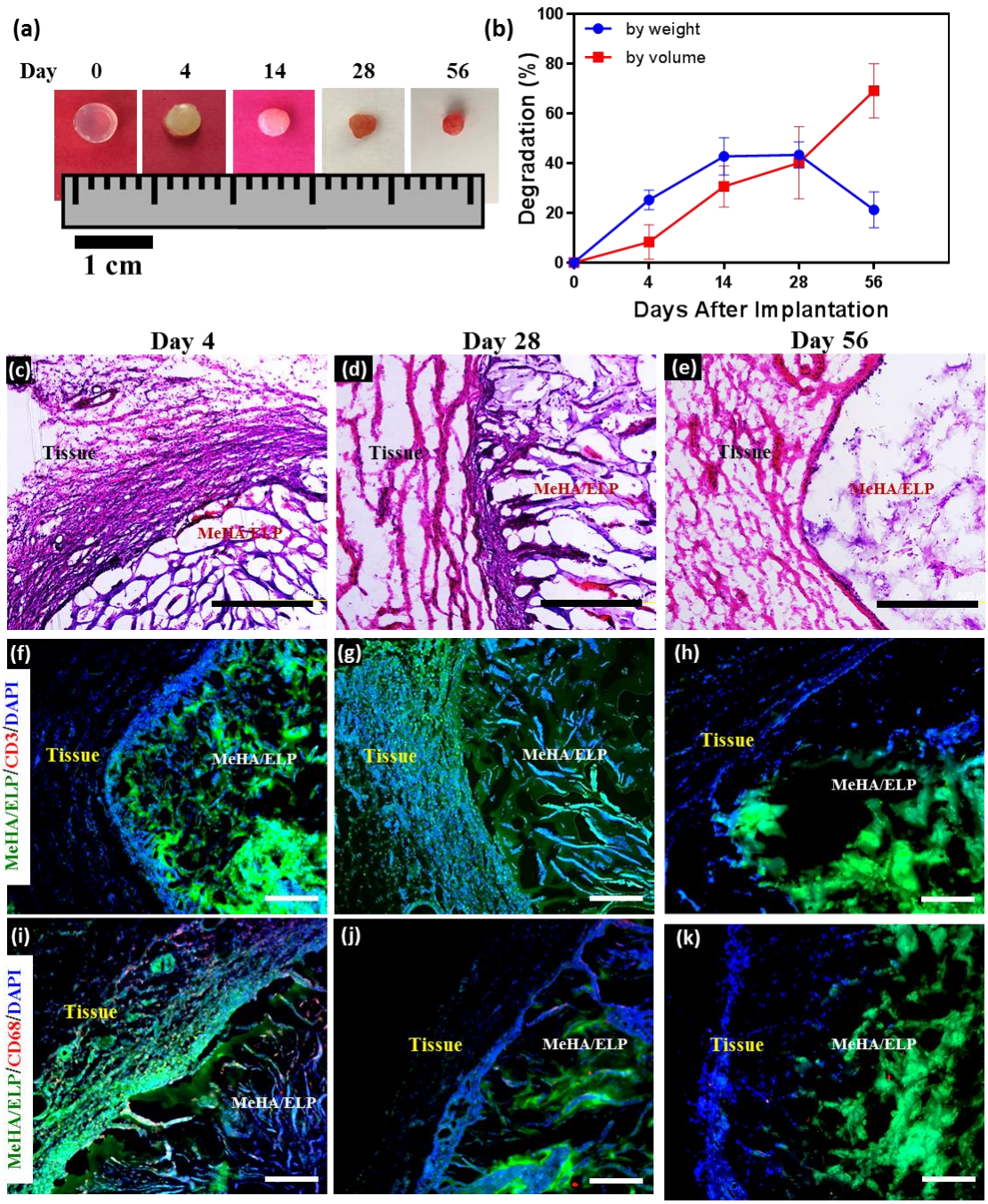

Figure 16. ***In vivo*** **biocompatibility and biodegradation of MeHA/ELP hybrid hydrogels in a rat subcutaneous implantation model**. **(a)** Representative images of MeHA/ELP hydrogels before implantation (day 0) and on days 4, 14, 28, 56 post-implantation. **(b)** *In vivo* biodegradation of MeHA/ELP hydrogels on days 0, 4, 14, 28 and 56 of implantation, based on weight and volume loss of the implants (n = 4). The *in vivo* degradation profile of MeHA/ELP hydrogels shows an approximately linear degradation behavior by volume during the first 56 days after implantation, as well as the highest biodegradation by weight between days 14 and 28. Hematoxylin and eosin (H&E) staining of MeHA/ELP sections (hydrogels

with the surrounding tissue) after **(c)** 4 days, **(d)** 28 days, and **(e)** 56 days of implantation (scale bars = 500 μm). Immunohistofluorescent analysis of subcutaneously implanted MeHA/ELP hydrogels showing no significant local lymphocyte infiltration (CD3) at days **(f)** 4, **(g)** 28 and **(h)** 56 post-implantation (scale bars = 200 μm). Fluorescent images showed transient macrophage infiltration (CD68) at day 4 **(i)**, followed by no apparent positive fluorescence at days **(j)** 28 and **(k)** 56 post-implantation (scale bars = 200 μm). Green, red and blue colors in **(f-k)** represent the MeHA/ELP autofluorescent hydrogels, the immune cells, and cell nuclei (DAPI), respectively. Hydrogels were formed by using 2% MeHA and 10% ELP at 120 sec UV exposure time.

The average degradation based on the weight of the explanted samples also increased from 25.2 ± 3.9% at day 14 to 42.7 ± 7.5% at day 28 and dropped to 21.2 ± 7.2% on day 56 post implantation (Fig. 16b). This decrease in the degradation rate might be due to the ingrowth of new autologous tissue within the engineered hydrogels, which led to an increase in the weight of the explanted sample on day 56 (Fig. 16b). This observation was also apparent after visual inspection of the explanted samples (Fig. 16a). These results were in agreement with our previous work, which demonstrated that ELP implants allowed the ingrowth of predominantly non-inflammatory tissue into the scaffold[121]. The efficient control over the biodegradation rate of the hydrogels enables their fine-tuning for different tissue engineering applications. Previous studies have demonstrated that both MeHA[242, 243] and ELP[197, 244, 245] can be effectively biodegraded *in vivo*, and that the rate at which this process occurs can be controlled by modifying their biochemical composition. These observations suggest that the biodegradability of the hybrid hydrogels can be finely tuned not only by varying the concentration of MeHA and ELP biopolymers, but also by further modifying their biochemical structure. Therefore, the tunable biodegradability of MeHA/ELP hydrogels could prove greatly advantageous for the engineering of biomaterials for different biomedical and tissue engineering applications.

Lastly, we evaluated the immunogenicity of the engineered hydrogels, via histological and immunohistochemical analysis of subcutaneously implanted samples. Hematoxylin/eosin (H&E) staining revealed that the hybrid hydrogels were efficiently biodegraded and replaced by new autologous tissue, without any apparent signs of fibrous capsule formation (Figures 15c-e). The degree of inflammatory cell recruitment into the gel site was evaluated via immunofluorescent staining using antibodies against the lymphocyte (CD3) and macrophage (CD68) associated antigens. These results showed no detectable lymphocyte invasion (CD3, red) throughout the duration of the experiment (56 days) (Figures 16f-h). In addition, immunofluorescent staining against the CD68 antigen showed minor macrophage infiltration at day 4 post-implantation (Fig. 16i). However, we did not detect any observable fluorescence for the CD68 antigen at days 28 and 56 post-implantation (Fig. 16j-k). These results indicate that MeHA/ELP hydrogels possess high biocompatibility *in vivo*, as demonstrated by the absence of any sustained inflammatory responses from the host organism. Taken together, these observations suggest that the engineered hybrid hydrogels can be used to engineer chondroinductive scaffolds for regenerative tissue engineering, due to their tunable biodegradability and high biocompatibility.

In this section, we engineered a new class of phtocrsslinkable adhesive hydrogels using MeHA and ELP, with antimicrobial properties for different tissue engineering applications in particular cartilage repair. MeHA/ELP hydrogels exhibited a wide range of highly tunable physical properties, including mechanical strength, elasticity, adhesion strength, porosity, and swellability. Standard lap shear and burst pressure tests revealed that MeHA/ELP hydrogels exhibited higher adhesive strength, compared to commercially available tissue adhesives such as Evicel® and Coseal™. *In vitro* studies also demonstrated that the engineered hydrogels were cytocompatible and could induce the chondrogenic differentiation of hMSCs, as demonstrated by histological

evaluation of cartilage-specific GAGs deposition. In addition, the incorporation of ZnO nanoparticles into MeHA/ELP hydrogels provided high antimicrobial activity against MRSA *in vitro*. *In vivo* subcutaneous implantation showed that MeHA/ELP hydrogels could be biodegraded and integrated into the host surrounding tissues, without eliciting any significant inflammatory responses. Taken together, our results suggest that MeHA/ELP-ZnO hydrogels have the potential to be used for different tissue engineering applications especially cartilage repair, due to their tunable physical and mechanical properties, as well as their intrinsic chondroinductive activity and antimicrobial properties.

In the following section, we introduce another class of antimicrobial adhesive hydrogels which can strongly integrate into the native tissue and enhance tissue regeneration. However, to synthesize the antimicrobial properties, we replaced ZnO with antimicrobial peptides, due to significant advantages of the AMPs. The engineered multifunctional hydrogel can be used for different tissue engineering and surgical application. One possible application could be treatment of peri-implant diseases which will be discussed in detail in the following section.

3.2.2. Osteoinductive and antimicrobial adhesive hydrogels

In recent years, significant efforts have been made to develop macromolecular antimicrobial agents that are impervious to antibiotic resistance, and can be used in the context of wound healing, bone and dental applications [62]. The antimicrobial activity of ZnO nanoparticles and their potential applications for the development of hard and soft tissue healing have been extensively reported in the literature [68,69]. Also, in previous section, we demonstrated engineering of a ZnO based antimicrobial adhesive hydrogel for tissue engineering applications, especially for cartilage tissue repair. However, recent studies have reported the adverse implications of ZnO nanoparticles

in metal homeostasis [70] and cardiac function [71]. To solve this issue, other alternatives for metal oxide NPs as antimicrobial agents needs to be considered. In this regard, in one of our previously published works, we introduced a new class of multifunctional hydrogel adhesives for the treatment of chronic non-healing wounds [104]. Composite hydrogels were synthesized from two naturally derived biopolymers, MeTro and GelMA. The synergistic association of two biopolymers with distinct physicochemical properties enabled fine-tuning of various properties of the composite hydrogels including mechanical properties, in vitro and in vivo degradation, swellability, and porosity. The adhesive properties of the composite hydrogels were shown to be readily tunable to different physiological scenarios and comparatively superior to commercially available tissue adhesives. Incorporation of an antimicrobial peptide (Tet213) to the hydrogel network provided a wide spectrum antibacterial properties to MeTro/GelMA-AMP hydrogels, which was significantly more potent than ZnO nanoparticles. In addition, our results suggest that a qualitatively and quantitatively similar antimicrobial activity can be achieved using a concentration of AMP that is 30-fold lower than that of ZnO nanoparticles (i.e., 0.1% (w/v) AMP vs. 3% (w/v) ZnO). MeTro/GelMA-AMP hydrogels were shown to support the growth, spread, and proliferation of both, 2D surface seeded and 3D encapsulated fibroblasts in vitro. Furthermore, MeTro/GelMA-AMP hydrogels elicited minimal inflammatory responses, and were shown to be efficiently biodegraded in vivo when implanted subcutaneously in a murine animal model. Taken together, our results demonstrated the remarkable potential of MeTro/GelMA-AMP hydrogels for the engineering of sutureless regenerative and antimicrobial hydrogel adhesives, which could prevent infection and promote healing of chronic wounds.

Therefore, based on our previous published work, the use of peptide-based antimicrobial strategies provides a viable alternative that could help circumvent the known limitations associated

with ZnO, and aid in the engineering of safer approaches for the management of wound healing process.

AMPs are comprised of short sequences of cationic amino acids, which have been shown to possess broad spectrum bactericidal activity against G(+/-) bacteria [63]. AMPs bind to the negatively charged outer leaflet of bacterial cell membranes, which leads to changes in bacterial surface electrostatics, actuation upon cytoplasmic targets, increased membrane permeabilization, and ultimately, cell lysis [104].

In this section, we aimed to provide antimicrobial capabilities to the engineered GelMA hydrogels through the incorporation of a broad-spectrum AMP. In order to engineer an osteoinductive multifunctional adhesive hydrogel, we incorporated disc shaped silicate NPs (laponite) into the bioadhesive. The potential applications of these adhesive hydrogels can be different hard tissue healing and regeneration such as bone and dental applications. For example, Peri-implant diseases (PIDs), which include peri-implant mucositis (PIM) and peri-implantitis (PI), are inflammatory conditions affecting the tissues that surround dental implants [246].

As dental implants have become the standard of care for tooth replacement, the number of patients affected by peri-implant diseases (PIDs) is increasing [247]. PIDs include peri-implant mucositis (PIM), which is characterized by the inflammation of the soft tissue surrounding the implants, and peri-implantitis (PI), which is characterized by bone loss around the implants [247]. Since implant placements continue increasing, it is predicted that PIDs will become one of the most significant dental diseases of the future [248].

PIM is treated with nonsurgical procedures, which include mechanical debridement alone or in combination with local delivery of antibiotics [249]. However, because of their inability to efficiently antagonize the infection, these approaches do not treat PIM effectively [250, 251]. PI

is treated by means of surgical approaches, which include various bone regenerative strategies [252, 253]. However, the use of autografts, allografts, xenografts, and alloplasts, with or without the use of antibiotics, has shown limited success [252, 253]. INFUSE®, a novel commercially available product for bone regeneration, based on the combination of human recombinant bone morphogenetic protein 2 (hrBMP2) and collagen, has also been proposed for implant re-osseointegration [254]. Yet, the uncontrolled release rate of the growth factor [52] and the potentially harmful side effects associated with hrBMP2 [255, 256] severely limit its application in PI regenerative procedures. Currently, there are no commercially available products that combine antimicrobial and osteoinductive strategies; therefore, clinical management of PI remains challenging. Therefore, the engineering of therapeutic approaches that could enable compartmentalized tissue healing by sealing the affected area and thus preventing migration of bacteria and other unwanted cells to the healing site [257, 258], may improve clinical outcome in patients with PIM and PI.

It has been shown that silicate nanoparticles (SNs) can induce osteogenic differentiation of human mesenchymal stem cells (hMSCs) in vitro [259-264]. Thus, we hypothesize that incorporation of SNs can potentially enhance osteoinduction and bone regeneration, while also reducing the amount of recombinant growth factors delivered to the treated area.

Here, we propose to engineer a visible light crosslinkable adhesive and antimicrobial hydrogel with tunable physical properties with or without osteoinductive activity, for the treatment of PIDs. The antimicrobial adhesive could be used for the treatment of PIM, while the further incorporation of osteoinductive properties is intended for treatment of PI. First, physical properties of the multifunctional adhesives were evaluated. The adhesion properties of the hydrogels were then tested based on ASTM standard tests. Next, the antimicrobial properties of the hydrogel against

Porphyromonas gingivalis (p. gingivalis) were evaluated. The in vitro cytotoxicity of the adhesive hydrogels was then evaluated, and finally to test whether the hydrogel adhesives could be effectively utilized in vivo without risks of displacement during the healing process, we delivered GelMA precursor to bone defects artificially created in mouse calvaria.

3.2.2.1. Synthesis and physical characterization of the adhesive hydrogels

To engineer a biomaterial that possesses all the characteristics needed for the treatment of PIM, we have synthesized a rapidly photocrosslinkable, antimicrobial and adhesive GelMA-based hydrogel. The synthesis process was very similar to synthesis of elastic and adhesive hydrogels in section 3.1.1. Briefly, these hydrogels were formed by the photochemical reaction of methacryloyl groups, available on GelMA chains using Eosin Y as photoinitiator, TEA as an initiator, and VC as a catalyst (visible light in the range of 450 to 550 nm) 1, 3. We also incorporated AMP into the hydrogels to impart antimicrobial properties. In addition, different concentrations of SNs were incorporated into the hydrogels to make it osteoinductive.

3.2.2.2. Physical characterization of osteoinductive adhesive hydrogels

As previously mentioned, in this section, we engineered a visible light crosslinkable adhesive and antimicrobial hydrogel with tunable physical properties with or without osteoinductive activity, for the treatment of PIDs. The antimicrobial adhesive could be used for the treatment of PIM, while the further incorporation of osteoinductive properties is intended for treatment of PI. Regenerating bone after PI remains technically challenging due to the limited efficacy of currently available materials used as bone grafts in the clinical setting [52, 254-256]. To address these limitations, we aim to engineer an osteoinductive adhesive for the treatment of PI, by incorporating osteoinductive SNs to the formulation of GelMA optimized in previous section. To do this,

different concentrations of SNs were loaded into GelMA precursor solution prior to photopolymerization to form osteoinductive hydrogels. The physical properties of the engineered adhesive composite were characterized as shown in Figure 20.

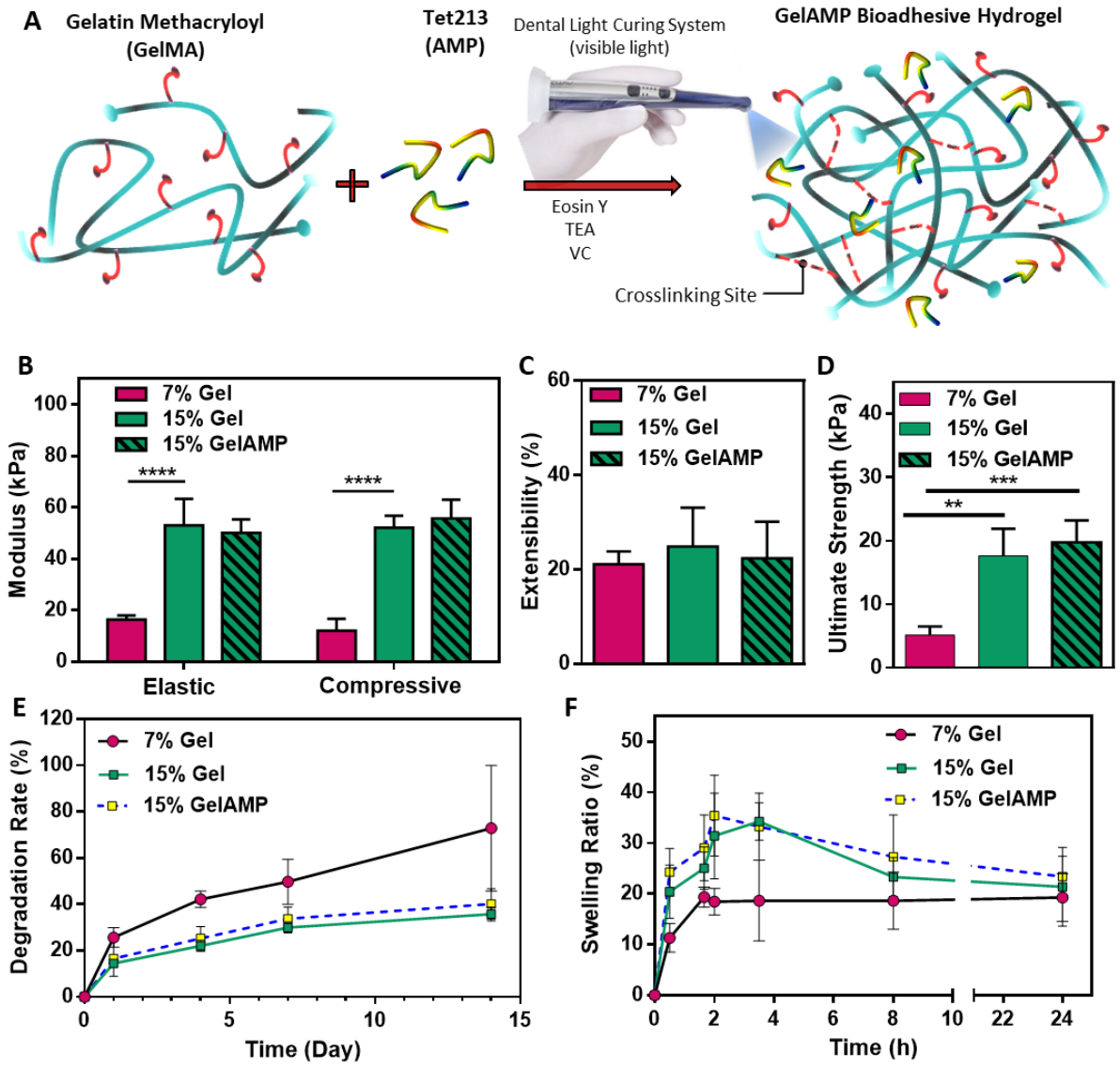

Figure 17. Physical characterization of bioadhesive hydrogels. (A) Synthesis and photocrosslinking process of bioadhesive hydrogels. **(B)** Elastic and Young's modulus, **(C)** extensibility, and **(D)** ultimate stress of the adhesive hydrogels produced by using 7% and 15% (w/v) total polymer concentration with and without AMP. **(E)** *In vitro* degradation properties and **(F)** swelling ratios in Dulbecco's phosphate buffered saline (DPBS) for 7% and 15% (w/v)

adhesive hydrogels with and without AMP. Data are represented as mean ± SD (*$p < 0.05$, **$p < 0.01$, ***$p < 0.001$, ****$p < 0.0001$ and $n \geq 5$).

To evaluate the physical properties of the bioadhesives, hydrogel formulations were synthesized based on two different concentrations of bioadhesive (7 and 15% (w/v)) with and without incorporation of AMP. Our results showed that 15% (w/v) bioadhesive hydrogels exhibited a 4.3-fold and 3.2-fold increase in the Young's and elastic moduli, respectively, when compared to 7% (w/v) hydrogels (**Fig. 17B**). In addition, the extensibility of the bioadhesives did not change by changing the concentration of bioadhesive from 7% to 15% (w/v) or by the addition of AMP (**Fig. 17C**). However, the ultimate tensile strength of hydrogels increased from 5.2 ± 1.3 kPa to 19.8 ± 3.5 kPa as the bioadhesive concentration was increased from 7% to 15% (w/v) (**Fig. 17D**). The results also showed that the addition of AMP did not alter the mechanical properties of the bioadhesives, which could be due to the low concentration and the small size of the AMP [104].

Next, we examined the *in vitro* stability of the bioadhesives by incubating them in DPBS for 14 days. Bioadhesives with 7% (w/v) concentration resulted in significantly accelerated degradation as compared to bioadhesives with 15% (w/v) concentration. In particular, the 7% (w/v) bioadhesive showed 72.8 ± 21.1% degradation by day 14 post-incubation, while 35.8 ± 3.0 % of the hydrogel with 15% (w/v) concentration was degraded during the same time (**Fig. 17E**).

We then determined the water uptake capacity of the hydrogels, by calculating the swelling ratios of the bioadhesives at different concentrations and time points. For this, the swelled weights of the samples after incubation at 37 °C in DPBS was divided by their corresponding dry weights. As shown in **Fig. 17F**, the swelling ratios of the hydrogels decreased by increasing bioadhesive concentrations. However, the swelling ratios barely changed after 10 h of incubation, indicated that the equilibrium states were achieved at this time point. In addition, the incorporation of AMP

did not alter the degradation rate and the swellability of the bioadhesives (**Fig. 17E, F**). Overall, bioadhesives with 15% (w/v) concentration showed higher mechanical stiffness and slower degradation rates as compared to 7% (w/v) hydrogels. Previous studies have also studied the effect of physical properties and microstructural features of hydrogel scaffolds on the regeneration and repair of target tissues [104, 265, 266]. An ideal bioadhesive used in the setting of the oral cavity should be elastic and flexible, as well as sufficiently strong to withstand breakage due to the intrinsic dynamism of the oral tissues [267]. For this purpose, the water uptake capacity of the bioadhesives should be finely tuned to prevent excessive swelling, which could lead to patient discomfort and detachment from the wet and highly motile oral tissues. Furthermore, fast degradation of the adhesive could compromise adequate retention and greatly limit their clinical efficacy [104]. Our results showed that, in addition to the higher modulus (**Fig. 17B**), and ultimate strength (**Fig. 17D**) of the 15% (w/v) bioadhesives, they also showed comparatively higher structural stability *in vitro*. This was demonstrated by their slower degradation rates (**Fig. 17E**) and similar swelling equilibrium states upon incubation in DPBS (**Fig. 17F**) when compared to 7% (w/v) bioadhesives. In the next step, we will evaluate the adhesive properties of the hydrogels to soft physiological tissues and hard implant surfaces.

Based on these results, the Young's modulus of the SN loaded adhesive hydrogels increases significantly when the concentration of the SN increases from 0 to 150 μg/ml, while it decreases at higher SN concentration (500 μg/ml) (Figure 20a). For tensile properties, the maximum elastic modulus was observed at 500 μg/ml SN concentration, while there was no statistical difference between the elastic modulus of the adhesives engineered with lower SN concentrations and the control (Figure 20b). In contrast with elastic modulus, the extensibility of the SN laden adhesives was minimum at 500 μg/ml SN concentration (Figure 20c).

To evaluate the effect of the SN incorporation on degradation properties of the adhesives, adhesive hydrogels containing different concentration of SN (0, 50, 100 and 500 μg/ml) were incubated in PBS for up to 14 days. The results revealed there was no significant effect on degradation of the GelMA adhesives after incorporation of SN.

In addition to physical characterization, other properties of the SN-laden adhesives need to be investigated. Therefore, we optimized the SN concentration and will study its effect on the osteogenic differentiation of 3D encapsulated hMSCs *in vitro*. The optimized formulation was then tested *in vivo* using a mouse calvaria model, mandibular bone defect in minipigs, and ligature induced PI model in minipigs to evaluate the osteoinductive properties of the SN-laden adhesives *in vivo*.

3.2.2.3. In vitro and ex vivo adhesive properties of the engineered hydrogels

The strong retention and adhesion of biomaterials to both the native tissue and the implant surface is a critical factor to promote periodontal tissue repair and regeneration [268]. Moreover, the designed bioadhesive must withstand the shear and the pressure exerted by the underlying tissues and the high motility of the oral tissues. To evaluate these parameters, we performed standard *in vitro* adhesion tests including wound closure (ASTM F2458-05), lap shear (ASTM F2255-05), and burst pressure (ASTM F2392-04) to assess the adhesiveness of the hydrogels to physiological tissues and titanium surfaces. Similar tests were also performed using a commercially available sealant, CoSEAL™, as control. Wound closure tests were performed to measure the adhesive strength of the bioadhesives to soft tissues including porcine gingiva (**Fig. 18A, B**) and porcine skin (**data is not shown**). The results of the wound closure tests revealed that the adhesive strength of the hydrogel to gingiva increased from 23.5 ± 5.4 kPa to 55.3 ± 6.7 kPa, by increasing the hydrogel concentration from 7 to 15% (w/v) (**Fig. 18B**). Similarly, the adhesive

strength of the bioadhesives to porcine skin was increased 2.1-fold by increasing the total polymer concentration from 7 to 15% (w/v) (**data is not shown**). Moreover, the presence of AMP did not alter the adhesion strength of the hydrogels for both porcine gingiva and skin (**Fig. 18B)**. Lastly, the adhesive strength of the 15% (w/v) bioadhesive was significantly higher than that of CoSEAL™, with a 3.3-fold difference for gingiva tissue and a 1.7-fold difference for skin tissue (**Fig. 18B**).

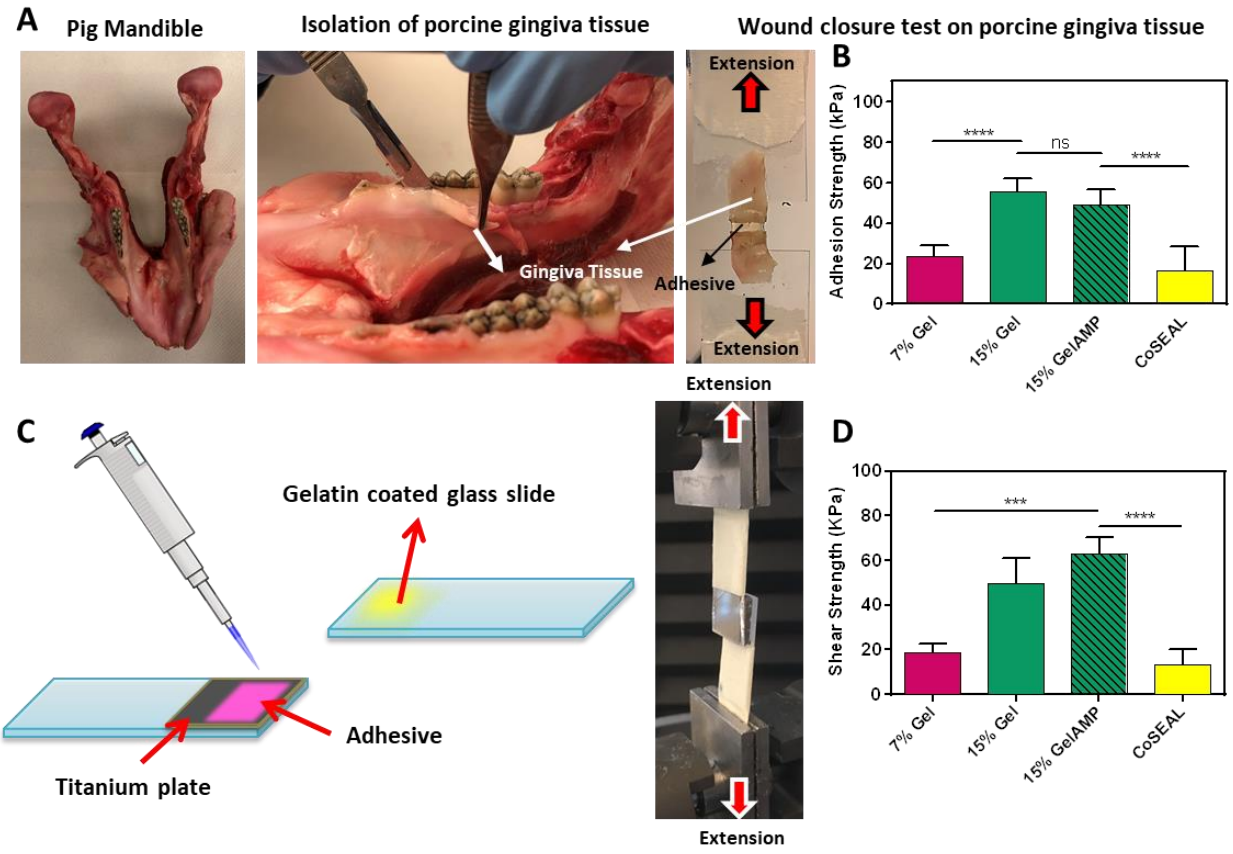

Figure 18. *In vitro* and *ex vivo* adhesion properties of GelAMP hydrogels. (A) Representative images of wound closure test using pig gingiva tissue based on ASTM standard test (F2458-05) and **(B)** adhesion strength of bioadhesive hydrogels and a commercially available adhesive (CoSEAL™) to porcine gingiva. **(C)** Schematic of the *in vitro* lap shear test based on a modified ASTM standard (F2255-05), using titanium as a substrate. **(D)** The *in vitro* lap shear strength of

the bioadhesive hydrogels at 7% and 15% polymer concentration and a commercially available adhesive (CoSEAL™). Data are represented as mean ± SD (**p < 0.01, ***p < 0.001, ****p < 0.0001, n=5).

Similar to the wound closure tests, 15% (w/v) bioadhesives, with and without AMP, showed significantly higher lap shear strength to titanium surface as compared to CoSEAL™ (i.e., 3.7 and 4.6-fold difference, respectively) (**Fig. 18D**). However, the lap shear strength did not significantly change for 15% (w/v) bioadhesives with and without AMP (**Fig. 18D**). In contrast, the burst pressure of the bioadhesives was increased from 17.0 ± 2.9 kPa at 7% (w/v) to 34.6 ± 4.0 kPa at 15% (w/v) final polymer concentration. Furthermore, the highest burst pressure was observed for 15% (w/v) hydrogels (37.7 ± 6.5 kPa), which was significantly higher than that of CoSEAL™ (1.7 ± 0.1 kPa) (**data is not shown**).

Different hydrogel adhesives have been used for sealing, reconnecting tissues, or as implant coatings [264, 268]. However, their poor mechanical properties and adhesion to wet tissues have limited their implementation in the clinic. Moreover, the majority of the commercially available dental adhesives are based on polymethyl methacrylate (PMMA) or acrylic based resins, which are mainly used as fillers for dentin cavities. Although these types of adhesives have shown strong adhesion and binding to the oral surfaces and tissues (i.e., gingiva and pulpal walls), their potential as a platform for the treatment of PIDs is limited [269, 270]. This is mainly due to the lack of cell-binding sites, and poor tissue biointegration, which ultimately limit the regenerative capacity of these resins [270]. In contrast, our results revealed that our visible light curable bioadhesives are able to bind strongly to both hard (titanium) and soft (gingiva) surfaces and withstand high shear stress and pressure. In addition, we have previously shown that gelatin-based bioadhesives can

strongly adhere to wet and dynamic tissues such as the lungs [118]. Therefore, these bioadhesives could be used to effectively adhere to periodontal tissues in the presence of blood and saliva, as well as under palatal pressure and during mastication. Moreover, due to the high regenerative capacity of ECM-derived biopolymers, gelatin-based bioadhesives could constitute a suitable alternative for the treatment of PIDs [104].

3.2.2.4. In vitro antimicrobial properties of adhesive hydrogels

AMPs are comprised of short sequences of cationic amino acids, which have been shown to possess broad spectrum bactericidal activity against G (+/-) bacteria [104, 271]. AMPs bind to the negatively charged outer leaflet of bacterial cell membranes, which leads to changes in bacterial surface electrostatics, increased membrane permeabilization, and cell lysis [104].

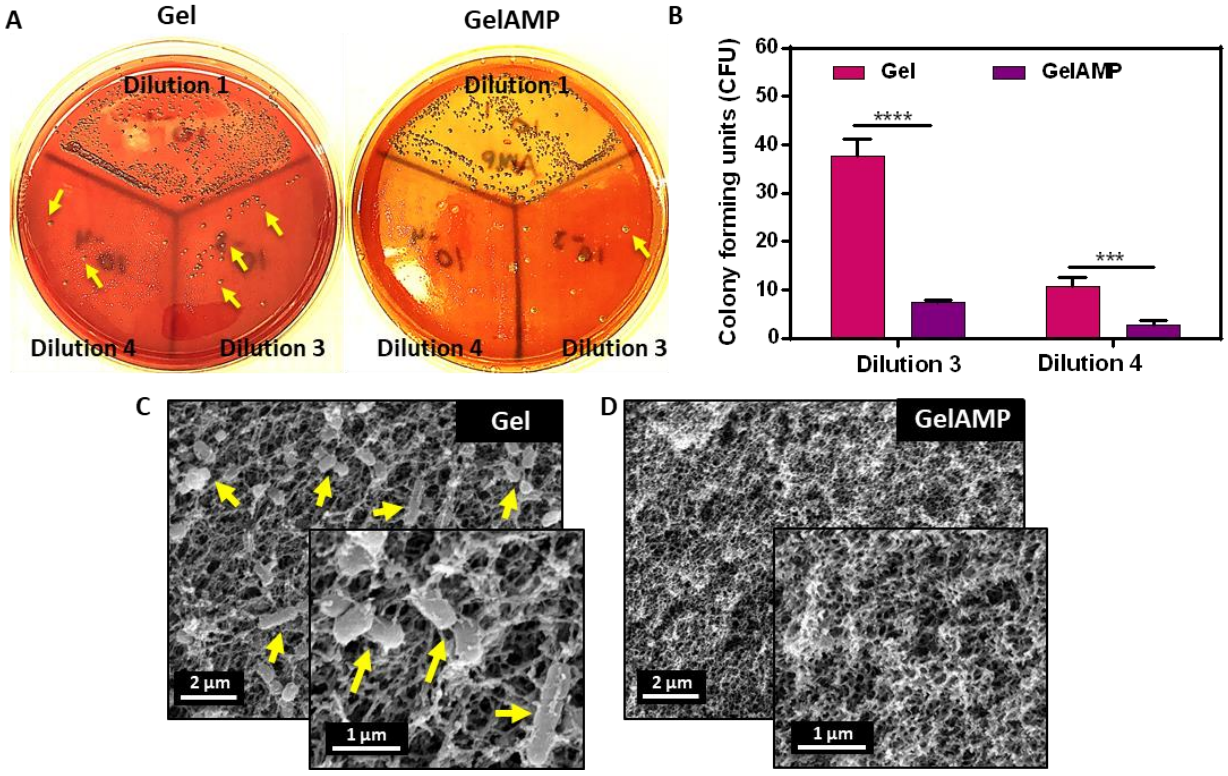

Figure 19. *In vitro* antibacterial properties of bioadhesive hydrogels against *p. gingivalis*. (A) Representative images of *p. gingivalis* colonies grew on blood agar plates for bioadhesives with and without AMP. **(B)** Quantification of colony forming units (CFUs) for bioadhesive hydrogels with and without AMP (0.2% (w/v)), seeded with *p. gingivalis bacteria* (day 4). Representative scanning electron microscope (SEM) images of *p. gingivalis* colonization on bioadhesive hydrogels containing **(C)** 0% and **(D)** 0.2% AMP. Clusters of bacteria are shown with yellow arrows. (***$p < 0.001$ and ****$p < 0.0001$).

Here, we synthesized GelAMP, a dental light curable bioadhesive with antimicrobial properties through the incorporation of AMP into bioadhesive hydrogels. Previously, we have shown that AMP tet213 at very low concentrations is effective against both G (+/-) bacteria [104]. Here, we used an optimized concentration of AMP in this work (0.2 %(w/v)) based on our previous study [104]. First, we evaluated the antimicrobial activity of the resulting bioadhesive against *P. gingivalis* using a standard colony forming units (CFU) assay and direct visualization of the bacteria-laden hydrogels via scanning electron microscope (SEM) (**Fig. 19**). The CFU assay showed that the number of *P. gingivalis* colonies in the 3-logarithmic dilution decreased from 37.7 ± 3.5 at 0.0% (w/v) AMP, to 10.6 ± 1.9 at 0.2% (w/v) AMP (**Fig. 19A, B**). A similar response was also observed for the 4-logarithmic dilution, which further confirmed the bactericidal properties of the engineered antimicrobial GelAMP bioadhesives, when compared to pristine hydrogels as controls (**Fig. 19B**). SEM micrographs also showed that the hydrogels without AMP exhibited significant bacterial infiltration and colonization throughout the polymer network (**Fig. 19C**). In contrast, GelAMP containing 0.2% (w/v) AMP, showed high antimicrobial activity as

demonstrated by the complete absence of bacterial clusters on both surface and cross sections of the bioadhesives (**Fig. 19D**).

A variety of AMPs such as defensins and cathelicidins are normally found in the oral cavity, particularly in the gingival crevicular fluid and in salivary secretions, and constitute the first line of defense against bacterial infection [272]. Moreover, AMPs do not trigger resistance mechanisms and play a key role in the regulation of microbial homeostasis and the progression of gingival and periodontal diseases [273]. Because of this, previous groups have explored the use of AMPs as active coatings for dental implants and other therapeutic strategies aimed at the prevention of bacterial infection [274-276]. However, AMPs are highly susceptible to proteolytic degradation by proteases secreted by bacteria and host cells and thus, efficient *in vivo* delivery of AMPs to the site of infection remains challenging. Thus, the engineered bioadhesives in this work could be used to protect AMPs from environmental degradation and to deliver physiologically relevant concentrations of AMPs for controlled periods of time.

2.1. C*ell studies*

An ideal bioadhesive not only must be cytocompatible but should also allow the attachment and proliferation of cells within the 3D microstructure to support biointegration and healing. Here, we assessed the ability of the engineered bioadhesives to support the attachment and proliferation of migratory cells from the bone stroma via 3D encapsulation of bone marrow stromal cells (**Fig. 7**). In addition, we evaluated the ability of the bioadhesives to support the growth and proliferation of migratory stromal cells via 3D encapsulation of freshly isolated calvarial bone sutures.

***In vitro* cytocompatibility and proliferation of 3D encapsulated cells within bioadhesive hydrogels:** First, we evaluated the viability, metabolic activity, and spreading of bone marrow mouse stromal cells (W-20-17 [277]) encapsulated within the adhesives using a live/dead and

PrestoBlue assays, and F-Actin/DAPI staining, respectively. Our results showed that cells encapsulated within the bioadhesives with and without AMP exhibited > 90% viability after 1, 3, and 5 days of culture (**Fig. 20A, B**). In addition, the incorporation of AMP, did not affect the viability of the encapsulated cells (**Fig. 20A, B**). Moreover, F-Actin/DAPI staining revealed that W-20-17 cells could attach and proliferate throughout the 3D network for Gel and GelAMP adhesives, up to 5 days of culture (**Fig. 20C**). Furthermore, the metabolic activity of cells in GelAMP hydrogels increased consistently from 2273 ± 66 RFUs at day 1 to 10041 ± 938 RFUs at day 5 of culture (**Fig. 20D**). In addition, there were no statistically significant differences between the metabolic activity of cells seeded on GelAMP and Gel adhesives (**Fig. 20D**).

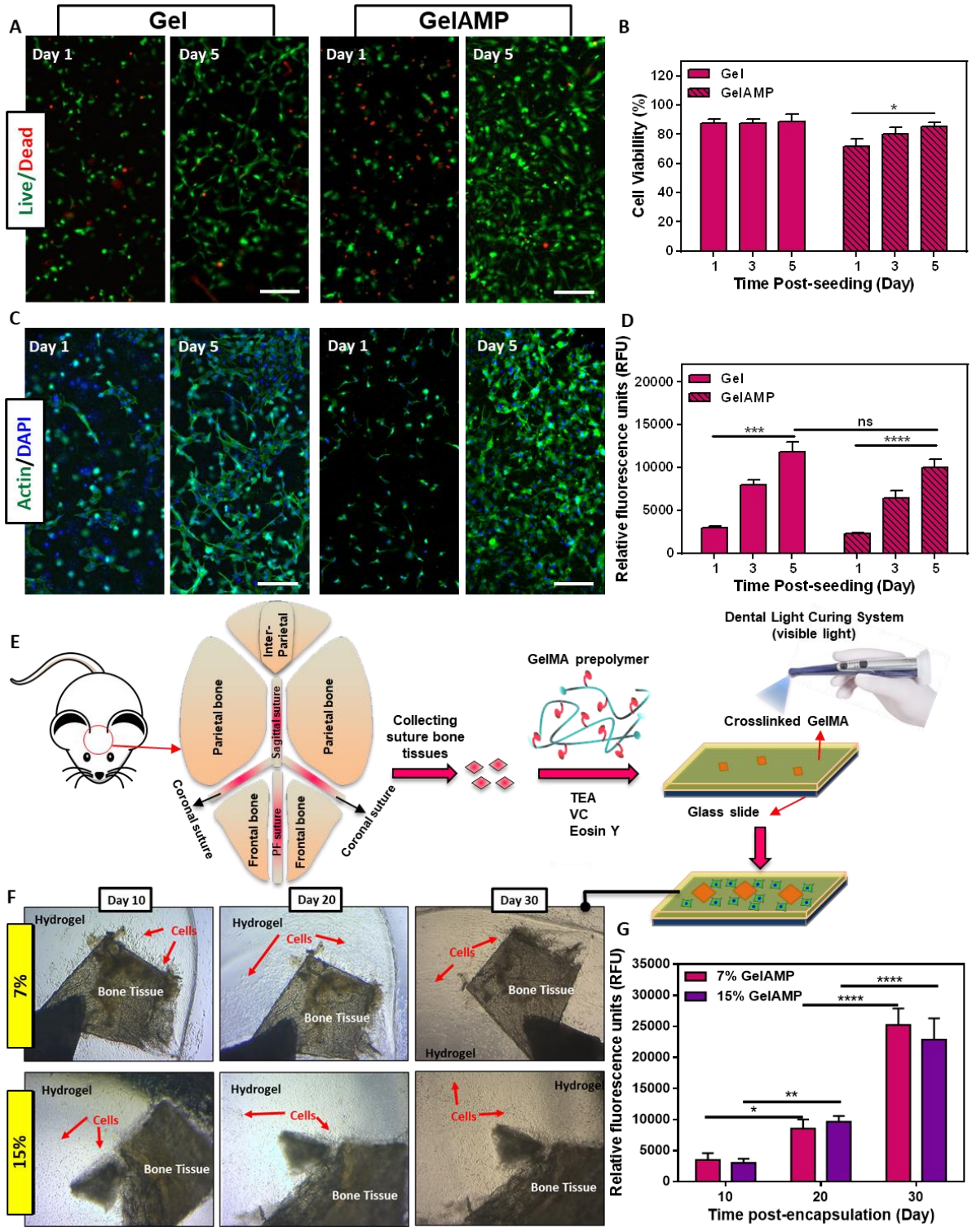

Figure 20. *In vitro* 3D encapsulation of W-20-17 cells and mouse calvarial bone sutures inside adhesive hydrogels. (A) Representative live/dead images of W-20-17 cells encapsulated within bioadhesives hydrogels with and without AMP after 1 and 5 days. **(B)** Quantification of viability

of W-20-17 cells incorporated within hydrogels without (control) and with AMP (GelAMP) using live/dead assays on days 1, 3, and 5 post encapsulation. **(C)** Representative phalloidin (green)/DAPI (blue) stained images of cell-laden bioadhesive with and without AMP after 1 and 5 days. **(D)** Quantification of metabolic activity of W-20-17 cells encapsulated in hydrogels after 1, 3, and 5 days. **(E)** Schematic diagram of the extraction and encapsulation of mouse calvarial bone sutures in 3D hydrogel network. **(F)** Representative images of calvarial bone sutures encapsulated within 7 % and 15% (w/v) bioadhesives to visualize growth and diffusion of cells at days 10, 20 and 30 post encapsulation. **(G)** Quantification of metabolic activity of migratory stromal cells from encapsulated bone sutures. Hydrogels were formed at 120 sec visible light exposure time (** $p < 0.01$, *** $p < 0.001$), **** $p < 0.0001$).

3D encapsulation of calvarial bone suture explants within bioadhesives: We encapsulated the freshly isolated calvarial bone sutures in both 7 and 15% (w/v) hydrogels to evaluate the ability of the bioadhesives to support the proliferation and migration of stromal cells (**Fig. 20E**). During the first week of encapsulation, no significant cell migration was observed. A week after encapsulation, cell (most likely suture-derived skeletal stem cells [278, 279]) deployment out of the suture was observed, followed by proliferation and migration within the bioadhesive hydrogel (**Fig. 20F**). The migratory and proliferative behavior of these cells were assessed for up to 30 days post-encapsulation (**Fig. 20F**). These results showed that the metabolic activity of the encapsulated cells increased consistently for both 7% and 15% (w/v) bioadhesives (**Fig. 20G**). For instance, the metabolic activity of the cells in 15% GelAMP (w/v) bioadhesives increased from 3016 ± 678 RFUs at day 10, to 22869 ± 3421 RFUs at day 30 post-encapsulation (**Fig. 20G**). However, we did not observe any statistical difference between metabolic activity of the cells seeded within the 7% and 15% (w/v) bioadhesive hydrogels (**Fig. 20G**).

Our results also indicated that the antimicrobial bioadhesives did not elicit any cytotoxic response and could effectively support the growth of both W-20-17 and suture-derive skeletal stem

cells *in vitro*. Previous studies have reported the development of different types of antimicrobial hydrogels based on the incorporation of metal or metal oxide nanoparticles [104, 280, 281]. However, the negative effect of metal oxide nanoparticles on cell viability greatly limit their application for the clinical management of PIDs [281]. In contrast, our results remonstrated that the cells could infiltrate and spread throughout our antimicrobial bioadhesives, while also remaining proliferative and metabolically active.

Taken together, these results demonstrated that our bioadhesives could be used to form an adhesive and antimicrobial barrier that prevents bacterial growth and supports the proliferation of bone-competent cells *in vitro*. The ability of the bioadhesives to eradicate or prevent infection at the implant site could not only be relevant to disinfect the affected area, but also to reduce inflammatory responses triggered by sustained microbial colonization. Moreover, the establishment of a cell-supportive microenvironment could promote the regeneration of the affected bone by endogenous progenitor cells that migrate into the wound site. Therefore, we next aimed to evaluate the ability of the bioadhesives to support bone regeneration *in vivo* using a calvarial defect model in mice.

3.2.2.5. In vivo evaluation of implanted hydrogels

We investigated the ability of the hydrogels to be delivered and formed *in situ* and to remain firmly attached to the wound area without the risk of displacement during the healing process. For this, we first created critically sized defects in mice calvaria using dental drills. The bioadhesive precursor solutions (7% and 15% (w/v)) were directly injected into the bone defects and photopolymerized using a commercial dental light curing unit (**Fig. 21A**). Our results showed that the bioadhesives could remain at the site of application without any sign of displacement after 7 and 14 days of implantation (**Fig. 21B**). In addition, histological assessment (hematoxylin and

eosin (H&E)) showed the complete sealing of the defect and a strong coherence between the biopolymer and the native bone following application (**Fig. 21C**). Moreover, the H&E images also revealed that bioadhesives with both formulations (7, and 15% (w/v)) could remain attached to the wound site up to 42 days after application (**Fig. 21D, E**). At earlier time points (14 days post application), the formation of new autologous bone could be observed near the margin of the original defect (**data is not shown**). Calvarial defects in untreated control animals showed limited new bone formation at day 42 post application (**Fig. 21F**). In contrast, histological staining revealed the formation of new bone for both 7% and 15% (w/v) bioadhesives (**Fig. 21D, E**). Furthermore, the area covered by the newly formed bone was significantly larger for defects treated with 15% (w/v) hydrogels as compared to 7% (w/v) hydrogels (**data is not shown**). This observation could be explained in part due to the increased structural integrity of bioadhesives with higher polymer concentration, which provided a more structurally stable scaffold to support bone regeneration and the ingrowth of the adjacent connective tissues (**Fig. 21E)**. These observations provided qualitative evidence that was indicative of the formation of new bone and the subsequent repair of the defect.

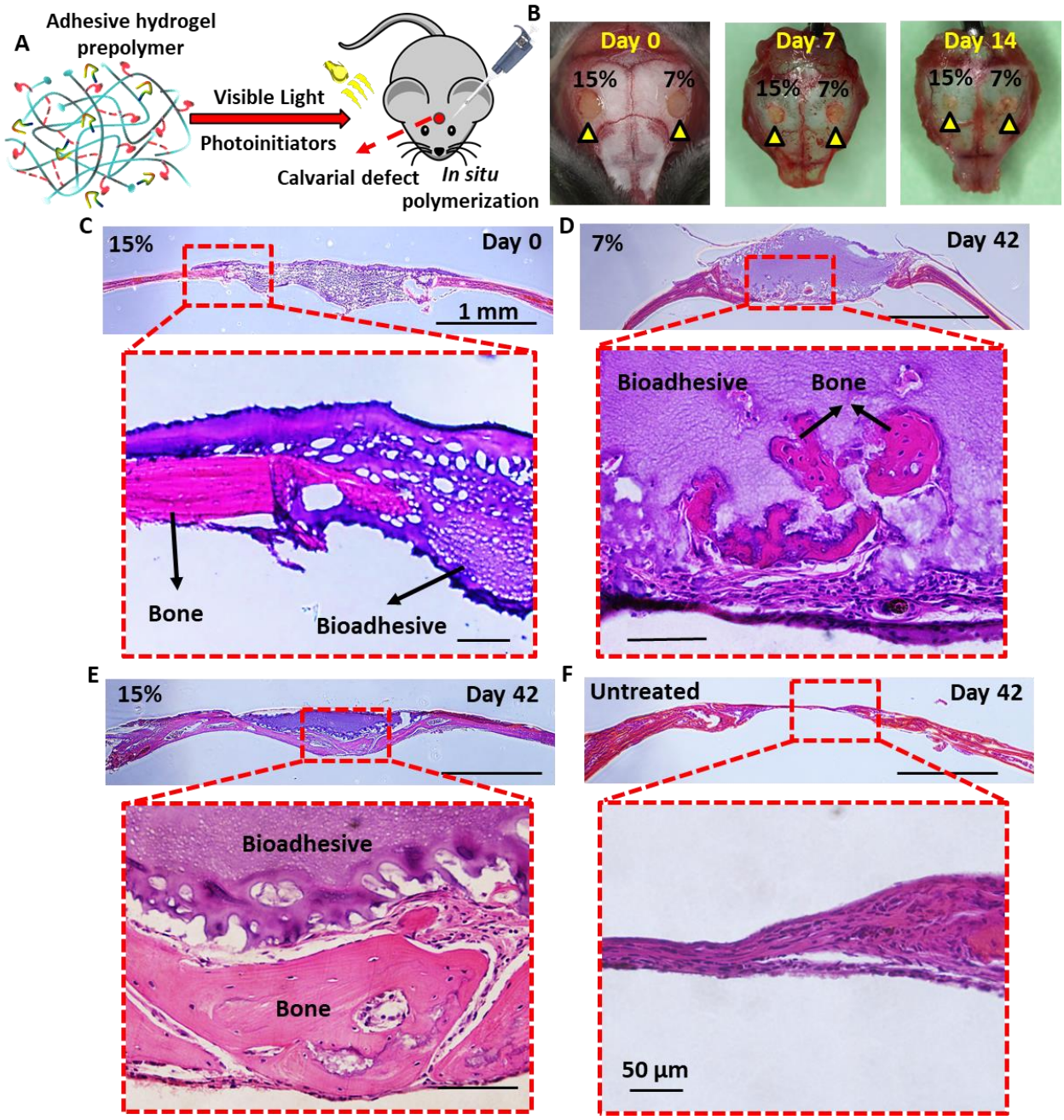

Figure 21. *In vivo* evaluation of bioadhesive hydrogels using a mouse calvarial defect model. **(A)** Schematic diagram of *in situ* application of bioadhesive hydrogels in a mouse calvarial defect model. **(B)** 7% and 15% bioadhesive hydrogels were delivered to artificially created bone defects in mouse calvaria (yellow arrowheads), and photopolymerized for 1 min using a commercially

available dental curing light. 7 and 14 days after implantation, samples remained in place, without any sign of detachment. **(C)** Histological evaluation (H&E staining) of the 15% (w/v) bioadhesives at day 0 post implantation. Representative H&E images for **(D)** 7% (w/v) and **(E)** 15% (w/v) bioadhesive treatment, and **(F)** untreated sample after 42 days post implantation.

To perform a quantitative evaluation of new bone formation, micro-computed tomography (μCT) was performed on untreated defects, as well as defects treated with bioadhesive synthesized using 7 and 15% (w/v) polymer concentrations at days 0, 28, and 42 post-procedure (**Fig. 22)**. Our results showed that the untreated defects exhibited limited evidence of bone forming up to 28- and 42 days post-procedure, with little decrease in the extension of the critical size (**Fig. 22A)**. At day 28, the defects treated with the 15% (w/v) hydrogels showed significantly higher bone formation than 7% (w/v) hydrogels and the untreated controls. At day 42, a significant amount of new bone was observed for defects treated with 15% (w/v) hydrogels (**Fig. 22A**). In addition, on days 28 and 42, the bone surface area (BS) and the bone volume (BV) for 15% (w/v) hydrogels were shown to be significantly higher than that of untreated and 7% (w/v) groups (**Fig. 22B, C**). For instance, at day 42, the BS for 15% (w/v) hydrogels corresponded to 2.96 ± 0.46 mm^2, which was significantly higher than the untreated controls (i.e., 1.03 ± 0.63 mm^2) and 7% (w/v) hydrogels (i.e., 1.40 ± 0.53 mm^2) (**Fig. 22B**). Moreover, the highest BV was observed for 15% (w/v) bioadhesives (i.e., 7.16 ± 1.65 mm^3), which was significantly higher than those of untreated (i.e., 2.76 ± 1.03 mm^3) and 7% (w/v) bioadhesives (i.e., 4.45 ± 0.72 mm^3) (**Fig. 22C**). Statistical analysis indicated that both the concentration of the biopolymer and the treatment time had a significant effect on BV and BS. For instance, the BS and BV increased 1.27 and 1.66-fold respectively, at 28- and 42 days post-

procedure, which was indicative of sustained bone regeneration throughout the experiment (**Fig. 22B, C**).

The higher degree of bone regeneration observed for 15% (w/v) bioadhesive could be due in part to the direct contribution of the enhanced mechanical properties of hydrogels with higher polymer concentrations [266]. For instance, Huebsch *et al.* demonstrated that the contribution of matrix elasticity to new bone formation *in vivo* is highly correlated with mechanically induced osteogenesis [266]. They reported that the BV and mineral density obtained for hydrogels with elasticities in the range of 60 kPa was significantly higher than those with 5 kPa or 120 kPa moduli [266]. In our study, 15% (w/v) bioadhesives, which exhibited elastic and Young's modulus corresponding to 53.0 ± 10.3 kPa and 52.2 ± 4.7 kPa (**Fig. 17B**), respectively, could potentially enable mechanically induced osteogenesis and thus, promote the formation of new bone *in vivo*. However, the clinical efficacy of antimicrobial bioadhesives for the treatment of patients with advanced PI could be limited due to the lack of a bona fide osteoinductive strategy. Although previous groups have reported the development of regenerative bioadhesives, they often rely on the use of growth factors [282, 283], stem cells [266, 284], and other bioactive molecules [285, 286]. These methods often suffer from clinical limitations and drawbacks [254-256]. Due to these limitations, in our future work we will introduce a cell/growth factor-free strategy by the incorporation of alternative osteoinductive strategies such as nanosilicates [261, 287] into antimicrobial bioadhesives which could constitute an attractive platform for the development of osteoinductive and antimicrobial bioadhesives for the treatment of PIDs.

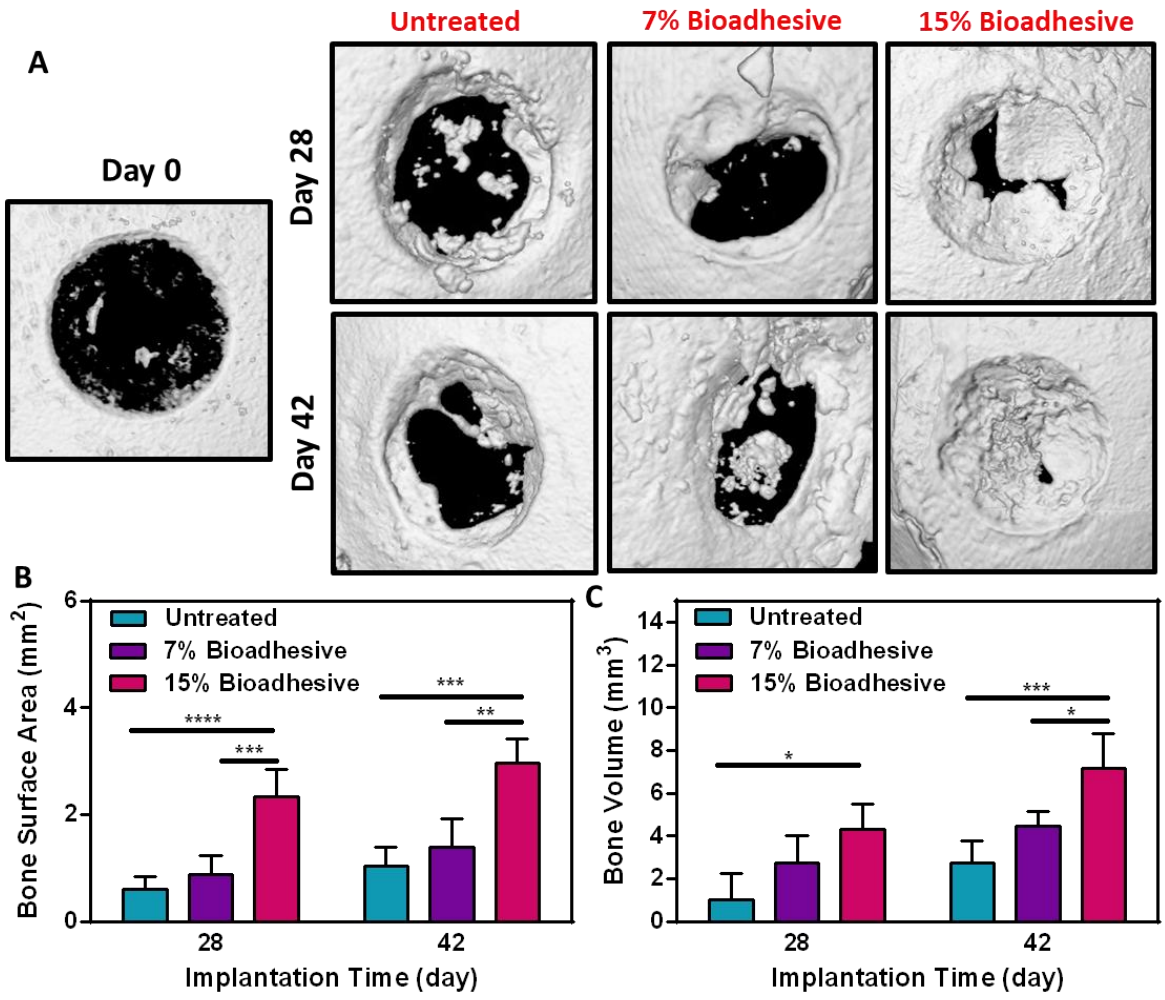

Figure 22. Quantitative evaluation of new bone formation using µCT analysis. (A) Representative micro-CT images for untreated defect, and defects treated with 7% and 15% bioadhesives on days 28 and 42 post-implantation **(B)** Quantitative analysis of bone surface area and **(C)** and bone volume. Data are represented as mean ± SD (*p < 0.1, **p < 0.01, ***p < 0.001, ****p < 0.0001, n=5).

3.3. Engineering an osteoinductive and antimicrobial bioadhesive hydrogels for treatment of peri-implantitis and periodontal bone defects

As described earlier, guided bone regeneration (GBR) techniques, which rely on compartmentalized tissue healing (CTH([257, 258], are utilized for re-osseointegration of implants affected by PI. Several biomaterials have been proposed to increase the regenerative efficacy of GBR [288-290]. However, GBR remains technically challenging, with large variability in terms of success rate [291-294]. Autologous bone grafts are the most effective approach to increase the success rate of GBR [288]. Nevertheless, due to the morbidity associated with them [295], bone allografts and xenografts, as well as alloplastic grafts have been used as substitutes, albeit with limited success [288, 295]. For example, there are some bone graft products such as Bio-OSS®, DynaBlast®, INFUSE®, PROGENIX®, Grafton DBM and MinerOss in the market, but none of them is specifically designed for treatment of PI, nor has antimicrobial properties. Most of the trials that tested more complex and expensive therapies did not show any statistically or clinically significant advantages over deep mechanical cleaning [296]. INFUSE®, a commercially available product for bone regeneration, based on combination of human recombinant bone morphogenetic protein 2 (hrBMP2) and collagen, has also been proposed for implant re-osseointegration [254]. Yet, the uncontrolled release rate of the growth factor [52] and the potentially harmful side effects (e.g. cancer) associated with hrBMP2 [255, 256] severely limit its application in PI treatment. Thus, the development of approaches based on the use different growth factors or alternative osteoinductive agents to regenerate the bone around implants are highly desired. Currently, there are no commercial products that combine high adhesion to soft and hard oral tissues, and antimicrobial and osteoinductive properties; therefore, clinical management of PI remains challenging. In this section, our goal was to engineer osteoinductive and antimicrobial adhesive hydrogels that: **1)** can be rapidly photocrosslinked *in situ* using dental curing lights, **2)** are able to strongly adhere to soft/hard oral tissues, as well as implant surfaces in the presence of

blood and saliva, **3)** exhibit potent antimicrobial activity, and **4)** can induce bone regeneration. To achieve this goal, we incorporated osteoinductive silicate nanoparticles (SNs) (laponite XLG) in GelAMP (GelMA-AMP) adhesive hydrogels (**Fig. 23**).

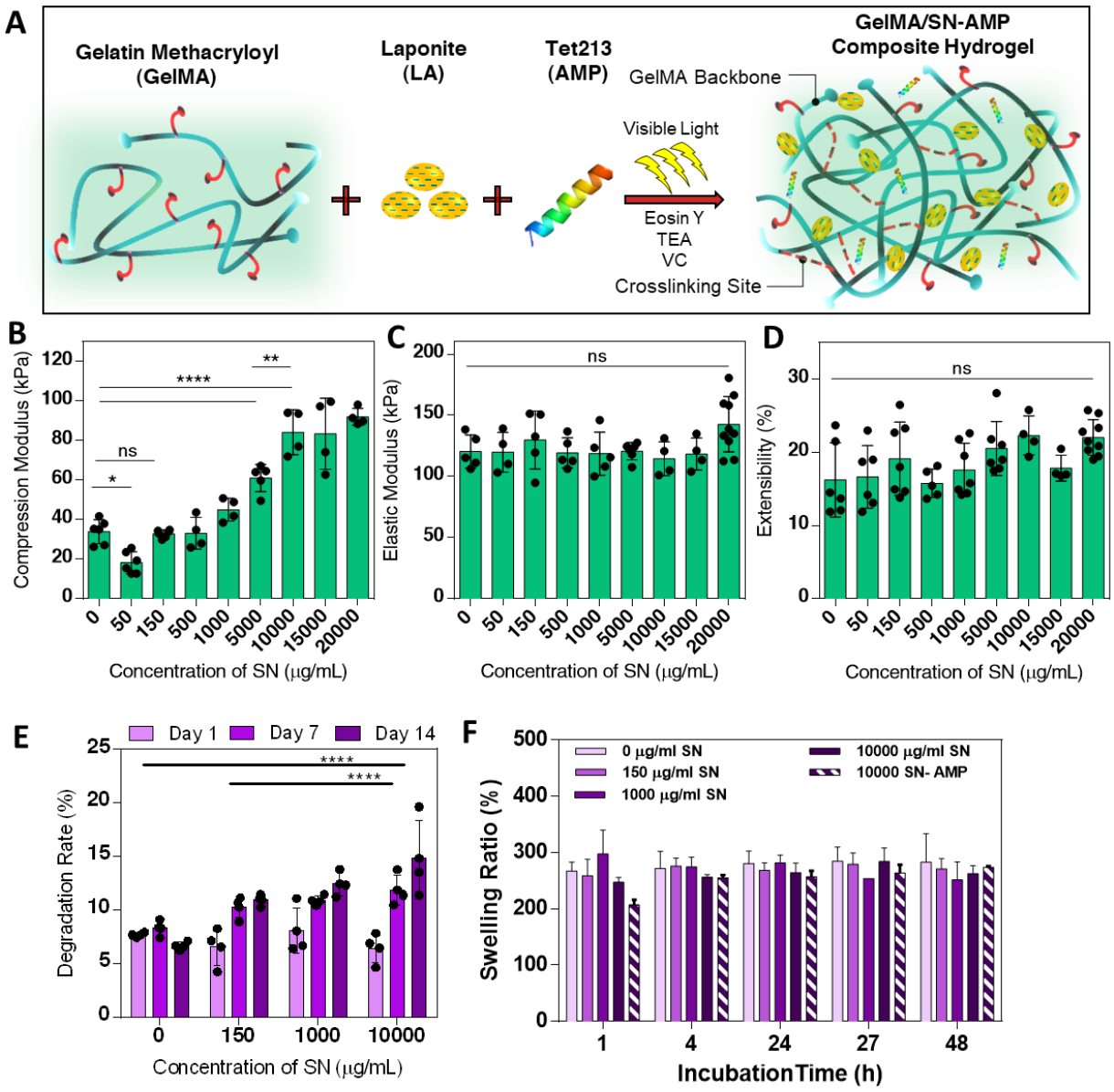

Figure 23. Physical characterization of bioadhesive hydrogels. (A) Synthesis and photocrosslinking process of bioadhesive hydrogels. **(B)** Young's and **(C)** Elastic modulus, and **(D)** extensibility of the adhesive hydrogels produced by using 15% (w/v) total polymer concentration and different SN content. **(E)** *In vitro* degradation properties and **(F)** swelling ratios

in Dulbecco's phosphate buffered saline (DPBS) for 7% and 15% (w/v) adhesive hydrogels with and without AMP. Data are represented as mean ± SD (*$p < 0.05$, **$p < 0.01$, ***$p < 0.001$, ****$p < 0.0001$ and $n \geq 5$).

3.3.1. Physical characterization of composite bioadhesive hydrogels

Next, we characterized physical properties of a library of bioadhesive hydrogels formed by using different concentrations of AMP and SN to optimize mechanical strength and adhesion properties of the hydrogels. The results showed that the maximum Young's modulus was observed for the adhesive hydrogels containing 10000 µg/ml SN **(Fig. 23B)**. However, the elastic modulus and extensibility of the hydrogels did not alter by changing SN concentration **(Fig. 23C-D)**. We also performed in vitro degradation test, where the adhesive hydrogels showed containing higher SN content showed significantly higher degradation rate as compared to hydrogels without SN **(Fig. 23D)**. Moreover, the swelling test indicated no significant difference in the water uptake capacity of the hydrogels. We also performed standard Wound Closure Test (**Fig 24A**), and Lap Shear Test (**Fig 24B**) to measure the adhesive strength of the bioadhesives. Based on the wound closure test, the bioadhesives containing 10000 µg/ml SN showed significantly higher adhesive strength to porcine gingiva, as compared to hydrogels without SN. In addition, the results of the lap shear tests showed that the adhesive strength of the bioadhesive hydrogels to titanium surfaces increased from 49.6 ± 11.6 kPa to 99.8 ± 18.5 kPa by increasing the SN concentration from 0 to 10000 µg/ml and both the adhesion strength and the lap shear strength of the bioadhesive were significantly higher than Coseal®) (**Fig 24A-B**). Our results also confirmed that the addition of AMP has no effect on the mechanical or adhesive properties of the hydrogels.

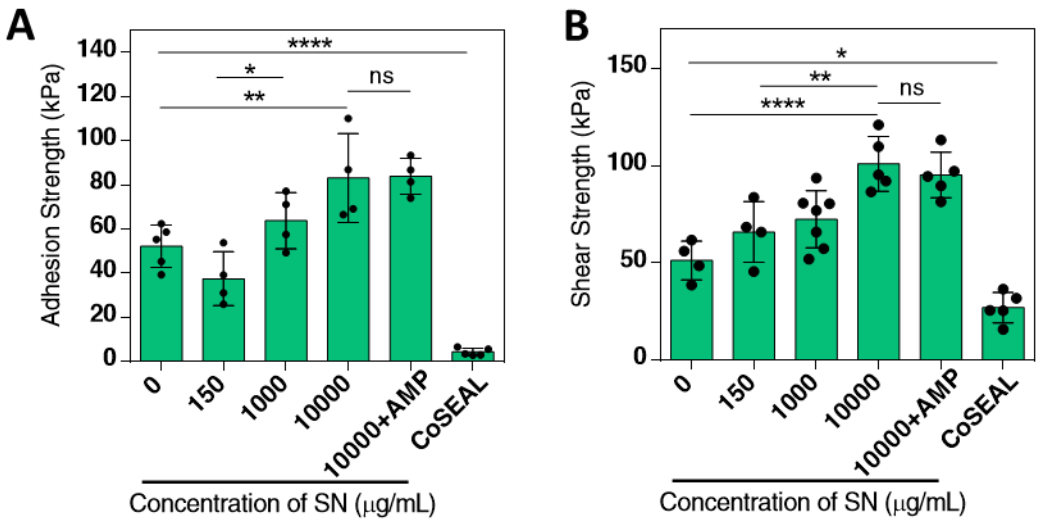

Figure 24. *In vitro* and *ex vivo* adhesion properties of adhesives hydrogels. (A) Adhesion strength of bioadhesive hydrogels and a commercially available adhesive (CoSEAL™) to porcine gingiva based on ASTM standard wound closure test (F2458-05). **(B)** The *in vitro* lap shear strength of the bioadhesive hydrogels and a commercially available adhesive (CoSEAL™) on titanium substrate, based on a modified ASTM standard (F2255-05). Data are represented as mean ± SD (**p < 0.01, ***p < 0.001, ****p < 0.0001, n=5).

3.3.2. In vitro antimicrobial properties of composite bioadhesive hydrogels

In addition, we evaluated the antimicrobial activity of AMP using different anaerobic and aerobic bacteria (G+/-). First, we evaluated the antimicrobial activity of the resulting bioadhesive against *P. gingivalis* using standard optical density (OD) growth test, and colony forming units (CFU) assay (**Fig. 25**). The OD test revealed that the optical density of the samples containing 0.4% (w/v) AMP, as well as AMP solution (same concentration) decreased significantly overtime as compared to the samples without or with lower concentration of AMP, as well as sulfamethoxazole/trimethoprim (SMZ-TMP) antibiotic as control (**Fig. 25A**). The CFU assay

showed that the number of *P. gingivalis* colonies in the 3-logarithmic dilution decreased significantly at 0.4% (w/v) AMP, as compared to 0, 0.1, and 0.2% (w/v) AMP (**Fig. 19A, B**). A similar response was also observed for the 4-logarithmic dilution (**Fig. 19B**). In addition, we have examined the antimicrobial activity of the hydrogels against three different aerobic bacteria (G+/-), including multidrug resistant (MDR) e. coli, MRSA and staphylococcus aureus (**Fig. 25 D-F)**. The results demonstrated that the samples containing 0.4% AMP showed the highest antimicrobial activity against all three bacteria, as compared to GelMA/SN and pristine GelMA hydrogels (**Fig. 25 D-F)**.

A

	0	6 h	24 h	36 h	48 h	60 h
Bacteria Solution	0.644	0.029	0.126	0.128	0.105	0.105
AMP solution 0.1% (w/v)	0.678	-0.121	0.009	-0.064	-0.077	-0.077
AMP solution 0.4% (w/v)	0.714	-0.106	0.023	-0.093	-0.104	-0.104
Antibiotic (SMZ-TMP)	0.751	-0.023	0.125	0.019	0.017	0.017
Adhesive (1000 SN-0% AMP)	0.616	-0.053	0.171	0.044	0.248	0.248
Adhesive (1000 SN-0.4% AMP)	0.719	-0.08	0.056	-0.053	-0.032	-0.032

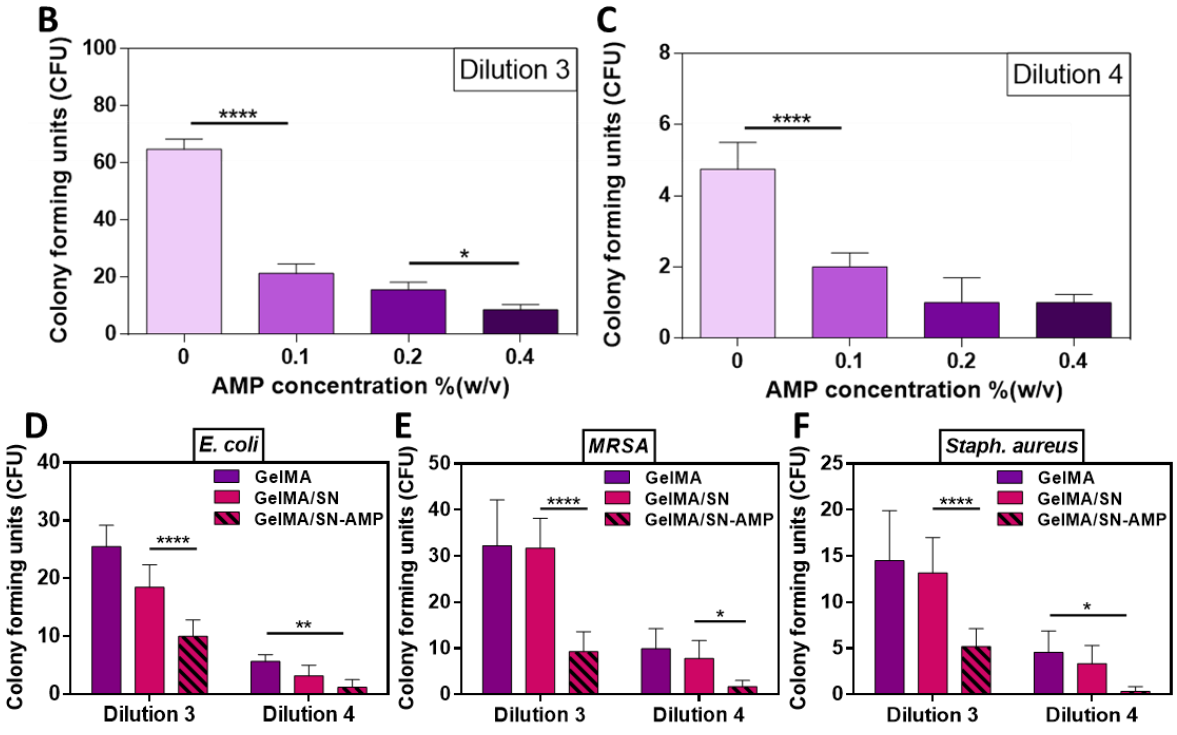

Figure 25. ***In vitro*** **antibacterial properties of bioadhesive hydrogels against different**

aerobic/anerobic and G+/- bacteria. (A) Quantification optical density (OD) growth of *p. gingivalis* bacteria cultured in different solutions with and without AMP, and a commercial antibiotic (SMZ-TMP) as control. **(B)** Quantification of colony forming units (CFUs) for bioadhesive hydrogels with and without AMP (0, o.1, 0.2, and 0.4 % (w/v)), seeded with *p. gingivalis bacteria* (day 4). Quantification of colony forming units for bioadhesive hydrogels with and without AMP (0.4 % (w/v)), seeded with **(C)** *MDR e. coli*, **(D)** *MRSA* and **(E)** *staphylococcus aureus*. (*p < 0.05, **p < 0.01 and ****p < 0.0001).

3.3.3. In vitro cytocompatibility and differentiation studies

In this section, different *in vitro* assays were used to evaluate hMSCs viability, proliferation, and differentiation. According to live/dead assay, cell viability was >90% for all the samples for up to 5 days post seeding (**Fig. 26a-h, m)**. In addition, hMSCs were able to spread on the surface of the hydrogels based on Actin/DAPI staining (**Fig. 26i-l)**. Moreover, the cell metabolic activity, measured by PrestoBlue assay, increased consistently for all the samples over time (**Fig. 26n)**.

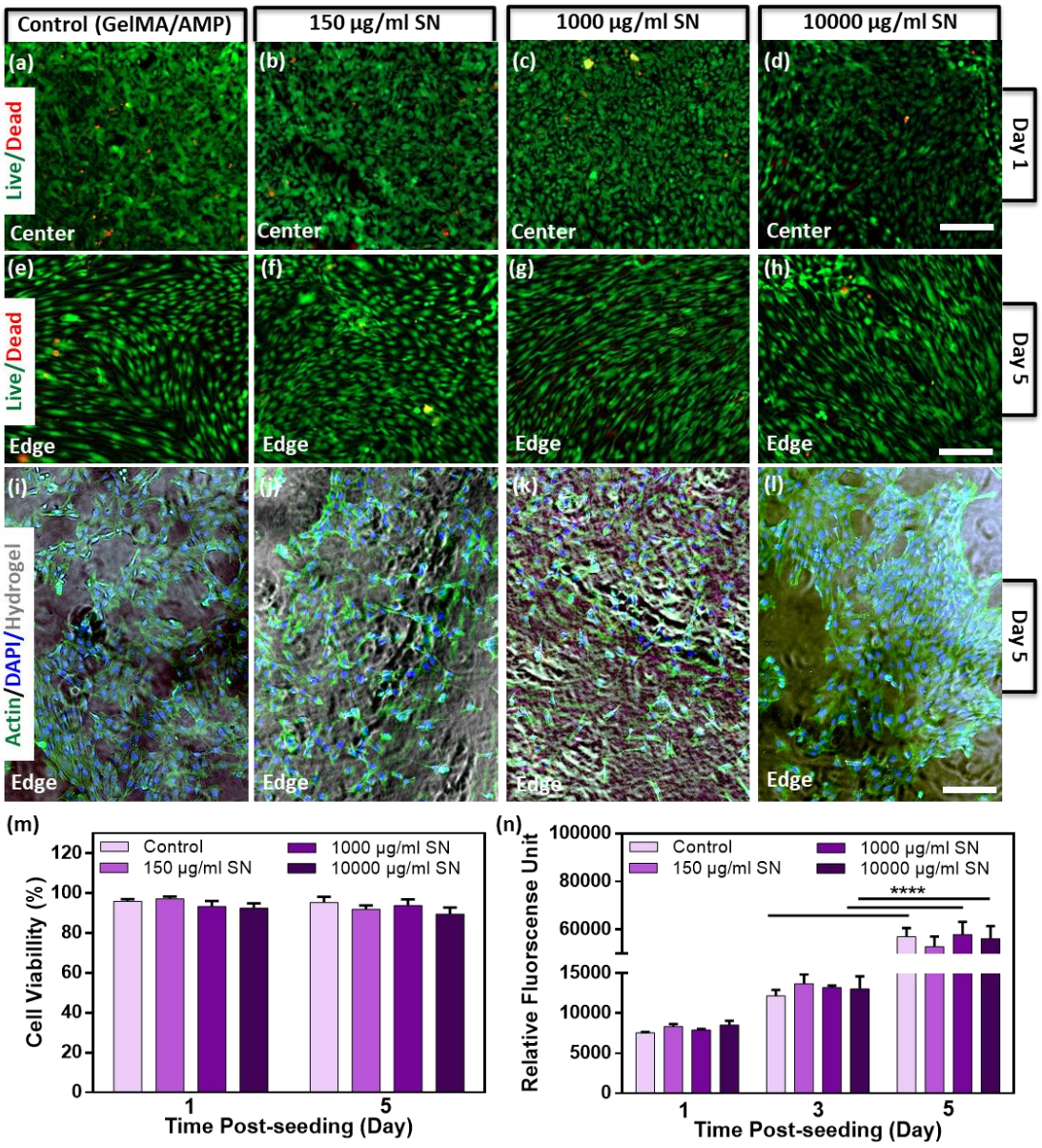

Figure 26. ***In vitro*** **cytocompatibility and proliferation of hMSCs. (A)** Representative live/dead images of hMSCs cells seeded on the surface of antimicrobial bioadhesive hydrogels with different SN content after 1 and 5 days. **(B)** Representative phalloidin (green)/DAPI (blue) stained images of cells seeded on bioadhesives after 1 and 5 days. **(C)** Quantification of viability of cells seeded on the hydrogels using live/dead assays on days 1, 3, and 5 post encapsulation. **(D)** Quantification of metabolic activity of hMSCs seeded on the surface of hydrogels after 1, 3, and 5 days.

Next, we evaluated the osteogenic differentiation of hMSCs seeded on the surface of the hydrogels with and without SNs. Two control groups were used: well-plate with and without Bio-OSS bone graft. The results indicated that the hMSCs seeded on bioadhesive hydrogels showed the highest viability, adhesion and spreading after 15 days as compared to control groups (**Fig. 27A**). In addition, the results showed higher chondrogenic differentiation of hMSCs seeded on bioadhesives containing SNs after 15 days of culture (**Fig. 27B**). The Alizarin staining also showed higher calcium deposition, indication higher osteogenic differentiation of hMSCs seeded on bioadhesives containing SNs after 7 and 15 days of culture as compared to other groups (**Fig. 27C**). Representative images of Von Kossa staining for hMSCs seeded on the surface of bioadhesive hydrogels containing AMP, with SNs showed higher phosphate deposition, indication higher osteogenic differentiation of hMSCs seeded on bioadhesives containing SNs after 7 and 15 days of culture as compared to other groups (**Fig. 27D**).

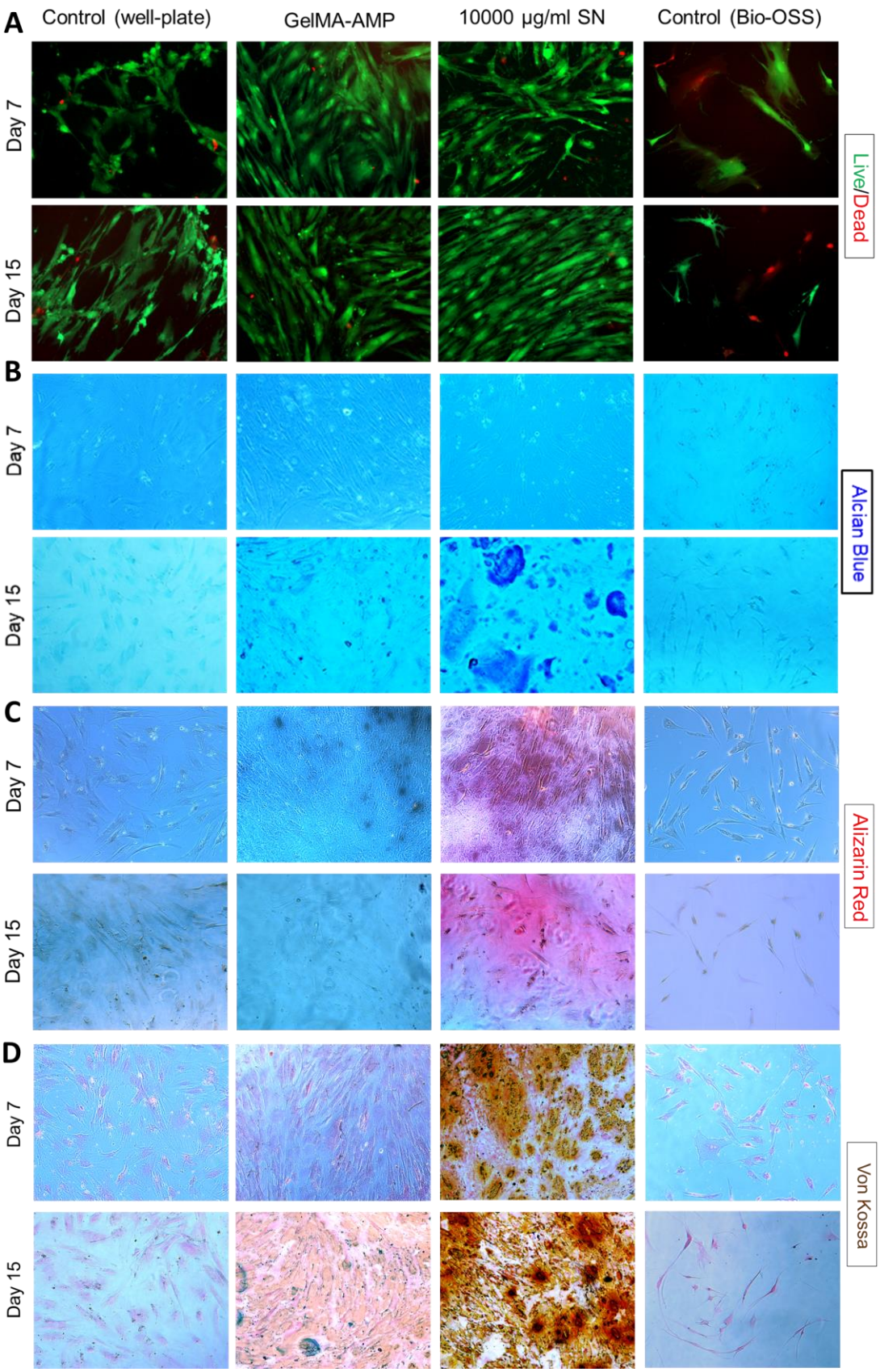
A
Control (well-plate)
GelMA-AMP
10000 µg/ml SN
Control (Bio-OSS)
Day 7
Day 15
Live/Dead
B
Day 7
Day 15
Alcian Blue
C
Day 7
Day 15
Alizarin Red
D
Day 7
Day 15
Von Kossa

Figure 27. *In vitro* cytocompatibility and osteogenic differentiation of hMSCs. (A) Representative fluorescent images of calcian AM (green: live) and ethidium homodimer I (red: dead) for hMSCs seeded on the surface of well-plate (control), bioadhesive hydrogels containing AMP, with and without SNs, and Bio-OSS bone graft after 7 and 15 days. Representative images of **(B)** Alcian Blue, **(C)** Alizarin Red, and **(D)** Von Kossa staining for hMSCs seeded on the surface of well-plate (control), bioadhesive hydrogels containing AMP, with and without SNs, and Bio-OSS bone graft after 7 and 15 days.

3.3.4. In vivo biocompatibility and biodegradation of composite bioadhesives

In order to assess biocompatibility and biodegradation of bioadhesive hydrogels, we used a rat subcutaneous implantation model (as described before). The results of subcutaneous implantation showed that the implanted bioadhesives (both formulations with and without SN) could be efficiently biodegraded in a period of time that allowed the growth of new autologous tissue after 56 days post implantation (**Fig. 28A**). In addition, the bioadhesives elicited minimal inflammatory responses against macrophages (CD68) and the lymphocytes (CD3) up to 56 days post implantation (**Fig. 28B,C**).

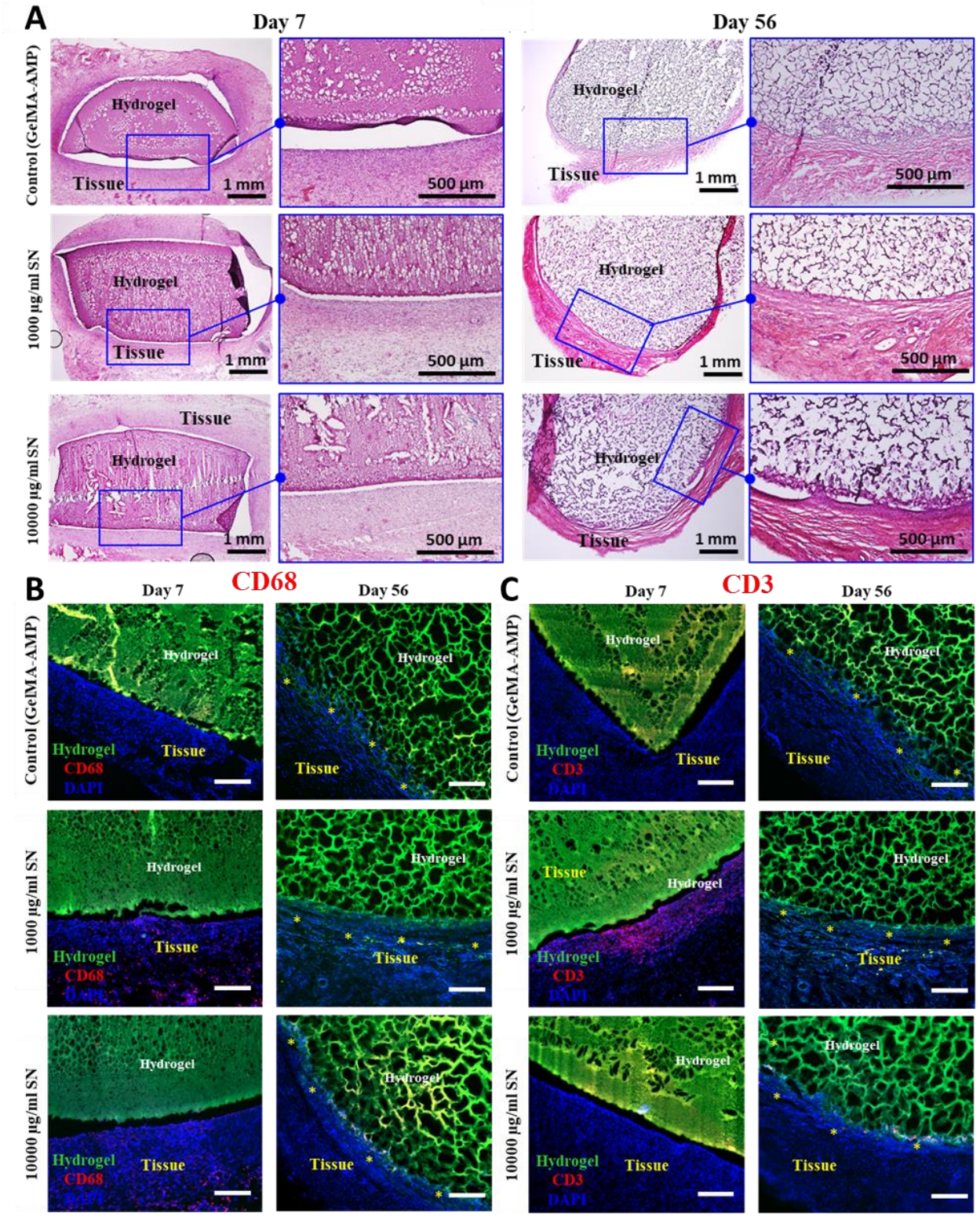

Figure 28. ***In vivo*** **biocompatibility and biodegradation of hydrogels in a rat subcutaneous implantation model. (A)** Representative H&E, and immunohistochemical images for **(B)** CD68

marker for detection of macrophages and **(C)** CD3 marker for detection of T cells (lymphocytes) for bioadhesives containing 0, 1000, and 10000 µg/ml SN for up to 56 days after subcutaneous implantation in rats.

3.3.5. In vivo bone forming capacity of composite bioadhesives

Next, we have tested the bone forming capability of our adhesive hydrogel containing AMP and SN in a large mandibular bone defect model in miniature pigs (**Fig 29**). We used commercial bone graft Bio-OSS as a control. The defect treated with Bio-OSS bone graft showed high bone density at day 0 (**Fig 29A**). This is mainly due to radiopaque nature of Bio-OSS granules. After 60 days, the new bone formed on the surface of Bio-Oss and bridged the particles, (**Fig 29B**), which is similar to previous reports [297, 298]. In contrast, the adhesive hydrogels were radiolucent at day 0, while appeared to show extensive new bone formation and complete bone filling the defect after 60 days (**Fig 29A-B**). In addition, unlike Bio-OSS granules, bioadhesive precursor could readily fill the holes in the defect site due to the injectable nature of the prepolymer solution. There are also some reports on limited bioresorption of Bio-OSS *in vivo*, where the Bio-OSS remnants could be detected in the bone defect after long term implantation (>44 months) [299].

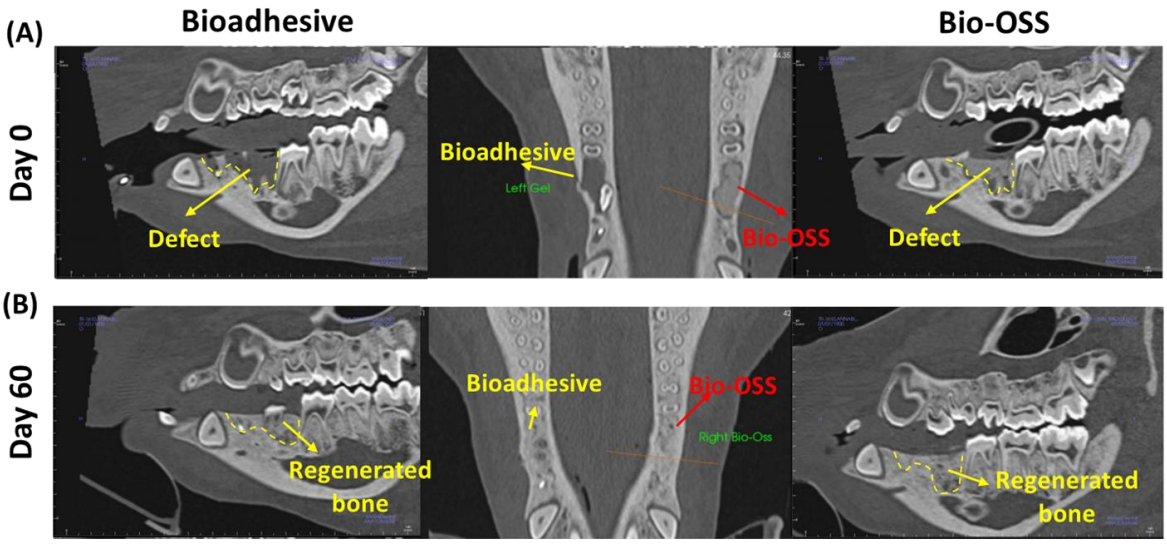

Figure 29. ***In vivo*** **evaluation of the bioadhesive hydrogels in a critical sized mandibular bone defect model miniature pig model.** The representative CT images for bioadhesive hydrogels and Bio-OSS bone graft after application in a large defect in miniature pig mandible at **(A)** day 0 and **(B)** 60 post application.

3.3.6. In vivo of composite bioadhesives in a ligature induced peri-implantitis model in miniature pigs

In order to evaluate the efficacy of bioadhesive hydrogels, we first developed a ligature induced peri-implantitis model in miniature pigs and then used our composite bioadhesives for treatment of the PI associated bone defects (**Fig. 30)**.

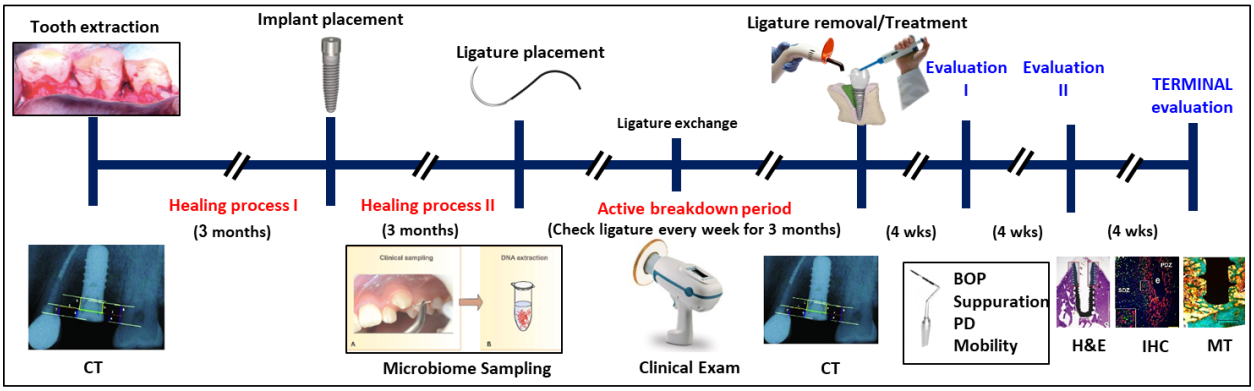

Fig 30. Outline of the study to test the efficacy of the adhesives for PI treatment in a minipig model.

To develop the PI model, we used three miniature pigs (Yucatan breed, males), 12 months of age with an average body weight of approximately 65 kg was utilized. In the first step, three premolar teeth from each side of the jaw was removed (**Fig. 31A)**. Two months after teeth extraction, new tooth growth was observed in the defect sites (**Fig. 31B)**. Three months after the bilateral removal of the premolars, two titanium implants per side was inserted into each animal (4 implants/animal) (**Fig. 32A-B)**. Three months after the insertion of the implants, PI was induced by placing a ligature around the neck of the implants, allowing for the undisturbed accumulation of plaque and calculus around the implants (**Fig. 33)**. Ligatures were checked weekly and were replaced every 4 week and then left in place for a total of 3 months. During a breakdown period of 3 months, PI was developed as a significant bone loss was occurred around the dental implants (**Fig. 34)**.

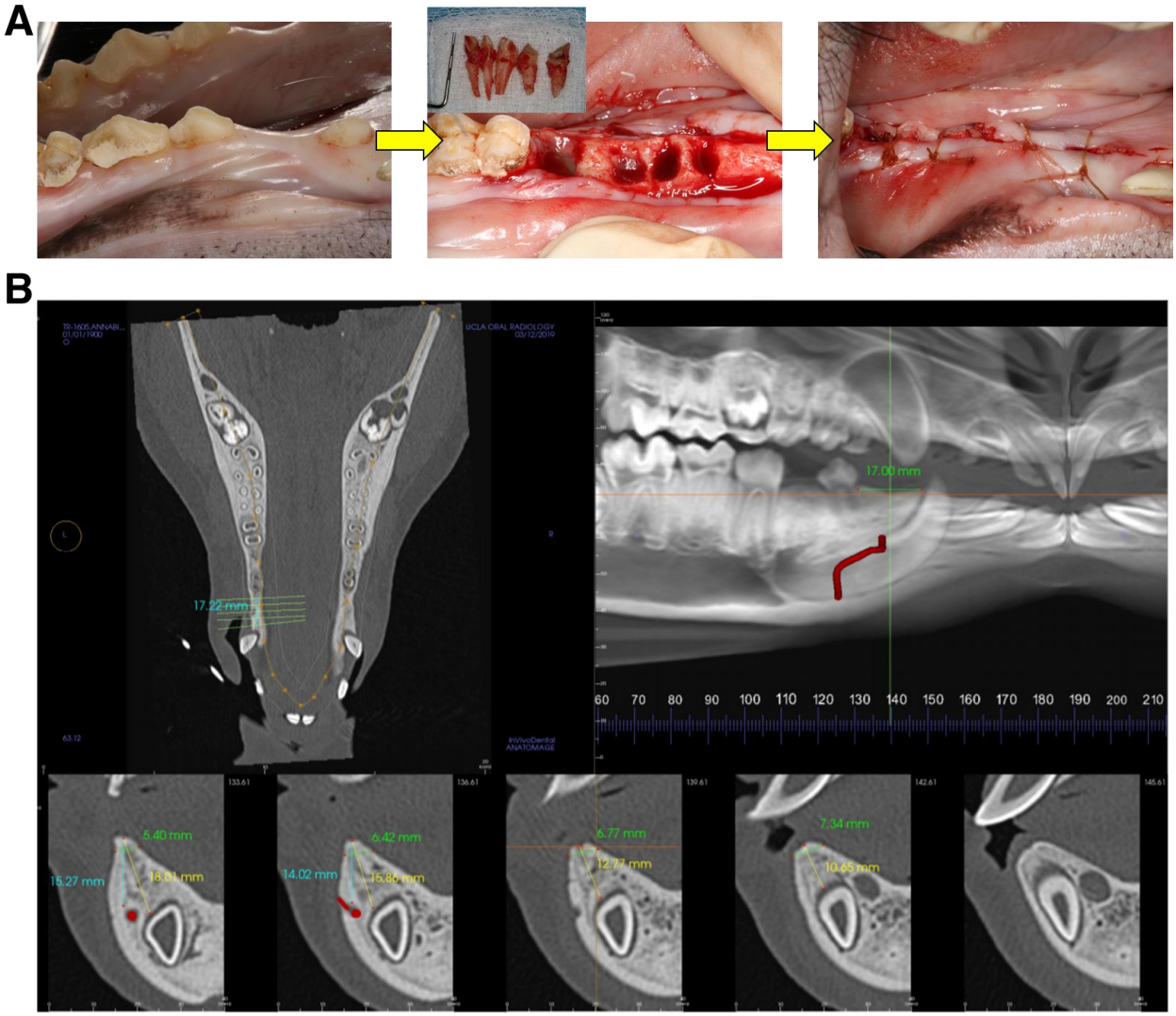

Figure 31. (A) Representative images of tooth extraction process and closure of the wound in miniature pigs. **(B)** Representative CT images of the pig mandible, showing the area related to extracted teeth after 2 months healing. A tooth regrowth was observed in one defect site.

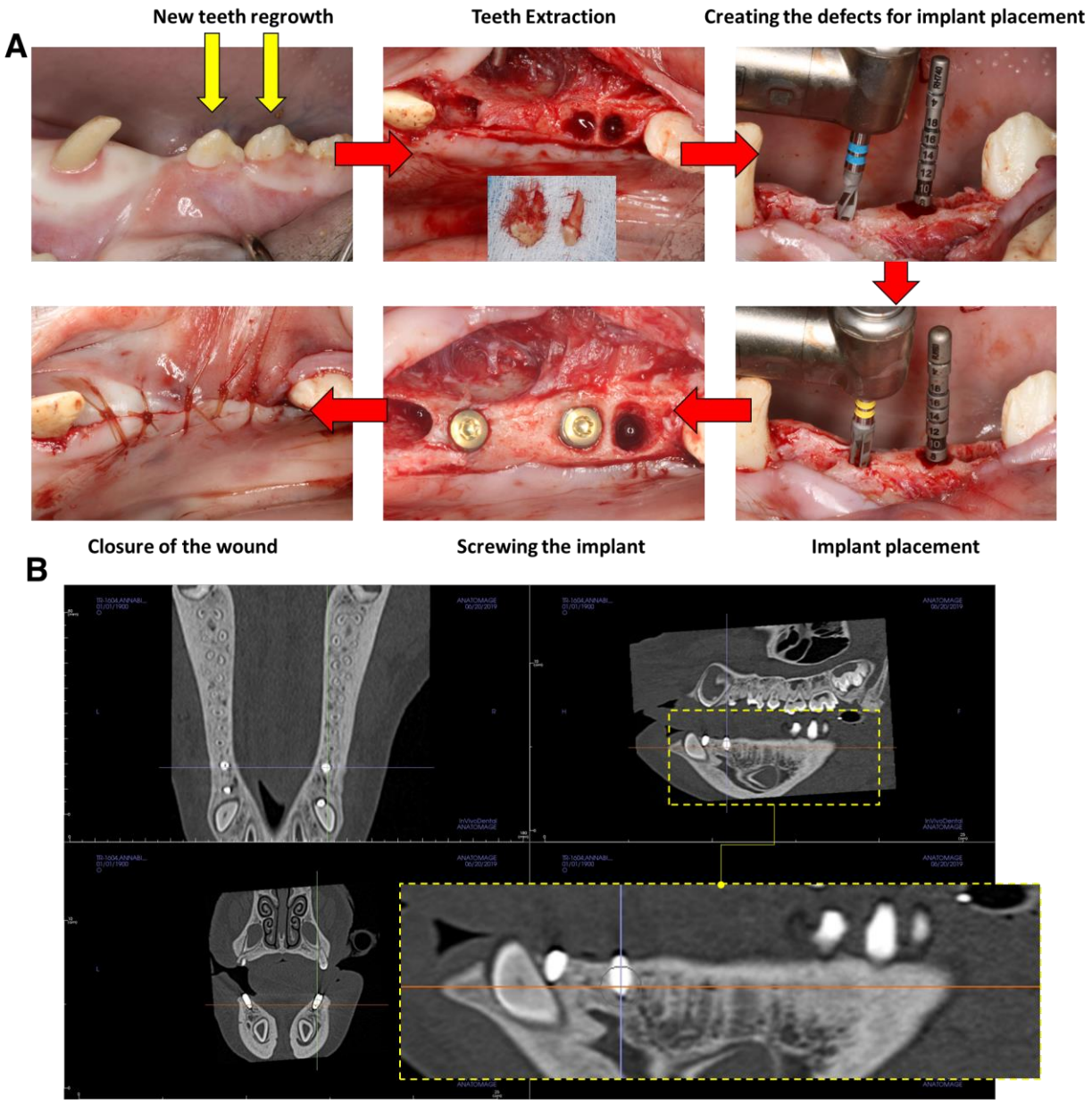

Figure 32. (A) Representative images of secondary tooth extraction process, implant placement, and closure of the wound in miniature pigs. **(B)** Representative CT images of the pig mandible, showing the implants after 2 months healing (two months after implant placement).

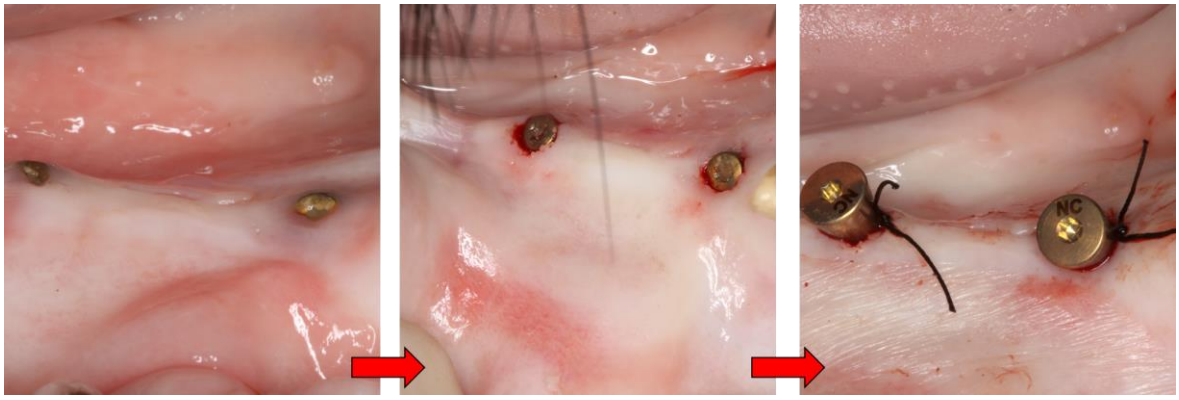

Figure 33. Representative images of ligature and implant abutment placement in miniature pigs, two months after implant placement. Two silk ligatures were used per implant to induce peri-implantitis through bacterial accumulation.

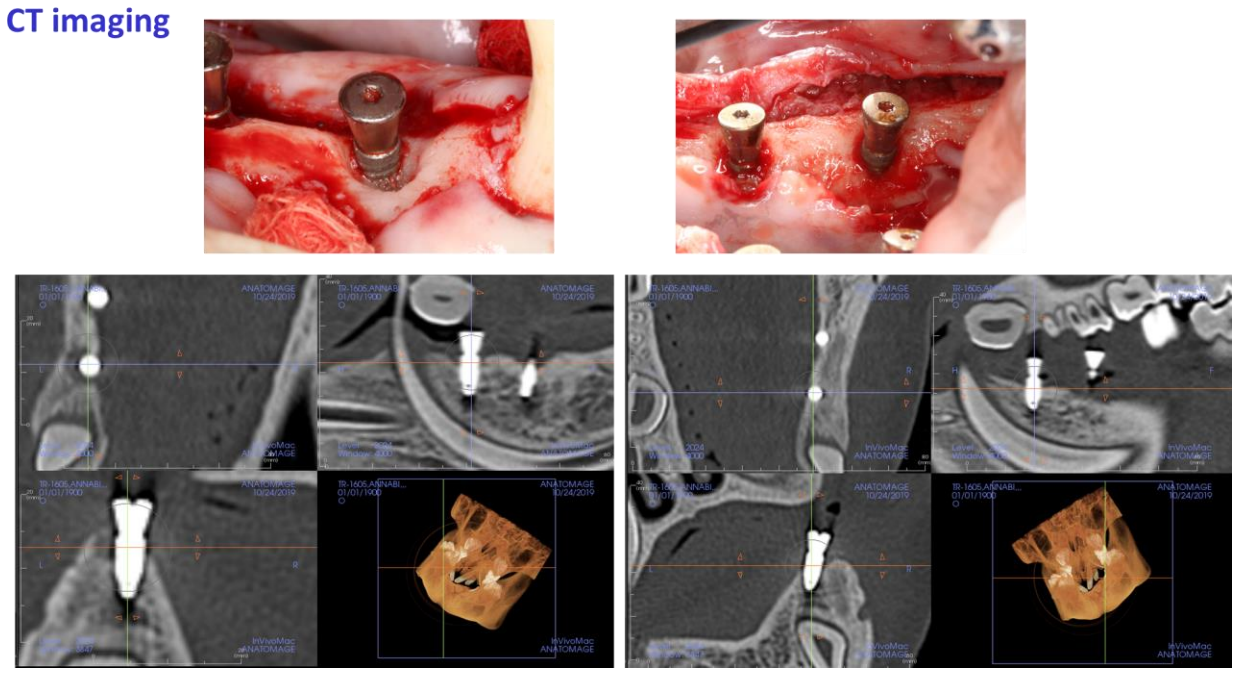

Figure 34. Representative photographic and CT images of the implants 3 months after ligature placement. A significant bone loss was observed around the implants.

Then treatments were initiated, and evaluations were performed after 4 and 12 weeks. The following treatments were tested: **1)** mechanical debridement without treatment; **2)** PI treated with mechanical debridement + GelMA-AMP-SNs; 3**)** PI treated with mechanical debridement + Dynablast (commercial bone graft). After surgical exposure of the PI defects and mechanical debridement, hydrogel treatment (~500 µl) was pipetted to fill the peri-implant defects. Then the precursor was polymerized *in situ* with a VALO® LED curing light for 2 min (**Fig. 35** and **Fig. 36)**. Similarly, for Dynablast bone graft, the material was transferred to the defect site by using a sterile spatula (**Fig. 36)**.

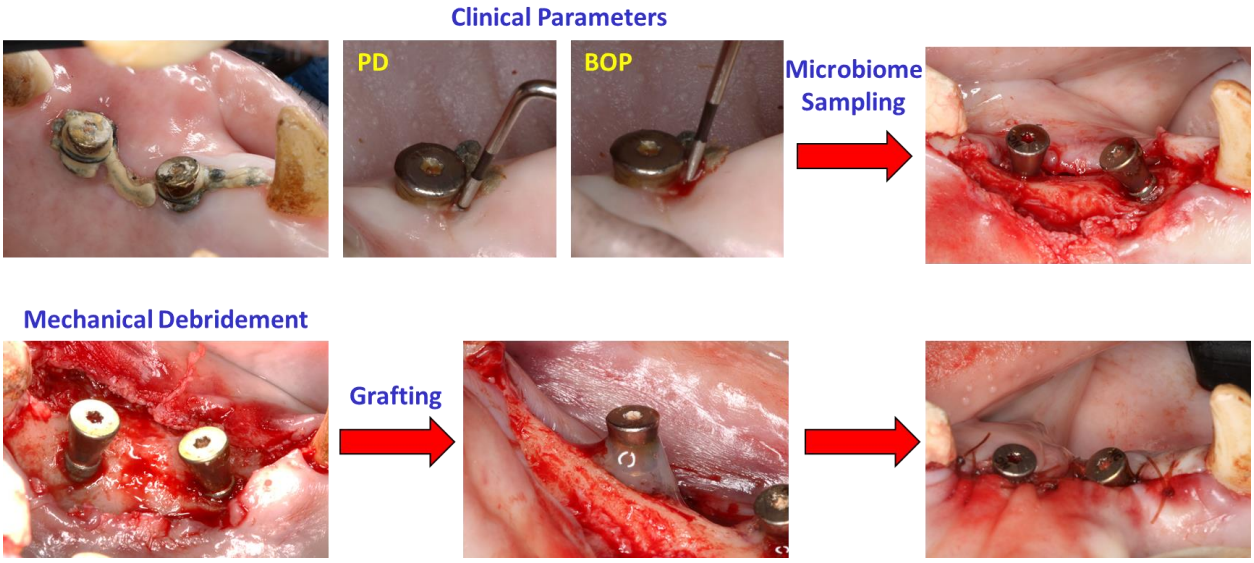

Fig. 35. Representative images of implants with ligature and high plaque index, measurement of clinical parameters, mechanical debridement process, grafting with bioadhesive hydrogels, and closure of the wound in miniature pigs.

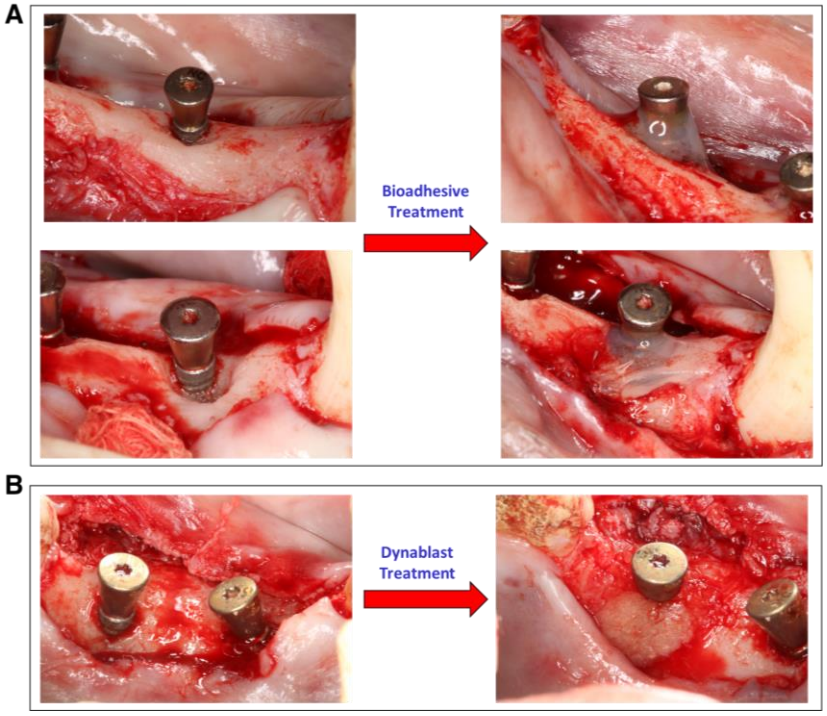

Figure 36. Representative images of peri-implant defects after treatment with **(A)** bioadhesive hydrogels and **(B)** Dynablast, a commercial bone graft as control.

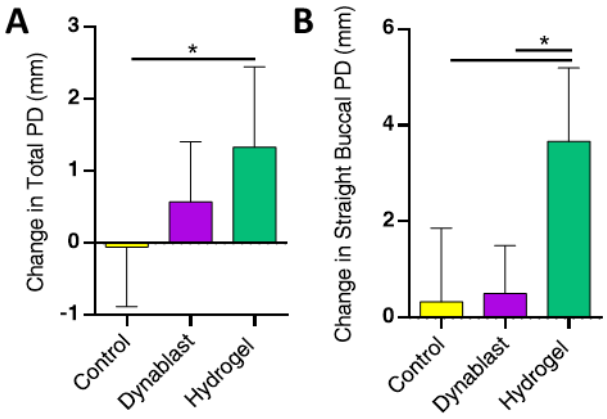

Figure 37. Peri-implant prosthetic parameters. **(A)** Total changes in and **(B)** change in straight buccal changes probing pocket depth (PD) values for the implants treated with bioadhesive hydrogels, and Dynablast and untreated controls. Data are represented as mean ± SD (*$p < 0.05$, $n \geq 3$).

A significant bone loss was observed around the implants after one week and also one month (no significant bone regeneration) for the control group. The prosthetic parameters were measured before and after treatment. The data showed a significant decrease in total and straight buccal probing pocket depth (PD) for the implants treated with bioadhesive hydrogels as compared to untreated group and the defects treated with Dynablast (**Fig. 37A-B**).

In addition, a significant bone regeneration around the implant was observed after 3 months in the distal side of the implant (height decreased from 2.48 to 1.53 mm). In addition, the height of lingual bone slightly decreased (3.45 to 3.34 mm) (**Fig. 38B**). **Figure 38A** shows the micro-CT images for the bone defects treated with bioadhesive hydrogels, and Dynablast and untreated controls. The quantification of bone morphological parameters and trabecular analysis were performed for all the samples. Based on the results, the bone volume fraction (BV/TV) in the region of interest for the samples treated with bioadhesive hydrogels were significantly higher than those treated with Dynablast and untreated control (**Fig. 38C**). This clearly shows the higher bone regenerative capability of bioadhesive hydrogels even compared to a commercial bone graft (Dynablast). Bone surface density (BS/BV) was also calculated for all the samples. However, there was no statistical difference between bone surface density in all the samples (**Fig. 38D**).

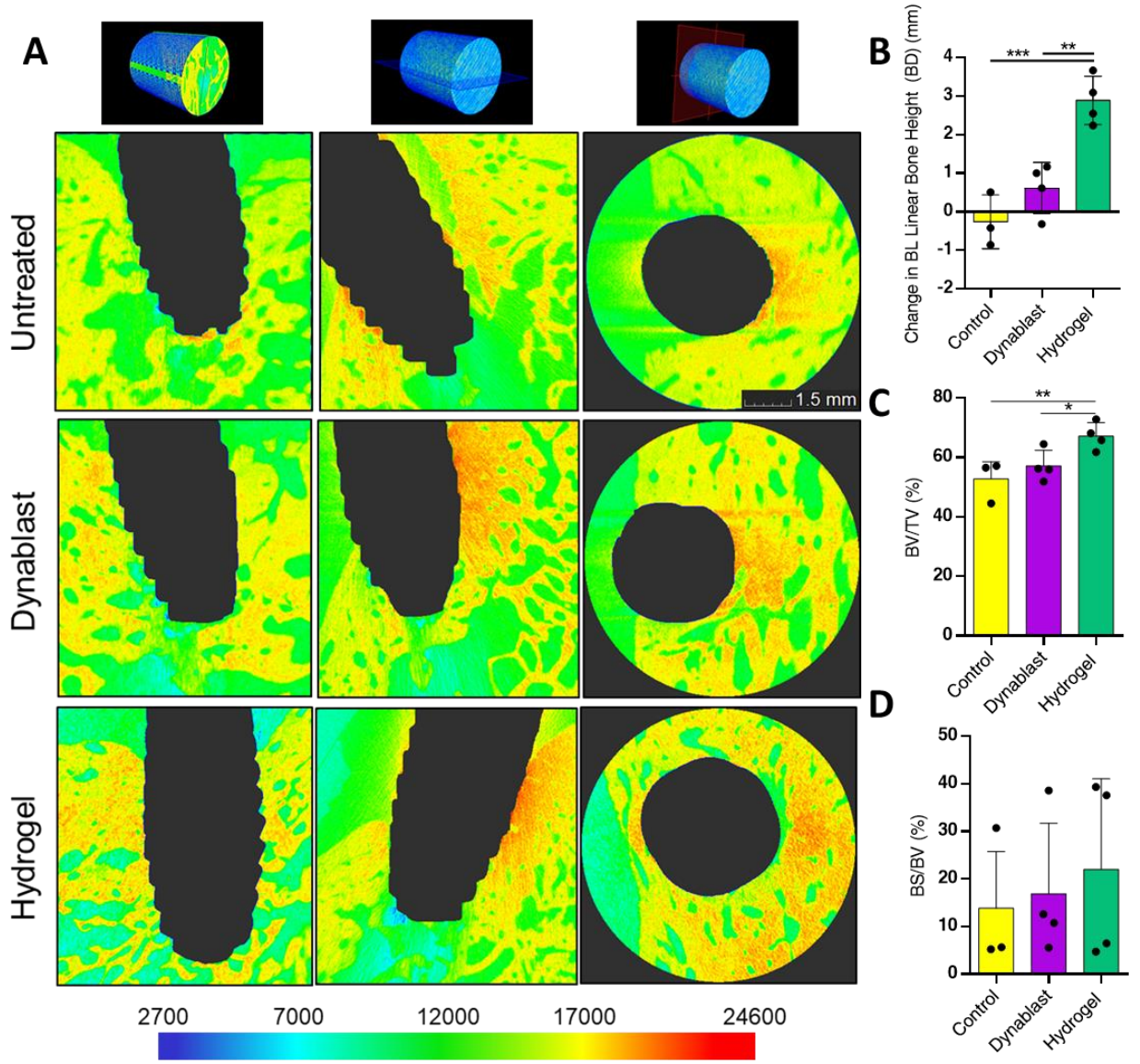

Figure 37. Analysis of bone regeneration and quality. **(A)** Micro computed tomography (µ-CT) images for the implants treated with bioadhesive hydrogels, and Dynablast and untreated controls at different angels. **(B)** changes in total linear bone height calculated from CT images. **(B)** bone volume fraction (BV/TV) and **(D)** Bone surface density (BS/BV) for all the samples, calculated from µ-CT images. Data are represented as mean ± SD (*$p < 0.05$, **$p < 0.01$, ***$p < 0.001$, $n \geq 3$).

4. Conclusion

While traditional surgical closure and treatment of tissue defects is achieved by sutures, staples, or wires, the application of adhesives for different types of lesions is essential. The repair of parenchymatous defects, such as in the lungs, liver, or kidney, as well as hard tissues such as cartilage, bone and tooth is particularly challenging since the consistency of these tissues does not facilitate strong fastening of sutures or staples or due to non-healing nature of the tissue. An ideal tissue adhesive for wound closure and treatment of soft and hard tissues should be (i) biocompatible and biodegradable, (ii) rapidly crosslinked and easily applicable, (ii) antimicrobial and impervious to antibiotic resistance and to prevent biofilm formation, (iii) strongly adhesive, (iv) tunable and long lasting, and (v) optimal mechanical properties and degradation rate to allow new tissue ingrowth. Therefore, new biomaterial-based approaches are needed to address the limitations of currently available alternatives. Here, we introduced a new class of photocrosslinkable biomaterials that can be easily applied to the defect sites and enhance the healing process. First, we demonstrated highly elastic and adhesive materials for soft and flexible tissues. As an example, for the application of these adhesive biomaterials, we examined the sealing ability and physical properties of the adhesive material for corneal stromal defect and corneal laceration. The regenerative type of our biomaterial fully biointegrates with the native cornea, and can thus be used to repair corneal stromal defects and lacerations regardless of size and shape, leading to regeneration of corneal tissue and circumventing the need for transplantation in many patients. Next, since the multifunctional biomaterials with optimal mechanical, adhesive, antimicrobial, and differentiation properties, would constitute a more effective therapeutic strategy over conventional single-strategy approaches for different tissue engineering applications, we developed another class of photocrosslinkable adhesive biomaterials that were antimicrobial (by incorporation of metal oxide NPs or AMPs) and can be used for both hard and soft tissue

regeneration. In addition, it was shown that SNs can be incorporated into the adhesive hydrogels to induce osteoinductive functionality of the engineered hydrogels for treatment of peri-implantitis or periodontal bone defects. The engineered hydrogel adhesives could be readily delivered to the affected area and be photocrosslinked *in situ* using commercially available dental curing light units. In addition, we have also demonstrated that the incorporation of AMPs to adhesive hydrogels could effectively prevent bacterial colonization using *Porphyromonas gingivalis*, which is the main etiologic agent associated with chronic periodontitis. Moreover, we have shown that the incorporation of SNs could promote the osteogenic differentiation of human mesenchymal stem cells (hMSCs) *in vitro.* Furthermore, our results showed extensive new bone formation and complete healing of critical sized mandibular bone defects in miniature pigs after 8 weeks. Furthermore, the engineered SN-loaded GelMA-AMP adhesives was used to successfully treat PI and promote re-osseointegration *in vivo*, using large animal (miniature pigs) model of ligature induced PI. This can yield to new and promising therapeutic approaches for treatment of PI. In summary, we demonstrated multifunctional adhesive hydrogels which can be used for different tissue engineering applications.

5. References

1. Grinstaff, M.W., Designing hydrogel adhesives for corneal wound repair. Biomaterials, 2007. **28**(35): p. 5205-14.
2. Miki, D., et al., A Photopolymerized Sealant for Corneal Lacerations. Cornea, 2002. **21**(4): p. 393-399.
3. Chae, J.J., et al., Application of a Collagen-Based Membrane and Chondroitin Sulfate-Based Hydrogel Adhesive for the Potential Repair of Severe Ocular Surface Injuries. Military Medicine, 2014. **179**(6): p. 686-694.
4. Ghobril, C. and M.W. Grinstaff, The chemistry and engineering of polymeric hydrogel adhesives for wound closure: a tutorial. Chemical Society Reviews, 2015. **44**(7): p. 1820-1835.
5. Mehdizadeh, M. and J. Yang, Design strategies and applications of tissue bioadhesives. Macromol Biosci, 2013. **13**(3): p. 271-88.
6. Bouten, P.J., et al., The chemistry of tissue adhesive materials. Progress in Polymer Science, 2014. **39**(7): p. 1375-1405.
7. Trott, A.T., Cyanoacrylate tissue adhesives. An advance in wound care. Journal of the American Medical Association, 1997. **277**(19): p. 1559-60.
8. Alio, J.L., et al., Efficacy of synthetic and biological bioadhesives in scleral tunnel phacoemulsification in eyes with high myopia. J Cataract Refract Surg, 1998. **24**(7): p. 983-8.
9. Price Jr, J.A. and J.A.C. Wadsworth, Evaluation of an adhesive in cataract wound closure. American Journal of Ophthalmology, 1969. **68**(4): p. 663-668.
10. Meskin, S.W., et al., Liquid bandage (2-octyl cyanoacrylate) as a temporary wound barrier in clear corneal cataract surgery. Ophthalmology, 2005. **112**(11): p. 2015-21.
11. Leung, G.Y.S., et al., Preliminary in vitro evaluation of 2-octyl cyanoacrylate (Dermabond®) to seal corneal incisions. Cornea, 2005. **24**(8): p. 998-999.
12. Kim, T. and B.V. Kharod, Tissue adhesives in corneal cataract incisions. Curr Opin Ophthalmol, 2007. **18**(1): p. 39-43.
13. Webster, R.G., The Use of Adhesive for the Closure of Corneal Perforations. Archives of Ophthalmology, 1968. **80**(6): p. 705.
14. Alió, J.L., M.E. Mulet, and J.C. Garcia, Use of cyanoacrylate tissue adhesive in small-incision cataract surgery. Ophthalmic Surgery and Lasers, 1996. **27**(4): p. 270-274.
15. Shigemitsu, T. and Y. Majima, The utilization of a biological adhesive for wound treatment: comparison of suture, self-sealing sutureless and cyanoacrylate closure in the tensile strength test. Int Ophthalmol, 1996. **20**(6): p. 323-8.
16. Awan, K.J. and P.G. Spaeth, Use of isobutyl 2 cyanoacrylate tissue adhesive in the repair of conjunctival fistula in filtering procedures for glaucoma. Annals of Ophthalmology, 1974. **6**(8): p. 851-853.
17. Grady, F.J. and M. Forbes, Tissue adhesive for repair of conjunctival buttonhole in glaucoma surgery. Am J Ophthalmol, 1969. **68**(4): p. 656-8.
18. Zalta, A.H. and R.H. Wieder, Closure of leaking filtering blebs with cyanoacrylate tissue adhesive. Br J Ophthalmol, 1991. **75**(3): p. 170-3.
19. Al-Shahwan, S., et al., Long-term follow up of surgical repair of late bleb leaks after glaucoma filtering surgery. J Glaucoma, 2006. **15**(5): p. 432-6.
20. Haslinda, A.R., et al., Cyanoacrylate tissue glue for wound repair in early posttrabeculectomy conjunctival bleb leak: a case series. Int Med Case Rep J, 2015. **8**: p. 145-50.
21. Loane, M.E. and A. Galanopoulos, The surgical management of leaking filtering blebs. Curr Opin Ophthalmol, 1999. **10**(2): p. 121-5.
22. Hartnett, M.E. and T. Hirose, Cyanoacrylate glue in the repair of retinal detachment associated with posterior retinal breaks in infants and children. Retina, 1998. **18**(2): p. 125-9.

23. Hotta, K., A. Hirakata, and T. Hida, The management of retinal detachments associated with choroidal colobomas by vitrectomy with cyanoacrylate retinopexy. Jpn J Ophthalmol, 1998. **42**(4): p. 323-6.
24. McCuen Ii, B.W., et al., Transvitreal cyanoacrylate retinopexy in the management of complicated retinal detachment. Transactions of the American Ophthalmological Society, 1987. **85**: p. 195-207.
25. Sheta, S.M., T. Hida, and B.W. McCuen, 2nd, Cyanoacrylate tissue adhesive in the management of recurrent retinal detachment caused by macular hole. Am J Ophthalmol, 1990. **109**(1): p. 28-32.
26. Leahey, A.B., J.D. Gottsch, and W.J. Stark, Clinical experience with N-butyl cyanoacrylate (Nexacryl) tissue adhesive. Ophthalmology, 1993. **100**(2): p. 173-80.
27. Arentsen, J.J., P.R. Laibson, and E.J. Cohen, Management of corneal descemetoceles and perforations. Ophthalmic Surg, 1985. **16**(1): p. 29-33.
28. Gasset, A.R. and H.E. Kaufman, Epikeratoprosthesis. Replacement of superficial cornea by methyl methacrylate. Am J Ophthalmol, 1968. **66**(4): p. 641-5.
29. Ohrstrom, A., et al., Scleral reinforcement by a teflon graft and a tissue adhesive. Acta Ophthalmol, 1988. **66**(6): p. 643-6.
30. Murube, J. and E. Murube, Treatment of dry eye by blocking the lacrimal canaliculi. Surv Ophthalmol, 1996. **40**(6): p. 463-80.
31. Patten, J.T., Punctal occlusion with n-butyl cyanoacrylate tissue adhesive. Ophthalmic Surg, 1976. **7**(2): p. 24-6.
32. Ellis, D.A. and A. Shaikh, The ideal tissue adhesive in facial plastic and reconstructive surgery. J Otolaryngol, 1990. **19**(1): p. 68-72.
33. Greene, D., R.J. Koch, and R.L. Goode, Efficacy of octyl-2-cyanoacrylate tissue glue in blepharoplasty. A prospective controlled study of wound-healing characteristics. Arch Facial Plast Surg, 1999. **1**(4): p. 292-6.
34. Perin, L.F., A. Helene, Jr., and M.F. Fraga, Sutureless closure of the upper eyelids in blepharoplasty: use of octyl-2-cyanoacrylate. Aesthet Surg J, 2009. **29**(2): p. 87-92.
35. Trivedi, D., et al., Use of cyanoacrylate glue for temporary tarsorrhaphy in children. Ophthal Plast Reconstr Surg, 2014. **30**(1): p. 60-3.
36. Donnenfeld, E.D., H.D. Perry, and D.B. Nelson, Cyanoacrylate temporary tarsorrhaphy in the management of corneal epithelial defects. Ophthalmic Surg, 1991. **22**(10): p. 591-3.
37. Ardis, A.E., Preparation of monomeric alkyl alpha-cyano-acrylates. 1949, Google Patents.
38. Vauthier, C., et al., Poly(alkylcyanoacrylates) as biodegradable materials for biomedical applications. Advanced Drug Delivery Reviews, 2003. **55**(4): p. 519-548.
39. Leonard, F., et al., Synthesis and degradation of poly(alkyl-α-cyanoacrylates). Journal of Applied Polymer Science, 1966. **10**(2): p. 259–272.
40. Ciapetti, G., et al., Cytotoxicity testing of cyanoacrylates using direct contact assay on cell cultures. Biomaterials, 1994. **15**(1): p. 5.
41. Tseng, Y.C., et al., In vitro toxicity test of 2-cyanoacrylate polymers by cell culture method. J Biomed Mater Res, 1990. **24**(10): p. 1355-67.
42. Chen, W.L., et al., Comparison of the bacteriostatic effects, corneal cytotoxicity, and the ability to seal corneal incisions among three different tissue adhesives. Cornea, 2007. **26**(10): p. 1228-34.
43. Refojo, M.F., et al., Evaluation of adhesives for corneal surgery. Arch Ophthalmol, 1968. **80**(5): p. 645-56.
44. Leggat, P.A., D.R. Smith, and U. Kedjarune, Surgical applications of cyanoacrylate adhesives: a review of toxicity. ANZ J Surg, 2007. **77**(4): p. 209-13.
45. Refojo, M.F. and C.H. Dohlman, The tensile strength of adhesive joints between eye tissues and alloplastic materials. Am J Ophthalmol, 1969. **68**(2): p. 248-255.
46. Bahney, C.S., et al., Visible light photoinitiation of mesenchymal stem cell-laden bioresponsive hydrogels. Eur Cell Mater, 2011. **22**: p. 43-55; discussion 55.
47. Kohane, D.S. and R. Langer, Polymeric biomaterials in tissue engineering. Pediatr Res, 2008. **63**(5): p. 487-91.

48. Yanez-Soto, B., et al., Biochemically and topographically engineered poly(ethylene glycol) diacrylate hydrogels with biomimetic characteristics as substrates for human corneal epithelial cells. J Biomed Mater Res A, 2013. **101**(4): p. 1184-94.
49. Masket, S., et al., Hydrogel sealant versus sutures to prevent fluid egress after cataract surgery. J Cataract Refract Surg, 2014. **40**(12): p. 2057-66.
50. Calladine, D., M. Ward, and R. Packard, Adherent ocular bandage for clear corneal incisions used in cataract surgery. J Cataract Refract Surg, 2010. **36**(11): p. 1839-48.
51. Ramsook, S.S. and P.S. Hersh, Use of a hydrogel sealant in epithelial ingrowth removal after laser in situ keratomileusis. J Cataract Refract Surg, 2015. **41**(12): p. 2768-71.
52. Tevlin, R., et al., Biomaterials for craniofacial bone engineering. J Dent Res, 2014. **93**(12): p. 1187-95.
53. Ranger, W.R., et al., Pneumostasis of experimental air leaks with a new photopolymerized synthetic tissue sealant. Am Surg, 1997. **63**(9): p. 788-95.
54. Bryant, S.J., C.R. Nuttelman, and K.S. Anseth, Cytocompatibility of UV and visible light photoinitiating systems on cultured NIH/3T3 fibroblasts in vitro. J Biomater Sci Polym Ed, 2000. **11**(5): p. 439-57.
55. Carnahan, M.A., et al., Hybrid dendritic-linear polyester-ethers for in situ photopolymerization. J Am Chem Soc, 2002. **124**(19): p. 5291-3.
56. Mazzoccoli, J.P., et al., Mechanical and cell viability properties of crosslinked low- and high-molecular weight poly(ethylene glycol) diacrylate blends. J Biomed Mater Res A, 2010. **93**(2): p. 558-66.
57. Voit, B.I. and A. Lederer, Hyperbranched and highly branched polymer architectures--synthetic strategies and major characterization aspects. Chem Rev, 2009. **109**(11): p. 5924-73.
58. Gao, C. and D. Yan, Hyperbranched polymers: from synthesis to applications. Progress in Polymer Science, 2004. **29**(3): p. 183-275.
59. Caminade, A.M., et al., The key role of the scaffold on the efficiency of dendrimer nanodrugs. Nat Commun, 2015. **6**: p. 7722.
60. Grayson, S.M. and J.M. Frechet, Convergent dendrons and dendrimers: from synthesis to applications. Chem Rev, 2001. **101**(12): p. 3819-68.
61. Valencia-Gallegos, J.A., M.M. Álvarez, and V.J. Martínez-Merino, High loaded dendrimers with free peripheral groups. . Tetrahedron Letters, 2015. **56**(48): p. 4.
62. Wathier, M., et al., Dendritic macromers as in situ polymerizing biomaterials for securing cataract incisions. Journal of the American Chemical Society, 2004. **126**(40): p. 12744-12745.
63. Fischer, M. and F. Vögtle, Dendrimers: From Design to Application—A Progress Report. Angewandte Chemie International Edition, 1999. **38**(7): p. 884-905.
64. Frechet, J.M., Dendrimers and supramolecular chemistry. Proc Natl Acad Sci USA, 2002. **99**(8): p. 4782-7.
65. Andre, S., et al., Lactose-containing starburst dendrimers: influence of dendrimer generation and binding-site orientation of receptors (plant/animal lectins and immunoglobulins) on binding properties. Glycobiology, 1999. **9**(11): p. 1253-61.
66. Carnahan, M.A. and M.W. Grinstaff, Synthesis and Characterization of Poly(glycerol−succinic acid) Dendrimers. Macromolecules, 2001. **34**(22): p. 7648-7655.
67. Namazi, H. and M. Adeli, Dendrimers of citric acid and poly (ethylene glycol) as the new drug-delivery agents. Biomaterials, 2005. **26**(10): p. 1175-83.
68. Applegate, M.B., et al., Photocrosslinking of Silk Fibroin Using Riboflavin for Ocular Prostheses. Adv Mater, 2016. **28**(12): p. 2417-20.
69. Park, H.C., et al., Tissue adhesives in ocular surgery. Expert review of ophthalmology, 2014.
70. Mosesson, M.W., Fibrinogen and fibrin structure and functions. J Thromb Haemost, 2005. **3**(8): p. 1894-904.
71. Ariëns, R., Novel mechanisms that regulate clot structure/function. Thrombosis research, 2016. **141**: p. S25-S27.

72. Doolittle, R., The Conversion of Fibrinogen to Fibrin: A Brief History of Some Key Events. Matrix Biology, 2016. **In Press**.
73. Domingues, M.M., et al., Thrombin and fibrinogen gamma' impact clot structure by marked effects on intrafibrillar structure and protofibril packing. Blood, 2016. **127**(4): p. 487-95.
74. Wolberg, A.S., Thrombin generation and fibrin clot structure. Blood Rev, 2007. **21**(3): p. 131-42.
75. Bochyńska, A., et al., Tissue adhesives for meniscus tear repair: an overview of current advances and prospects for future clinical solutions., 2016. **27**(5): p. 1-18.
76. Harris, D.M., et al., Autologous fibrin tissue adhesive biodegration and systemic effects. Laryngoscope, 1987. **97**(10): p. 1141-4.
77. Sierra, D.H., et al., A method to determine shear adhesive strength of fibrin sealants. J Appl Biomater, 1992. **3**(2): p. 147-51.
78. Rama, P., et al., Autologous fibrin-cultured limbal stem cells permanently restore the corneal surface of patients with total limbal stem cell deficiency1. Transplantation, 2001. **72**(9): p. 1478-1485.
79. Bungum, M., P. Humaidan, and L. Bungum, Recombinant human albumin as protein source in culture media used for IVF: a prospective randomized study. Reproductive biomedicine online, 2002. **4**(3): p. 233-236.
80. Sugio, S., et al., Crystal structure of human serum albumin at 2.5 Å resolution. Protein engineering, 1999. **12**(6): p. 439-446.
81. Chao, H.H. and D.F. Torchiana, BioGlue: albumin/glutaraldehyde sealant in cardiac surgery. J Card Surg, 2003. **18**(6): p. 500-3.
82. Fürst, W. and A. Banerjee, Release of glutaraldehyde from an albumin-glutaraldehyde tissue adhesive causes significant in vitro and in vivo toxicity. The Annals of thoracic surgery, 2005. **79**(5): p. 1522-1528.
83. Kobayashi, K., Summary of recombinant human serum albumin development. Biologicals, 2006. **34**(1): p. 55-9.
84. Cao, H., et al., Structural consistency analysis of recombinant and wild-type human serum albumin Journal of Molecular Structure, 2017. **1127**: p. 1-5.
85. Meek, K.M. and C. Boote, The organization of collagen in the corneal stroma. Exp Eye Res, 2004. **78**(3): p. 503-12.
86. Maurice, D.M., The structure and transparency of the cornea. J Physiol, 1957. **136**(2): p. 263-86.
87. Baldock, C., et al., Three-dimensional reconstructions of extracellular matrix polymers using automated electron tomography. Journal of structural biology, 2002. **138**(1): p. 130-136.
88. Kim, E.Y., et al., Collagen type I-PLGA film as an efficient substratum for corneal endothelial cells regeneration. Journal of Tissue Engineering and Regenerative Medicine, 2016: p. n/a-n/a.
89. Miki, D., et al., A photopolymerized sealant for corneal lacerations. Cornea, 2002. **21**(4): p. 393-9.
90. Chae, J.J., et al., Application of a collagen-based membrane and chondroitin sulfate-based hydrogel adhesive for the potential repair of severe ocular surface injuries. Mil Med, 2014. **179**(6): p. 686-94.
91. Noguera, G., et al., Novel laser-activated solder for sealing corneal wounds. Invest Ophthalmol Vis Sci, 2007. **48**(3): p. 1038-42.
92. Xiao, X., et al., In vivo study of the biocompatibility of a novel compressed collagen hydrogel scaffold for artificial corneas. J Biomed Mater Res A, 2014. **102**(6): p. 1782-7.
93. Calderon-Colon, X., et al., Structure and properties of collagen vitrigel membranes for ocular repair and regeneration applications. Biomaterials, 2012. **33**(33): p. 8286-95.
94. Matteini, P., et al., Microscopic characterization of collagen modifications induced by low-temperature diode-laser welding of corneal tissue. Lasers Surg Med, 2007. **39**(7): p. 597-604.
95. Zhao, L., et al., A novel smart injectable hydrogel prepared by microbial transglutaminase and human-like collagen: Its characterization and biocompatibility. Mater Sci Eng C Mater Biol Appl, 2016. **68**: p. 317-26.

96. Miyashita, H., et al., Collagen-immobilized poly (vinyl alcohol) as an artificial cornea scaffold that supports a stratified corneal epithelium. Journal of Biomedical Materials Research Part B: Applied Biomaterials, 2006. **76**(1): p. 56-63.
97. Zhang, J., et al., Characterization of a Novel Collagen Scaffold for Corneal Tissue Engineering. Tissue Eng Part C Methods, 2015. **22**(2): p. 165-172.
98. Rafat, M., et al., PEG-stabilized carbodiimide crosslinked collagen-chitosan hydrogels for corneal tissue engineering. Biomaterials, 2008. **29**(29): p. 3960-72.
99. Liu, W., M. Griffith, and F. Li, Alginate microsphere-collagen composite hydrogel for ocular drug delivery and implantation. J Mater Sci Mater Med, 2008. **19**(11): p. 3365-71.
100. Liu, W., et al., Recombinant human collagen for tissue engineered corneal substitutes. Biomaterials, 2008. **29**(9): p. 1147-58.
101. Liu, W., et al., Collagen–phosphorylcholine interpenetrating network hydrogels as corneal substitutes. Biomaterials, 2009. **30**(8): p. 1551-1559.
102. Deng, C., et al., Collagen and glycopolymer based hydrogel for potential corneal application. Acta Biomater, 2010. **6**(1): p. 187-94.
103. Ahn, J.-I., et al., Crosslinked collagen hydrogels as corneal implants: effects of sterically bulky vs. non-bulky carbodiimides as crosslinkers. Acta biomaterialia, 2013. **9**(8): p. 7796-7805.
104. Annabi, N., et al., Engineering a sprayable and elastic hydrogel adhesive with antimicrobial properties for wound healing. Biomaterials, 2017. **139**: p. 229-243.
105. Yamamoto, S., et al., Feasibility of using gelatin-microbial transglutaminase complex to repair experimental retinal detachment in rabbit eyes. Graefe's Archive for Clinical and Experimental Ophthalmology, 2013. **251**(4): p. 1109-1114.
106. McDermott, M.K., et al., Mechanical properties of biomimetic tissue adhesive based on the microbial transglutaminase-catalyzed crosslinking of gelatin. Biomacromolecules, 2004. **5**(4): p. 1270-9.
107. Chen, T., et al., Gelatin-based biomimetic tissue adhesive. Potential for retinal reattachment. J Biomed Mater Res B Appl Biomater, 2006. **77**(2): p. 416-22.
108. Nagai, N., et al., Decrease in corneal Damage due to Benzalkonium Chloride by the Addition of Sericin into Timolol Maleate Eye Drops. Journal of Oleo Science, 2013. **62**(3): p. 159-166.
109. Reyes, J.M., et al., A modified chondroitin sulfate aldehyde adhesive for sealing corneal incisions. Invest Ophthalmol Vis Sci, 2005. **46**(4): p. 1247-50.
110. Li, Q., et al., Photocrosslinkable polysaccharides based on chondroitin sulfate. J Biomed Mater Res A, 2004. **68**(1): p. 28-33.
111. Wang, D.A., et al., Multifunctional chondroitin sulphate for cartilage tissue-biomaterial integration. Nat Mater, 2007. **6**(5): p. 385-92.
112. Strehin, I., et al., Synthesis and characterization of a chondroitin sulfate-polyethylene glycol corneal adhesive. J Cataract Refract Surg, 2009. **35**(3): p. 567-76.
113. Strehin, I., et al., A versatile pH sensitive chondroitin sulfate-PEG tissue adhesive and hydrogel. Biomaterials, 2010. **31**(10): p. 2788-97.
114. Hiemstra, C., et al., Novel in Situ Forming, Degradable Dextran Hydrogels by Michael Addition Chemistry: Synthesis, Rheology, and Degradation. Macromolecules, 2007. **40**(4): p. 1165-1173.
115. Jin, R., et al., Enzyme-mediated fast in situ formation of hydrogels from dextran-tyramine conjugates. Biomaterials, 2007. **28**(18): p. 2791-800.
116. Takaoka, M., et al., Novel sutureless keratoplasty with a chemically defined bioadhesive. Invest Ophthalmol Vis Sci, 2009. **50**(6): p. 2679-85.
117. Noshadi, I., et al., In vitro and in vivo analysis of visible light crosslinkable gelatin methacryloyl (GelMA) hydrogels. Biomater Sci, 2017.
118. Assmann, A., et al., A highly adhesive and naturally derived sealant. Biomaterials, 2017. **140**: p. 115-127.

119. Smeds, K.A. and M.W. Grinstaff, Photocrosslinkable polysaccharides for in situ hydrogel formation (vol 54, pg 115, 2000). Journal of Biomedical Materials Research, 2001. **55**(2): p. 254-255.
120. Bian, L.M., et al., Enhanced MSC chondrogenesis following delivery of TGF-beta 3 from alginate microspheres within hyaluronic acid hydrogels in vitro and in vivo. Biomaterials, 2011. **32**(27): p. 6425-6434.
121. Zhang, Y.N., et al., A Highly Elastic and Rapidly Crosslinkable Elastin-Like Polypeptide-Based Hydrogel for Biomedical Applications. Adv Funct Mater, 2015. **25**(30): p. 4814-4826.
122. Guillemette, M.D., et al., Combined technologies for microfabricating elastomeric cardiac tissue engineering scaffolds. Macromol Biosci, 2010. **10**(11): p. 1330-7.
123. Chen, C.Y., G.W. Nace, and P.L. Irwin, A 6 x 6 drop plate method for simultaneous colony counting and MPN enumeration of Campylobacter jejuni, Listeria monocytogenes, and Escherichia coli. J Microbiol Methods, 2003. **55**(2): p. 475-9.
124. Fantes, F.E., et al., Wound healing after excimer laser keratomileusis (photorefractive keratectomy) in monkeys. Archives of ophthalmology, 1990. **108**(5): p. 665-75.
125. National Institutes of Health, ImageJ, .
126. Assmann, A., et al., Acceleration of autologous in vivo recellularization of decellularized aortic conduits by fibronectin surface coating. Biomaterials, 2013. **34**(25): p. 6015-26.
127. Sani, E.S., et al., Sutureless repair of corneal injuries using naturally derived bioadhesive hydrogels. Science Advances, 2019. **5**: p. eaav1281.
128. Islam, M.M., et al., Biomaterials-enabled cornea regeneration in patients at high risk for rejection of donor tissue transplantation. NPJ Regenerative medicine, 2018. **3**(1): p. 2.
129. Gain, P., et al., Global survey of corneal transplantation and eye banking. JAMA Ophthalmology, 2016. **134**(2): p. 167-173.
130. Ljubimov, A.V. and M. Saghizadeh, Progress in corneal wound healing. Progress in Retinal and Eye Research, 2015. **49**: p. 17-45.
131. Ciapetti, G., et al., Cytotoxicity testing of cyanoacrylates using direct contact assay on cell cultures. Biomaterials, 1994. **15**(1): p. 63-67.
132. Matossian, C., S. Makari, and R. Potvin, Cataract surgery and methods of wound closure: a review. Clinical Ophthalmology, 2015. **9**: p. 921.
133. Nishida, K., et al., Corneal reconstruction with tissue-engineered cell sheets composed of autologous oral mucosal epithelium. New England Journal of Medicine, 2004. **351**(12): p. 1187-96.
134. Kharod-Dholakia, B., et al., Prevention and treatment of corneal graft rejection: current practice patterns of the Cornea Society (2011). Cornea, 2015. **34**(6): p. 609-614.
135. Chen, Z., et al., Biomaterials for corneal bioengineering. Biomed Mater, 2018. **13**(3): p. 032002.
136. Park, H.C., et al., Tissue adhesives in ocular surgery. Expert review of ophthalmology, 2011.
137. Uy, H.S. and K.R. Kenyon, Surgical outcomes after application of a liquid adhesive ocular bandage to clear corneal incisions during cataract surgery. Journal of Cataract & Refractive Surgery, 2013. **39**(11): p. 1668-1674.
138. Li, L., et al., Gelatin-Based Photocurable Hydrogels for Corneal Wound Repair. ACS Applied Materials & Interfaces, 2018. **10**(16): p. 13283-13292.
139. Maurice, D.M., The structure and transparency of the cornea. The Journal of Physiology, 1957. **136**(2): p. 263-286.
140. Chae, J.J., et al., Regeneration of corneal epithelium utilizing a collagen vitrigel membrane in rabbit models for corneal stromal wound and limbal stem cell deficiency. Acta ophthalmologica, 2015. **93**(1).
141. Calderón-Colón, X., et al., Structure and properties of collagen vitrigel membranes for ocular repair and regeneration applications. Biomaterials, 2012. **33**(33): p. 8286-8295.
142. Banitt, M., et al., Wound integrity of clear corneal incisions closed with fibrin and N-butyl-2-cyanoacrylate adhesives. Current eye research, 2009. **34**(8): p. 706-710.

143. Rose, J., et al., Gelatin-Based Materials in Ocular Tissue Engineering. Materials, 2014. **7**(4): p. 3106.
144. Mishra, D. and R. Gilhotra, Design and characterization of bioadhesive in-situ gelling ocular inserts of gatifloxacin sesquihydrate. Daru, 2008. **16**(1).
145. Gratieri, T., et al., A poloxamer/chitosan in situ forming gel with prolonged retention time for ocular delivery. European Journal of Pharmaceutics and Biopharmaceutics, 2010. **75**(2): p. 186-193.
146. Assmann, A., et al., A highly adhesive and naturally derived sealant. Biomaterials, 2017. **140**: p. 115-127.
147. Kielbassa, C., L. Roza, and B. Epe, Wavelength dependence of oxidative DNA damage induced by UV and visible light. Carcinogenesis, 1997. **18**(4): p. 811-6.
148. Behar-Cohen, F., et al., Ultraviolet damage to the eye revisited: eye-sun protection factor (E-SPF®), a new ultraviolet protection label for eyewear. Clinical Ophthalmology, 2014. **8**: p. 87-104.
149. Youn, H.-Y., et al., In vitro ultraviolet–induced damage in human corneal, lens, and retinal pigment epithelial cells. Molecular Vision, 2011. **17**: p. 237-246.
150. Ramasamy, K., et al., Ultraviolet radiation-induced carcinogenesis: Mechanisms and experimental models. Journal of Radiation and Cancer Research, 2017. **8**(1): p. 4-19.
151. Bergmanson, J.P.G. and P.G. Söderberg, The significance of ultraviolet radiation for eye diseases. A review with comments on the efficacy of UV-blocking contact lenses. Ophthalmic and Physiological Optics, 1995. **15**(2): p. 83-91.
152. Delori, F.C., R.H. Webb, and D.H. Sliney, Maximum permissible exposures for ocular safety (ANSI 2000), with emphasis on ophthalmic devices. Journal of the Optical Society of America A, 2007. **24**(5): p. 1250-1265.
153. Bryant, S.J., C.R. Nuttelman, and K.S. Anseth, Cytocompatibility of UV and visible light photoinitiating systems on cultured NIH/3T3 fibroblasts in vitro. Journal of Biomaterials Science, Polymer Edition, 2000. **11**(5): p. 439-457.
154. Hang, L., et al., Cartilage Tissue Engineering Application of Injectable Gelatin Hydrogel with In Situ Visible-Light-Activated Gelation Capability in Both Air and Aqueous Solution. Tissue Engineering Part A, 2014. **20**(17-18): p. 2402-2411.
155. Soucy, M.J.R., et al., Photocrosslinkable Gelatin/Tropoelastin Hydrogel Adhesives for Peripheral Nerve Repair. Tissue Engineering Part A, 2018. **0**(0).
156. Noshadi, I., et al., In vitro and in vivo analysis of visible light crosslinkable gelatin methacryloyl (GelMA) hydrogels. Biomaterials science, 2017. **5**(10): p. 2093-2105.
157. Annabi, N., et al., Elastic sealants for surgical applications. European journal of pharmaceutics and biopharmaceutics : official journal of Arbeitsgemeinschaft fur Pharmazeutische Verfahrenstechnik e.V, 2015. **95**(0 0): p. 27-39.
158. Bahney, C., et al., Visible light photoinitiation of mesenchymal stem cell-laden bioresponsive hydrogels. European cells & materials, 2011. **22**: p. 43.
159. Rizwan, M., et al., Sequentially-crosslinked bioactive hydrogels as nano-patterned substrates with customizable stiffness and degradation for corneal tissue engineering applications. Biomaterials, 2017. **120**: p. 139-154.
160. Pircher, M., et al., Measurement and imaging of water concentration in human cornea with differential absorption optical coherence tomography. Optics Express, 2003. **11**(18): p. 2190-2197.
161. Lauto, A., D. Mawad, and L.J.R. Foster, Adhesive biomaterials for tissue reconstruction. Journal of Chemical Technology & Biotechnology, 2008. **83**(4): p. 464-472.
162. Pawar, R.P., Jadhav, A. E., Tathe, S. B., Khade, B. C. and Domb, A. J., Medicinal Applications of Cyanoacrylate, in Biodegradable Polymers in Clinical Use and Clinical Development, N.K.a.A.E. A. J. Domb, Editor. 2011.
163. Sawhney, P.K.C.S.L.B.A.D.A.S., Evaluation of Absorbable Surgical Sealants: In vitro Testing. Covidien, 2005.

164. Spotnitz, W.D., Fibrin Sealant: The Only Approved Hemostat, Sealant, and Adhesive;a Laboratory and Clinical Perspective. ISRN Surgery, 2014. **2014**: p. 28.
165. Chen, W.-L., et al., Comparison of the bacteriostatic effects, corneal cytotoxicity, and the ability to seal corneal incisions among three different tissue adhesives. Cornea, 2007. **26**(10): p. 1228-1234.
166. Hee Park, D., et al., In vitro degradation and cytotoxicity of alkyl 2-cyanoacrylate polymers for application to tissue adhesives. Journal of applied polymer science, 2003. **89**(12): p. 3272-3278.
167. Ma, Y., et al., Reconstruction of chemically burned rat corneal surface by bone marrow–derived human mesenchymal stem cells. Stem cells, 2006. **24**(2): p. 315-321.
168. Kelaini, S., A. Cochrane, and A. Margariti, Direct reprogramming of adult cells: avoiding the pluripotent state. Stem cells and cloning: advances and applications, 2014. **7**: p. 19.
169. Linhardt, R.J., S. Murugesan, and J. Xie, Immobilization of heparin: approaches and applications. Current topics in medicinal chemistry, 2008. **8**(2): p. 80-100.
170. Panda, A., et al., Fibrin glue in ophthalmology. Indian Journal of Ophthalmology, 2009. **57**(5): p. 371-379.
171. Jia, X. and K.L. Kiick, Hybrid multicomponent hydrogels for tissue engineering. Macromol Biosci, 2009. **9**(2): p. 140-56.
172. Annabi, N., et al., 25th anniversary article: Rational design and applications of hydrogels in regenerative medicine. Adv Mater, 2014. **26**(1): p. 85-123.
173. Drago, L., et al., Does Implant Coating With Antibacterial-Loaded Hydrogel Reduce Bacterial Colonization and Biofilm Formation in Vitro? Clinical Orthopaedics and Related Research, 2014. **472**(11): p. 3311-3323.
174. Sharma, B., et al., Human cartilage repair with a photoreactive adhesive-hydrogel composite. Science translational medicine, 2013. **5**(167): p. 167ra6-167ra6.
175. Shirzaei Sani, E., et al., Engineering Adhesive and Antimicrobial Hyaluronic Acid/Elastin-like Polypeptide Hybrid Hydrogels for Tissue Engineering Applications. ACS Biomaterials Science & Engineering, 2018.
176. Chuah, Y.J., et al., Hydrogel based cartilaginous tissue regeneration: recent insights and technologies. Biomater Sci, 2017.
177. Tan, H., et al., Injectable in situ forming biodegradable chitosan-hyaluronic acid based hydrogels for cartilage tissue engineering. Biomaterials, 2009. **30**(13): p. 2499-506.
178. Hoemann, C.D., et al., Tissue engineering of cartilage using an injectable and adhesive chitosan-based cell-delivery vehicle. Osteoarthritis and Cartilage, 2005. **13**(4): p. 318-329.
179. Kim, I.L., R.L. Mauck, and J.A. Burdick, Hydrogel design for cartilage tissue engineering: a case study with hyaluronic acid. Biomaterials, 2011. **32**(34): p. 8771-82.
180. Levett, P.A., et al., A biomimetic extracellular matrix for cartilage tissue engineering centered on photocurable gelatin, hyaluronic acid and chondroitin sulfate. Acta Biomater, 2014. **10**(1): p. 214-23.
181. Chen, W.H., et al., Synergistic anabolic actions of hyaluronic acid and platelet-rich plasma on cartilage regeneration in osteoarthritis therapy. Biomaterials, 2014. **35**(36): p. 9599-607.
182. Lee, P., et al., Influence of chondroitin sulfate and hyaluronic acid presence in nanofibers and its alignment on the bone marrow stromal cells: cartilage regeneration. J Biomed Nanotechnol, 2014. **10**(8): p. 1469-79.
183. Skaalure, S.C., et al., Semi-interpenetrating networks of hyaluronic acid in degradable PEG hydrogels for cartilage tissue engineering. Acta Biomater, 2014. **10**(8): p. 3409-20.
184. Yodmuang, S., et al., Silk microfiber-reinforced silk hydrogel composites for functional cartilage tissue repair. Acta Biomater, 2015. **11**: p. 27-36.
185. Singh, Y.P., N. Bhardwaj, and B.B. Mandal, Potential of Agarose/Silk Fibroin Blended Hydrogel for in Vitro Cartilage Tissue Engineering. ACS Appl Mater Interfaces, 2016. **8**(33): p. 21236-49.
186. Chao, P.H., et al., Silk hydrogel for cartilage tissue engineering. J Biomed Mater Res B Appl Biomater, 2010. **95**(1): p. 84-90.

187. Kontturi, L.S., et al., An injectable, in situ forming type II collagen/hyaluronic acid hydrogel vehicle for chondrocyte delivery in cartilage tissue engineering. Drug Deliv Transl Res, 2014. **4**(2): p. 149-58.
188. Parmar, P.A., et al., Collagen-mimetic peptide-modifiable hydrogels for articular cartilage regeneration. Biomaterials, 2015. **54**: p. 213-25.
189. Balakrishnan, B., et al., Self-crosslinked oxidized alginate/gelatin hydrogel as injectable, adhesive biomimetic scaffolds for cartilage regeneration. Acta Biomaterialia, 2014. **10**(8): p. 3650-3663.
190. Park, H. and K.Y. Lee, Facile control of RGD-alginate/hyaluronate hydrogel formation for cartilage regeneration. Carbohydrate Polymers, 2011. **86**(3): p. 1107-1112.
191. Moss, I.L., et al., A Novel Thiol-Modified Hyaluronan and Elastin-Like Polypetide Composite Material for Tissue Engineering of the Nucleus Pulposus of the Intervertebral Disc. Spine, 2011. **36**(13): p. 1022-1029.
192. Yang, J., et al., Cell-Laden Hydrogels for Osteochondral and Cartilage Tissue Engineering. Acta Biomater, 2017.
193. Liao, J., et al., Recent developments in scaffold-guided cartilage tissue regeneration. J Biomed Nanotechnol, 2014. **10**(10): p. 3085-104.
194. McHale, M.K., L.A. Setton, and A. Chilkoti, Synthesis and in Vitro Evaluation of Enzymatically Cross-Linked Elastin-Like Polypeptide Gels for Cartilaginous Tissue Repair. Tissue Engineering, 2006. **11**(11-12): p. 1768-1779.
195. Betre, H., et al., Characterization of a genetically engineered elastin-like polypeptide for cartilaginous tissue repair. Biomacromolecules, 2002. **3**(5): p. 910-6.
196. McHale, M.K., L.A. Setton, and A. Chilkoti, Synthesis and in vitro evaluation of enzymatically cross-linked elastin-like polypeptide gels for cartilaginous tissue repair. Tissue Eng, 2005. **11**(11-12): p. 1768-79.
197. MacEwan, S.R. and A. Chilkoti, Elastin-like polypeptides: biomedical applications of tunable biopolymers. Biopolymers, 2010. **94**(1): p. 60-77.
198. Moss, I.L., et al., A novel thiol-modified hyaluronan and elastin-like polypetide composite material for tissue engineering of the nucleus pulposus of the intervertebral disc. Spine (Phila Pa 1976), 2011. **36**(13): p. 1022-9.
199. Collins, M.N. and C. Birkinshaw, Hyaluronic acid based scaffolds for tissue engineering--a review. Carbohydr Polym, 2013. **92**(2): p. 1262-79.
200. Yoon, I.S., et al., Proliferation and chondrogenic differentiation of human adipose-derived mesenchymal stem cells in porous hyaluronic acid scaffold. J Biosci Bioeng, 2011. **112**(4): p. 402-8.
201. Kim, I.L., et al., Fibrous hyaluronic acid hydrogels that direct MSC chondrogenesis through mechanical and adhesive cues. Biomaterials, 2013. **34**(22): p. 5571-5580.
202. Sato, E., et al., High molecular weight hyaluronic acid increases the differentiation potential of the murine chondrocytic ATDC5 cell line. J Orthop Res, 2014. **32**(12): p. 1619-27.
203. Matsiko, A., et al., Addition of hyaluronic acid improves cellular infiltration and promotes early-stage chondrogenesis in a collagen-based scaffold for cartilage tissue engineering. J Mech Behav Biomed Mater, 2012. **11**: p. 41-52.
204. Hillel, A.T., et al., Photoactivated composite biomaterial for soft tissue restoration in rodents and in humans. Science translational medicine, 2011. **3**(93): p. 93ra67-93ra67.
205. Pitarresi, G., et al., Medicated hydrogels of hyaluronic acid derivatives for use in orthopedic field. International Journal of Pharmaceutics, 2013. **449**(1-2): p. 84-94.
206. Chung, C., et al., Influence of gel properties on neocartilage formation by auricular chondrocytes photoencapsulated in hyaluronic acid networks. J Biomed Mater Res A, 2006. **77**(3): p. 518-25.
207. Bian, L., et al., The influence of hyaluronic acid hydrogel crosslinking density and macromolecular diffusivity on human MSC chondrogenesis and hypertrophy. Biomaterials, 2013. **34**(2): p. 413-21.
208. Zhu, D., et al., Elastin-like protein-hyaluronic acid (ELP-HA) hydrogels with decoupled mechanical and biochemical cues for cartilage regeneration. Biomaterials, 2017. **127**: p. 132-140.

209. Bernhard, J.C. and G. Vunjak-Novakovic, Should we use cells, biomaterials, or tissue engineering for cartilage regeneration? Stem Cell Research & Therapy, 2016. **7**.
210. Pelgrift, R.Y. and A.J. Friedman, Nanotechnology as a therapeutic tool to combat microbial resistance. Advanced Drug Delivery Reviews, 2013. **65**(13–14): p. 1803-1815.
211. Sharma, R.K. and K. Balani, Mechanics of ZnO micro-rod and ZnO nanoparticle reinforcement in ultra-high molecular weight polyethylene biocomposite. Journal of Physics D: Applied Physics, 2014. **47**(34): p. 345301.
212. Mohandas, A., et al., Exploration of alginate hydrogel/nano zinc oxide composite bandages for infected wounds. Int J Nanomedicine, 2015. **10 Suppl 1**: p. 53-66.
213. Lau, H.K. and K.L. Kiick, Opportunities for multicomponent hybrid hydrogels in biomedical applications. Biomacromolecules, 2015. **16**(1): p. 28-42.
214. Zhu, Q., et al., Structural identification of (1-->6)-alpha-d-glucan, a key responsible for the health benefits of longan, and evaluation of anticancer activity. Biomacromolecules, 2013. **14**(6): p. 1999-2003.
215. Astachov, L., et al., Hyaluronan and mesenchymal stem cells: from germ layer to cartilage and bone. Front Biosci (Landmark Ed), 2011. **16**: p. 261-76.
216. Smeds, K.A., et al., Photocrosslinkable polysaccharides for in situ hydrogel formation. J Biomed Mater Res, 2001. **54**(1): p. 115-21.
217. Chen, M., M. Zhong, and J.A. Johnson, Light-Controlled Radical Polymerization: Mechanisms, Methods, and Applications. Chem Rev, 2016. **116**(17): p. 10167-211.
218. Chatani, S., C.J. Kloxin, and C.N. Bowman, The power of light in polymer science: photochemical processes to manipulate polymer formation, structure, and properties. Polymer Chemistry, 2014. **5**(7): p. 2187-2201.
219. Burdick, J.A. and G.D. Prestwich, Hyaluronic acid hydrogels for biomedical applications. Advanced materials, 2011. **23**(12).
220. Burdick, J.A. and G.D. Prestwich, Hyaluronic acid hydrogels for biomedical applications. Adv Mater, 2011. **23**(12): p. H41-56.
221. Tan, H., et al., Injectable in situ forming biodegradable chitosan–hyaluronic acid based hydrogels for cartilage tissue engineering. Biomaterials, 2009. **30**(13): p. 2499-2506.
222. Snyder, T.N., et al., A fibrin/hyaluronic acid hydrogel for the delivery of mesenchymal stem cells and potential for articular cartilage repair. J Biol Eng, 2014. **8**: p. 10.
223. Lim, D.W., et al., In situ cross-linking of elastin-like polypeptide block copolymers for tissue repair. Biomacromolecules, 2008. **9**(1): p. 222-30.
224. Nguyen, Q.T., et al., Cartilage-like mechanical properties of poly (ethylene glycol)-diacrylate hydrogels. Biomaterials, 2012. **33**(28): p. 6682-90.
225. Wang, L., et al., Hydrogel-based methods for engineering cellular microenvironment with spatiotemporal gradients. Crit Rev Biotechnol, 2016. **36**(3): p. 553-65.
226. Annabi, N., et al., The fabrication of elastin-based hydrogels using high pressure CO 2. Biomaterials, 2009. **30**(1): p. 1-7.
227. Trabbic-Carlson, K., L.A. Setton, and A. Chilkoti, Swelling and mechanical behaviors of chemically cross-linked hydrogels of elastin-like polypeptides. Biomacromolecules, 2003. **4**(3): p. 572-580.
228. Martin, L., et al., Synthesis and characterization of macroporous thermosensitive hydrogels from recombinant elastin-like polymers. Biomacromolecules, 2009. **10**(11): p. 3015-22.
229. Liu, H., Nanocomposites for Musculoskeletal Tissue Regeneration. 2016: Elsevier Science.
230. Park, H., et al., Effect of swelling ratio of injectable hydrogel composites on chondrogenic differentiation of encapsulated rabbit marrow mesenchymal stem cells in vitro. Biomacromolecules, 2009. **10**(3): p. 541-6.
231. Resende, R.R., et al., Scale/topography of substrates surface resembling extracellular matrix for tissue engineering. J Biomed Nanotechnol, 2014. **10**(7): p. 1157-93.

232. Costantini, M., et al., 3D bioprinting of BM-MSCs-loaded ECM biomimetic hydrogels for in vitro neocartilage formation. Biofabrication, 2016. **8**(3): p. 035002.
233. Liu, S.Q., et al., Biomimetic hydrogels for chondrogenic differentiation of human mesenchymal stem cells to neocartilage. Biomaterials, 2010. **31**(28): p. 7298-307.
234. Noth, U., et al., Chondrogenic differentiation of human mesenchymal stem cells in collagen type I hydrogels. J Biomed Mater Res A, 2007. **83**(3): p. 626-35.
235. Vazquez-Portalati, N.N., et al., Characterization of Collagen Type I and II Blended Hydrogels for Articular Cartilage Tissue Engineering. Biomacromolecules, 2016. **17**(10): p. 3145-3152.
236. Parmar, P.A., et al., Temporally degradable collagen-mimetic hydrogels tuned to chondrogenesis of human mesenchymal stem cells. Biomaterials, 2016. **99**: p. 56-71.
237. Chung, C. and J.A. Burdick, Influence of three-dimensional hyaluronic acid microenvironments on mesenchymal stem cell chondrogenesis. Tissue Eng Part A, 2009. **15**(2): p. 243-54.
238. Toh, W.S., et al., Modulation of mesenchymal stem cell chondrogenesis in a tunable hyaluronic acid hydrogel microenvironment. Biomaterials, 2012. **33**(15): p. 3835-45.
239. Finnegan, S. and S.L. Percival, Clinical and Antibiofilm Efficacy of Antimicrobial Hydrogels. Adv Wound Care (New Rochelle), 2015. **4**(7): p. 398-406.
240. Ng, V.W., et al., Antimicrobial hydrogels: a new weapon in the arsenal against multidrug-resistant infections. Adv Drug Deliv Rev, 2014. **78**: p. 46-62.
241. Kumar, P.T., et al., Flexible and microporous chitosan hydrogel/nano ZnO composite bandages for wound dressing: in vitro and in vivo evaluation. ACS Appl Mater Interfaces, 2012. **4**(5): p. 2618-29.
242. Chung, C., et al., The influence of degradation characteristics of hyaluronic acid hydrogels on in vitro neocartilage formation by mesenchymal stem cells. Biomaterials, 2009. **30**(26): p. 4287-96.
243. Sahoo, S., et al., Hydrolytically degradable hyaluronic acid hydrogels with controlled temporal structures. Biomacromolecules, 2008. **9**(4): p. 1088-92.
244. Liu, W., et al., Tumor accumulation, degradation and pharmacokinetics of elastin-like polypeptides in nude mice. J Control Release, 2006. **116**(2): p. 170-8.
245. Shamji, M.F., et al., An injectable and in situ-gelling biopolymer for sustained drug release following perineural administration. Spine (Phila Pa 1976), 2008. **33**(7): p. 748-54.
246. Jepsen, S., et al., Primary prevention of peri-implantitis: managing peri-implant mucositis. J Clin Periodontol, 2015. **42 Suppl 16**: p. S152-7.
247. Peri-implant mucositis and peri-implantitis: a current understanding of their diagnoses and clinical implications. J Periodontol, 2013. **84**(4): p. 436-43.
248. Levin, L., Editorial: peri-implantitis: the disease of the future. Quintessence Int, 2013. **44**(9): p. 643.
249. Renvert, S., A.M. Roos-Jansaker, and N. Claffey, Non-surgical treatment of peri-implant mucositis and peri-implantitis: a literature review. J Clin Periodontol, 2008. **35**(8 Suppl): p. 305-15.
250. Grusovin, M.G., et al., Interventions for replacing missing teeth: maintaining and recovering soft tissue health around dental implants. Cochrane Database Syst Rev, 2010(8): p. CD003069.
251. Suarez-Lopez Del Amo, F., S.H. Yu, and H.L. Wang, Non-Surgical Therapy for Peri-Implant Diseases: a Systematic Review. J Oral Maxillofac Res, 2016. **7**(3): p. e13.
252. Shanbhag, S., et al., Bone tissue engineering in oral peri-implant defects in preclinical in vivo research: a systematic review and meta-analysis. J Tissue Eng Regen Med, 2017.
253. Froum, S.J., et al., Successful Surgical Protocols in the Treatment of Peri-Implantitis: A Narrative Review of the Literature. Implant Dent, 2016. **25**(3): p. 416-26.
254. Hanisch, O., et al., Bone formation and reosseointegration in peri-implantitis defects following surgical implantation of rhBMP-2. Int J Oral Maxillofac Implants, 1997. **12**(5): p. 604-10.
255. Woo, E.J., Adverse events reported after the use of recombinant human bone morphogenetic protein 2. J Oral Maxillofac Surg, 2012. **70**(4): p. 765-7.
256. Mesfin, A., et al., High-dose rhBMP-2 for adults: major and minor complications: a study of 502 spine cases. J Bone Joint Surg Am, 2013. **95**(17): p. 1546-53.

257. Gottlow, J., et al., New attachment formation as the result of controlled tissue regeneration. J Clin Periodontol, 1984. **11**(8): p. 494-503.
258. Nyman, S., Bone regeneration using the principle of guided tissue regeneration. J Clin Periodontol, 1991. **18**(6): p. 494-8.
259. Gaharwar, A.K., et al., Bioactive silicate nanoplatelets for osteogenic differentiation of human mesenchymal stem cells. Adv Mater, 2013. **25**(24): p. 3329-36.
260. Mihaila, S.M., et al., The osteogenic differentiation of SSEA-4 sub-population of human adipose derived stem cells using silicate nanoplatelets. Biomaterials, 2014. **35**(33): p. 9087-99.
261. Xavier, J.R., et al., Bioactive nanoengineered hydrogels for bone tissue engineering: a growth-factor-free approach. ACS Nano, 2015. **9**(3): p. 3109-18.
262. Gaharwar, A.K., et al., Bioactive silicate nanoplatelets for osteogenic differentiation of human mesenchymal stem cells. Advanced materials, 2013. **25**(24): p. 3329-3336.
263. Mihaila, S.M., et al., The osteogenic differentiation of SSEA-4 sub-population of human adipose derived stem cells using silicate nanoplatelets. Biomaterials, 2014. **35**(33): p. 9087-9099.
264. Cheng, H., et al., Mussel-Inspired Multifunctional Hydrogel Coating for Prevention of Infections and Enhanced Osteogenesis. ACS Applied Materials & Interfaces, 2017.
265. Monteiro, N., et al., Photopolymerization of cell-laden gelatin methacryloyl hydrogels using a dental curing light for regenerative dentistry. Dental Materials, 2018. **34**(3): p. 389-399.
266. Huebsch, N., et al., Matrix elasticity of void-forming hydrogels controls transplanted-stem-cell-mediated bone formation. Nature materials, 2015. **14**(12): p. 1269.
267. Peh, K.K. and C.F. Wong, Polymeric films as vehicle for buccal delivery: swelling, mechanical, and bioadhesive properties. J Pharm Pharm Sci, 1999. **2**(2): p. 53-61.
268. Nasajpour, A., et al., A multifunctional polymeric periodontal membrane with osteogenic and antibacterial characteristics. Advanced Functional Materials, 2018. **28**(3): p. 1703437.
269. Purk, J.H., et al., In vitro microtensile bond strength of four adhesives tested at the gingival and pulpal walls of Class II restorations. 2006. **137**(10): p. 1414-1418.
270. Sofan, E., et al., Classification review of dental adhesive systems: from the IV generation to the universal type. 2017. **8**(1): p. 1.
271. Kazemzadeh-Narbat, M., et al., Antimicrobial peptides on calcium phosphate-coated titanium for the prevention of implant-associated infections. Biomaterials, 2010. **31**(36): p. 9519-26.
272. Khurshid, Z., et al., Human Oral Defensins Antimicrobial Peptides: A Future Promising Antimicrobial Drug. Curr Pharm Des, 2018. **24**(10): p. 1130-1137.
273. Mallapragada, S., A. Wadhwa, and P. Agrawal, Antimicrobial peptides: The miraculous biological molecules. J Indian Soc Periodontol, 2017. **21**(6): p. 434-438.
274. Shi, J., et al., Biological and immunotoxicity evaluation of antimicrobial peptide-loaded coatings using a layer-by-layer process on titanium. Scientific reports, 2015. **5**: p. 16336.
275. Holmberg, K.V., et al., Bio-inspired stable antimicrobial peptide coatings for dental applications. Acta biomaterialia, 2013. **9**(9): p. 8224-8231.
276. Yoshinari, M., et al., Prevention of biofilm formation on titanium surfaces modified with conjugated molecules comprised of antimicrobial and titanium-binding peptides. Biofouling, 2010. **26**(1): p. 103-110.
277. Thies, R.S., et al., Recombinant human bone morphogenetic protein-2 induces osteoblastic differentiation in W-20-17 stromal cells. Endocrinology, 1992. **130**(3): p. 1318-1324.
278. Maruyama, T., et al., Stem cells of the suture mesenchyme in craniofacial bone development, repair and regeneration. Nature communications, 2016. **7**: p. ncomms10526.
279. Wilk, K., et al., Postnatal calvarial skeletal stem cells expressing PRX1 reside exclusively in the calvarial sutures and are required for bone regeneration. Stem cell reports, 2017. **8**(4): p. 933-946.
280. Mohandas, A., et al., Exploration of alginate hydrogel/nano zinc oxide composite bandages for infected wounds. 2015. **10**(Suppl 1): p. 53.
281. Wahid, F., et al., Recent advances in antimicrobial hydrogels containing metal ions and metals/metal oxide nanoparticles. 2017. **9**(12): p. 636.

282. Patterson, J., et al., Hyaluronic acid hydrogels with controlled degradation properties for oriented bone regeneration. Biomaterials, 2010. **31**(26): p. 6772-6781.
283. Gibbs, D.M., et al., A review of hydrogel use in fracture healing and bone regeneration. Journal of tissue engineering and regenerative medicine, 2016. **10**(3): p. 187-198.
284. Chamieh, F., et al., Accelerated craniofacial bone regeneration through dense collagen gel scaffolds seeded with dental pulp stem cells. Scientific reports, 2016. **6**: p. 38814.
285. Nguyen, M.K., et al., RNA interfering molecule delivery from in situ forming biodegradable hydrogels for enhancement of bone formation in rat calvarial bone defects. Acta biomaterialia, 2018.
286. Kyllönen, L., et al., Local drug delivery for enhancing fracture healing in osteoporotic bone. Acta biomaterialia, 2015. **11**: p. 412-434.
287. Wang, Y., et al., Electrospun nanosilicates-based organic/inorganic nanofibers for potential bone tissue engineering. Colloids Surf B Biointerfaces, 2018. **172**: p. 90-97.
288. Jensen, S.S. and H. Terheyden, Bone augmentation procedures in localized defects in the alveolar ridge: clinical results with different bone grafts and bone-substitute materials. Int J Oral Maxillofac Implants, 2009. **24 Suppl**: p. 218-36.
289. Mellonig, J.T. and M. Nevins, Guided bone regeneration of bone defects associated with implants: an evidence-based outcome assessment. Int J Periodontics Restorative Dent, 1995. **15**(2): p. 168-85.
290. Simion, M., et al., Guided bone regeneration using resorbable and nonresorbable membranes: a comparative histologic study in humans. Int J Oral Maxillofac Implants, 1996. **11**(6): p. 735-42.
291. Fonseca, R.J., et al., Revascularization and healing of onlay particulate autologous bone grafts in primates. J Oral Surg, 1980. **38**(8): p. 572-7.
292. Phillips, J.H. and B.A. Rahn, Fixation effects on membranous and endochondral onlay bone graft revascularization and bone deposition. Plast Reconstr Surg, 1990. **85**(6): p. 891-7.
293. Jensen, O.T., et al., Vertical guided bone-graft augmentation in a new canine mandibular model. Int J Oral Maxillofac Implants, 1995. **10**(3): p. 335-44.
294. Tinti, C. and S. Parma-Benfenati, Vertical ridge augmentation: surgical protocol and retrospective evaluation of 48 consecutively inserted implants. Int J Periodontics Restorative Dent, 1998. **18**(5): p. 434-43.
295. Herford, A.S. and J.S. Dean, Complications in bone grafting. Oral Maxillofac Surg Clin North Am, 2011. **23**(3): p. 433-42.
296. Inc., i.R., US Dental Bone Graft Substitutes and other Biomaterials Market. 2015: iData Research Inc.
297. Pietruska, M.D.J.E.j.o.o.s., A comparative study on the use of Bio-Oss® and enamel matrix derivative (Emdogain®) in the treatment of periodontal bone defects. 2001. **109**(3): p. 178-181.
298. Wong, R. and A.J.T.o.b.e.j. Rabie, Effect of Bio-Oss® Collagen and Collagen matrix on bone formation. 2010. **4**: p. 71.
299. Duda, M. and J. Pajak. The issue of bioresorption of the Bio-Oss xenogeneic bone substitute in bone defects. in Annales Universitatis Mariae Curie-Sklodowska. Sectio D: Medicina. 2004.